Marta Serra Giza
B. of Sc. in Biochemistry

A mixed computational modelling and experimental approach to the interaction between gold nanoparticles and blood proteins

Dissertation for Master's degree in Biochemistry

Supervisor: Prof. Doutor José Ricardo Franco Tavares; UCIBIO, REQUIMTE, Departamento de Química, Faculdade de Ciências e Tecnologia, Universidade Nova de Lisboa

Auxilliary supervisor: Prof. Doutor Ludwig Krippahl; CENTRIA, Departamento de Informática, Faculdade de Ciências e Tecnologia, Universidade Nova de Lisboa

24th October 2016

FACULDADE DE CIÊNCIAS E TECNOLOGIA
UNIVERSIDADE NOVA DE LISBOA

Marta Serra Giza
B. of Sc. in Biochemistry

A mixed computational modelling and experimental approach to the interaction between gold nanoparticles and blood proteins

Dissertation for Master's degree in Biochemistry

Supervisor: Prof. Doutor José Ricardo Ramos Franco Tavares; UCIBIO, REQUIMTE, Departamento de Química, Faculdade de Ciências e Tecnologia, Universidade Nova de Lisboa

Auxilliary supervisor: Prof. Doutor Ludwig Krippahl; CENTRIA, Departamento de Informática, Faculdade de Ciências e Tecnologia, Universidade Nova de Lisboa

24th October 2016

Blank page

Copyrights

Blank page

Acknowledgments

I would like to thank the Bionanolab crew, as well as both supervisors for the support and incentive. It has been a very gratifying experience to develop work alongside with you.

I would also like to kindly thank everyone else involved for all the complicity and time spent with me throughout this year.

"Do not fear to think even the most not-probable."

- Bram Stoker, *Dracula*

Blank page

Contents

List of Figures

List of Tables

Blank page

Abstract

Upon arrival at the bloodstream, injected gold nanoparticles are covered with circulating plasma proteins, creating what is called a plasma corona. Its protein content is determined by the proteins' affinity constants to the exposed surface of the nanoparticle. This work aims to propose an interaction mechanism between three plasma proteins and CALNN-functionalized nanoparticles via computational simulation and complementary experimental approach. Denaturing polyacrylamide gel electrophoresis determined the protein content of two human plasma samples, and helped in the characterization of the three most abundant blood proteins used in this study. Estimation of their electrostatic potential surfaces, silhouette areas, and diameters allowed the evaluation of the theoretical number of proteins forming a fully-covered nanoparticle. Seventeen transferrin molecules and eighteen albumin molecules with a side-on adsorption orientation were predicted to represent a monolayer adsorbome in a 20 nm gold nanoparticle. The dynamics of albumin adsorption to nanoparticles was studied through incubation-time assays on agarose gel electrophoresis, resulting in a stable protein corona starting from 7 h incubation time. The concentration ratio forming protein corona at the surface of nanoparticles was analysed through agarose gels electrophoretic mobility assays, revealing the formation of a full protein corona when a plateau in bionanoconjugates migration is achieved, resulting in protein coronas of [HSA]:[AuNP-CALNN] of 200:1 and 600:1 for [BPF]:[AuNP-CALNN] concentration ratios. Zeta-potential values were derived by relating agarose percentage with electrophoretic mobility of albumin bionanoconjugates, resulting in lower potential values for bionanoconjugates due to surface charge shielding of nanoparticles. Obtained ζ-potential values ranged from -26.05 up to -20.36 mV, forming colloid stable bionanoconjugates. Hydrodynamic radii of bionanoconjugates of albumin supported the formation of a monolayered and two-layered protein corona with increasing albumin:nanoparticle concentration ratios. Transferrin and fibrinogen showed increasing hydrodynamic radii with increasing protein:nanoparticle concentration ratios; in which fibrinogen bionanoconjugates showed fibrinogen wrapping around the nanoparticle. Electrostatic potential surfaces and protein-ligand docking using nanoparticle's capping agent CALNN was performed in order to predict possible adsorption sites of human albumin and transferrin.

Keywords: Gold nanoparticles, protein corona, plasma proteins, electrophoresis, dynamic light scattering, bioinformatics.

Blank page

Resumo

Após entrada na corrente sanguínea, as nanopartículas de ouro são cobertas com proteínas plasmáticas formando uma coroa proteica. O conteúdo em proteínas depende das constantes de afinidade das proteínas para a superfície das nanopartículas. Esta dissertação tem como objectivo propôr um mecanismo de interacção entre três proteínas do plasma e nanopartículas de ouro funcionalizadas com o péptido CALNN, através de uma abordagem mista de trabalho computacional complementado com ensaios laboratoriais. Géis de poliacrilamida em condições desnaturantes permitiram determinar o conteúdo proteico de duas amostras de plasma humano e a caracterização das três proteínas mais abundantes do plasma. A previsão das superfícies de potencial electrostático, das áreas da silhueta das proteínas e do seu diâmetro permitiu determinar o número de proteínas que formam uma monocamada proteíca em torno de uma nanopartícula de ouro. Dezassete moléculas de albumina e dezoito moléculas de transferrina com uma adsorção de orientação '*side-on*' formam uma monocamada proteína à volta de uma nanopartícula de ouro com 20 nm de diâmetro. A dinâmica de adsorção da albumina humana a nanopartículas de ouro foi estudada através de ensaios com variação de tempos de incubação. Os resultados mostram a formação de uma coroa proteica estável a partir das 7 h de incubação. A razão de concentrações proteína:nanopartícula que forma uma coroa de proteínas foi estudada através de ensaios de mobilidade electroforética, e admitiu-se a formação da mesma quando se observa um patamar na migração dos bionanoconjugados, que resultaram na razão 200:1 para [HSA]:[AuNP-CALNN], e 600:1 para razões de concentração de fibrinogénio. O potencial zeta de bionanoconjugados de albumina foram determinados através de ensaios de mobilidade electroforética com variação da concentração de agarose; nos quais os potenciais para bionanoconjugados foram menores que para as nanopartículas livres, sendo que a adsorção de albumina a nanopartículas de ouro promove a diminuição da carga superficial das nanopartículas (de -26.16 mV até -20.36 mV). A determinação dos raios hidrodinâmicos dos bionanoconjugados, nanopartículas e proteínas permitiu caracterizar a corona proteíca de albumina como uma mono e dupla camada em torno da nanopartícula; para a transferrina e fibrinogénio, os raios hidrodinâmicos aumentam com o aumento das razões de concentração de proteína. Os bionanoconjugados de fibrinogénio apresentam adsorpção 'wrapping' em torno das AuNPs. O cálculo das superfícies de potencial electrostático e a realização de ensaios de docking com as proteínas do plasma permitiu a determinação dos locais preferenciais de ligação do péptido CALNN durante a adsorção a nanopartículas de ouro.

Palavras-chave: Nanopartículas de ouro, corona proteíca, proteínas plasmáticas, dispersão de luz dinâmica, electroforese, bionformática.

1. Introduction

1.1. Gold nanoparticles

Gold nanoparticles (AuNPs) can be defined as entities of metallic gold (Au) atoms ranging from 1 to 100 nanometers in diameter [1–5] (**Figure 1.1**) that can exhibit various shapes; the most common being the quasi-spherical shape [2]. These particles are synthetized in aqueous solution and thus are also known as colloidal gold.

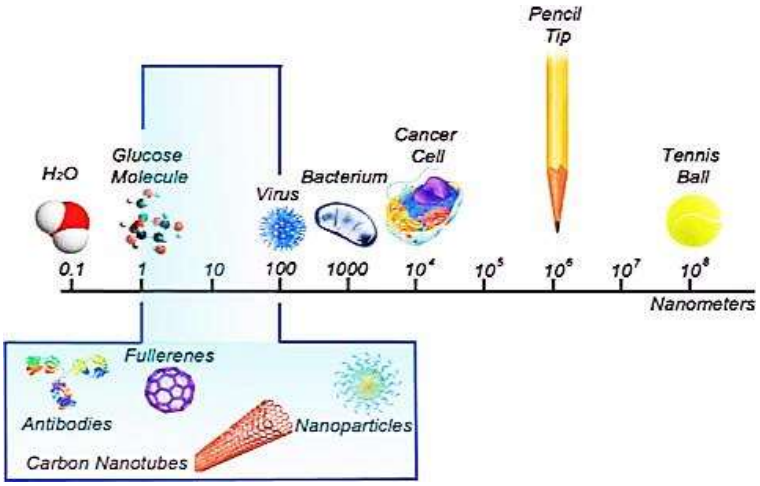

Figure 1.1. The size range of nanoparticles (blue outline) [6].

1.1.1. Surface plasmon resonance

One of the most explored features of gold nanoparticles is the phenomenon known by surface plasmon resonance (SPR), which explains the difference between the optical behaviour of gold nanoparticles and the one of macromolecular gold structures. Bulk gold atoms and solutions display a yellow color to the naked eye, as opposing to the red-wine color of gold nanoparticles in suspension [5,7]. SPR is the optical phenomenon occurring when incident light resonates with the intrinsic oscillation of gold valence electrons of nanoparticles, resulting in a strong absorbance band in the visible light spectrum [5] (**Figure 1.2**).

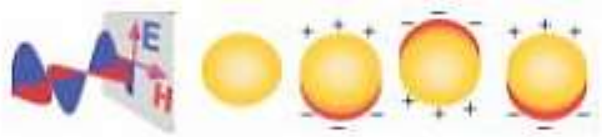

Figure 1.2. Electromagnetic radiation interacting with a nanosphere. *Adapted from* [5].

Incident electromagnetic (EM) radiation induces the formation of a dipole in a nanoparticle, causing its free conduction electrons to continuously oscillate against the proton restoring force. The frequency of this oscillation resonates with the frequency of visible light, and its maximum amplitude is called surface plasmon resonance. The SPR band of gold spherical nanoparticles can therefore be detected by spectroscopy in the visible region of the light spectrum [1,5,7].

Dispersed spherical gold nanoparticles from 10-100 nm in diameter show a strong SPR absorbance peak in the green EM spectrum region at around 520 nm [1,7,8]. Their optical properties can change, for example, by increasing ionic strenght in the solution or by varying the pH; producing delocalization of the conducting electrons from the nanoparticle surface which lowers the frequency of resonance to the red spectrum region (**Figure 1.3**), proof of nanoparticle aggregation.

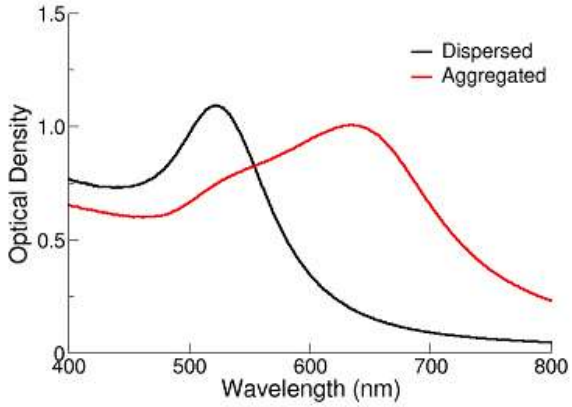

Figure 1.3. UV-Vis spectra of aggregated and dispersed gold nanoparticles [9].

1.1.1. Nanoparticle functionalization

The core of the nanoparticle (NP) is highly stable due to the tight packing between neighbour atoms. As the surface atoms have less surrounding atoms and therefore are less stable, they tend to interact with other species from the surrounding media in order to minimize their high surface energy [1,3].

Functionalization of nanoparticle surfaces is usually performed to stabilize them and prevent spontaneous aggregation, that can result in particles of macroscopic scale [1–5]. Capping of AuNPs is the defining step on their intrinsic properties and future applications. It takes advantage of the high reactivity of the surface Au atoms of the nanoparticle by promoting interaction with the reacting species, who also act as stabilizing agents during synthesis. The adsorption of these capping agents to AuNP is a dynamic process, occurring at a rate that is determined by the affinity of the reactant to the nanoparticle surface. These agents are also in equilibrium with the solvent molecules, enhancing homogeneous dispersion of the AuNPs in solution [1–5].

Nanoparticle surface functionalization is also performed in order to promote biomolecular interaction with AuNP, leading to a wide array of applications in scientific research, and health diagnosis and therapeutics [2,10]. The capping agents on the nanoparticle surface alter its intrinsic properties, serving as an adsorption vehicle for biomolecules. The introduction to nanoparticles in living systems results in formation of bionanoconjugates whose biological functions can be characterized by taking advantage of nanoparticles' physicochemical properties [10].

1.1.1.1. Capping agents

The most common capping agents used for biosensing applications of gold nanoparticles are citrate and 11-mercaptoundecanoic acid (MUA) (**Figure 1.4**). The first is a weak organic acid that interacts quickly with the Au valence electronic cloud by electrostatic repulsion of its negatively-charged carboxylic group, and therefore is defined as a labile capping agent.

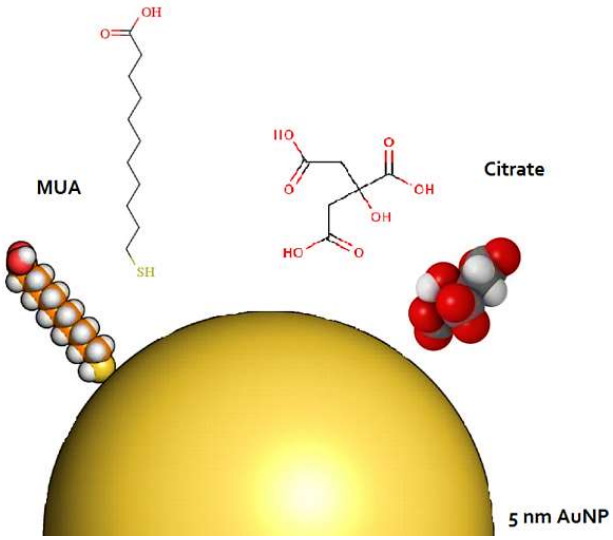

Figure 1.4. A 5 nanometer gold nanoparticle sphere capped with one MUA (left) and one citrate (right) molecule (not drawn to scale). *Adapted from* [3].

MUA is an eleven carbon hydrocarbon containing a terminal thiol group which covalently binds to the Au surface, and thus its equilibrium rate with the solvent molecules is much slower [1,3]. The terminal carboxylic group of both capping agents conveys a global negative charge to the functionalized AuNP, which consequently promotes the formation of a hydration layer around the nanoparticle, increasing colloidal stability [1,3].

The synthetic peptide CALNN (**Figure 1.5**) is also a thiol-binding capping agent, interacting covalently with the external gold atoms of AuNP [11]. The sulphur atom of cysteine enables covalent binding to the gold nanoparticle and arginine's carboxylic group provides negative terminal charge to the bionanoconjugate. In addition, alanine and leucine's hydrophobic side chains promote self-assembly of the molecule. This pentapeptide was rationally designed to create a well-packed layer at the AuNP surface, resulting in highly soluble, non-aggregating and non-flocculating, capped nanoparticles with chemical properties comparable to those of proteins [11].

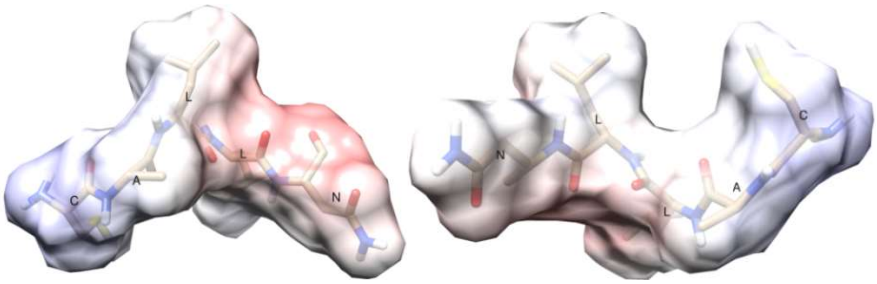

Figure 1.5. Front and back-views (left and right, respectively) of CALNN electrostatic potential surface at pH 7.4.

1.2. Protein corona

Conjugation between biomolecules and AuNPs can be used to study the interactions happening at a cellular level, aiming to a deeper understanding of biological systems [2,10,12]. More specifically, protein-AuNP conjugates have been developed to investigate their functions in multiple living systems (**Figure 1.6**), which can act as labelling, delivery, heating or sensing agents [2,10,12].

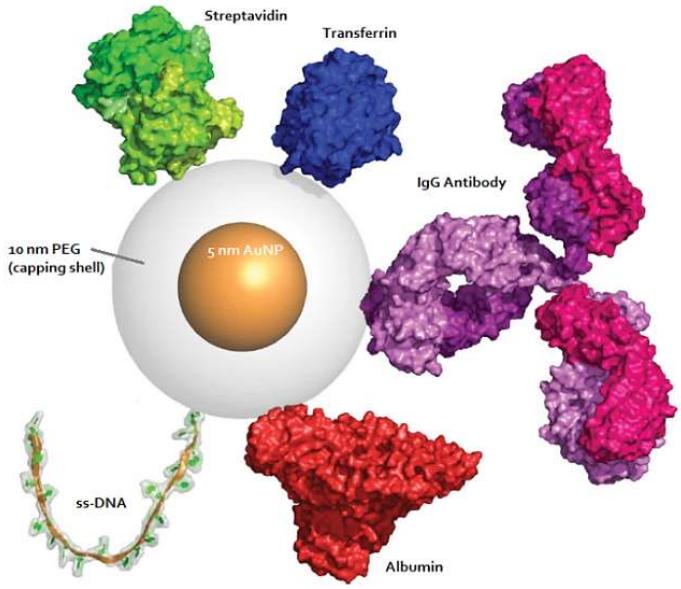

Figure 1.6. Representation of protein and DNA conjugates with a functionalized 15 nm AuNP (draw to scale). *Adapted from* [10].

The adsorption of proteins to functionalized gold nanoparticles is a two-step process, initiated by a fast electrostatic interaction between the surface of the AuNP and the exposed opposite-charged residues of the protein. Then a slower conformational rearrangement can occur by replacement of the capping agent, hydrophobic interactions with core aminoacid residues or cysteine's thiol-gold bonding [1,3]. These interactions can lead to an irreversible protein conformational change, resulting in change of biological function [1,3].

1.2.1. The Vroman effect

The set of proteins adsorbed to the nanoparticle surface is defined as the NP's protein corona (**Figure 1.7**). The Vroman effect, applied in the bionanotechnology field, determines the composition of the protein corona stating that the concentration of adsorbed proteins to the NP remains relatively constant over time, but the protein identity of the corona varies over time due to the different affinity constants presented by different proteins, generating competitive adsorption at the binding sites of the nanoparticle [3,4].

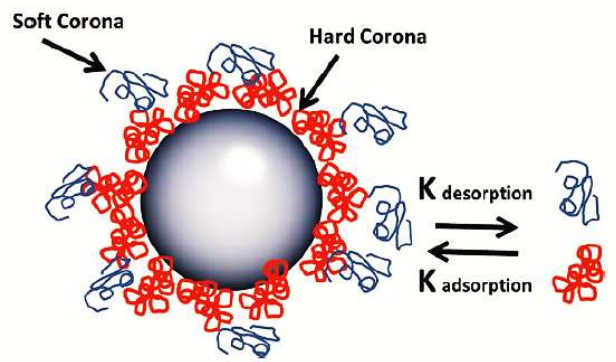

Figure 1.7. Formation of soft and hard corona in a nanoparticle. *Adapted from [4].*

This protein corona is governed by protein-nanoparticle affinity, as well as multiple protein-protein interactions. Both processes are dependent of the kinetics and thermodynamics of each interaction [3,4]. Proteins existing in (1) higher concentration; (2) those that diffuse quickly in the media and/or (3) those that have high affinity to the NP's surface can adsorb to it through stronger bonds and interactions [3,4], forming a robust hard corona layer. In a second stage, lower-affinity or scarce proteins interact loosely with the proteins of the hard corona, creating a much more transient soft protein corona [3,4]. The hard corona proteins show bigger exchange times with free proteins in solution than the soft corona proteins.

1.2.1.1. Time evolution of protein adsorption to nanoparticles

In the case of gold nanoparticles, it has already been shown that a full protein corona is formed within fourty-eight hours (48 h) of time incubation [13]. This time interval assures the formation of a permanent and stable hard corona of slowly exchanging proteins and an outer, labile and soft protein corona layer [13,14]. **Figure 1.8** shows an electrophoretic agarose gel of AuNP-MUA particles conjugated with human serum albumin for different incubation times, and representations of bionanoconjugates and unbound nanoparticles.

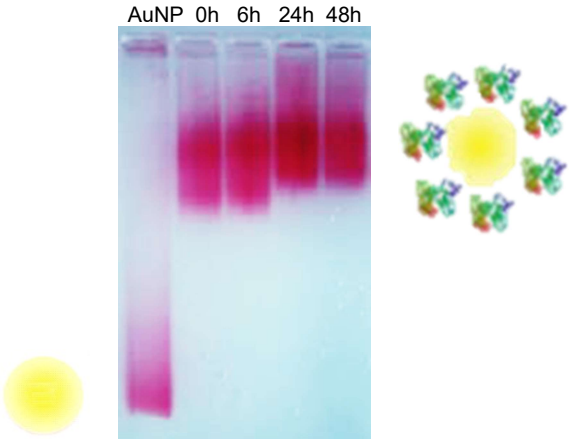

Figure 1.8. Agarose gel digital image of AuNP-MUA bionanoconjugates of human serum albumin after different incubation times at room temperature [13].

During electrophoresis, bionanoconjugates show less migration than gold nanoparticles alone. This can be explained by their increased molecular weight and lower electric surface charge potential. On the other hand, unbound nanoparticles migrate in the gel at a greater speed owing to higher surface potential and smaller size [13,14].

Figure 1.8 also shows that shorter incubation times produce a higher amount of loosely bound proteins, mostly because short incubation times are not enough to allow stronger protein adsorption to nanoparticles. Giving this, bionanoconjugates incubated up to 6 h reveal loss of protein content during electrophoresis producing increase of surface charge [14]. This protein disassociation generates nanoparticles coated with different amounts of protein, producing the smear visible on the bands in the gel. Bionanoconjugates incubated for longer times generate a tighter protein corona which, due to higher molecular weight, migrates less in the agarose gel [14].

Electrophoresis can be a powerful technique to qualitatively access nanoparticle coverage, because protein adsorption influences surface charge and molecular weight of free nanoparticles; the main properties analysed by this technique [14]; and additional explanations on this technique are given further ahead.

1.2.2. Nanoparticle size and curvature

Nanoparticle size strongly affects the formation and nature of the protein corona [1,14]. As the nanoparticle diameter increases surface curvature becomes lower, influencing the available contact area for protein adsorption [1,14]. Proteins can have two orientation preferences when adsorbing to nanoparticles: (1) side-on, with higher contact area promoting stronger interactions and even irreversible adsorption; or (2) end-on, with weaker interactions due to lower contact area (**Figure 1.9**). This adsorption orientation gives rise to less conformational changes in the protein structure than in side-on adsorption [1].

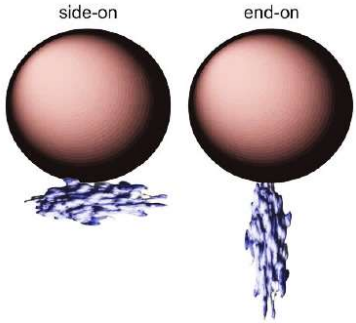

Figure 1.9. Possible orientations of a protein upon conjugation with a gold nanoparticle [1].

When nanoparticle size becomes close to protein size, this scale effect becomes essential on the formation of the protein corona. For globular proteins, a high surface curvature decreases protein-protein interactions, avoiding lateral interactions and crowding effect (**Figure 1.10**).

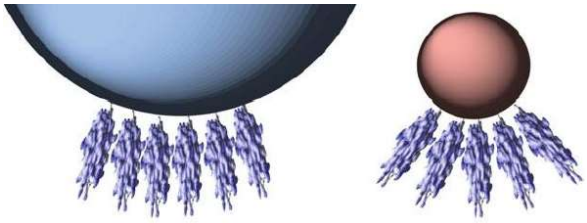

Figure 1.10. Crowding effect on low (left) and high curvature (right) nanoparticles [1].

For fibrillar proteins, like fibrinogen, profound conformational changes are observed upon adsorption, promoted by side-on adsorption and protein wrapping around the nanoparticle [1]. This kind of effects are extremely important when proteins adsorb to nanoparticles in a biological system.

1.1. Blood proteins

Human blood is a complex and heterogeneous mixture harbouring as much as 10,500 different proteins [15], whose composition varies constantly in response to development, age and gender, metabolic activity, genetic background and epigenetics, post-translational modifications, state of disease and lifestyle [16]. Fractionation by centrifugation of a blood sample, generates two high-density phases rich in leucocytes and platelets (1.0 %), and erythrocytes (45 %) [17]. The remaining low-density phase (54 %) bears the total protein content of the blood and is designated as plasma [17]. **Table 1.1** lists the most common proteins, its molecular weight and concentration in human plasma; **Figure 1.11** shows a denaturing polyacrylamide gel electrophoresis (SDS-PAGE) of human plasma sample.

Table 1.1. Major protein components of human plasma.

Adapted from [17].

Protein	Molecular weight (kDa)	Concentration (g/L)
Albumin	66.0	38.0-48.0
Fibrinogen	341	2.0-4.5
Transferrin	77.0	1.8-2.7
α2 macroglobulin	800	1.5-3.5
α1 antitrypsin	54.0	1.4-4.0
Haptoglobulin	100	1.2-2.6
α1 acid glycoprotein	44.0	0.6-1.4
Caeruloplasmin	132	0.2-0.6
Retinol-binding protein	21.0	0.03-0.1
C-reactive protein	105	<0.003
β2 microglobulin	11.8	<0.002
Immunoglobulins	160-900	---

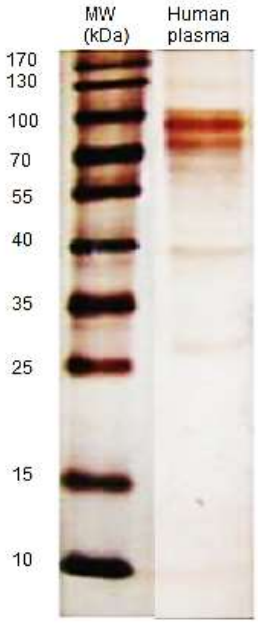

Figure 1.11. SDS-PAGE of a human plasma sample.

Adapted from [16].

A SDS-PAGE assay of healthy human plasma (**Figure 1.11**) generally shows one set of higher molecular weight proteins ranging from 100 to 70 kDa, which represent the most abundant plasma proteins. Two dim bands at around 40 and 25 kDa also indicate the presence of scarcer low molecular weight proteins in blood plasma [16,17]. Total protein quantification of the blood plasma proteins was performed by Okutucu *et al.* by comparing five methods (**Table 1.2**), and the average concentration of plasma proteins in blood is 93.96 g/L [18].

Table 1.2. Average plasma protein concentrations determined using five different methods [18].

Method	Plasma concentration (g/L)
Amido Black	83.4 ± 1.93
Lowry	110.2 ± 4.09
Bradford	95.1 ± 3.3
Biüret	88.8 ± 3.54
Ponceau-S/TCA	92.3 ± 5.71

1.2. Plasma adsorbome

Work performed by Walkey and Chan enabled the identification of a set of 125 plasma proteins that interact with at least one nanomaterial entity, and named it plasma adsorbome. These proteins are involved in diverse physiological functions, more specifically in lipid and ion transport, blood coagulation, immune complement activation, and pathogen recognition [19]. One of the main focuses during the development of this dissertation was to understand electrostatic interaction between the most abundant plasma proteins and nanoparticles upon injection in the bloodstream (**Figure 1.12**).

Figure 1.12. Schematic of a human blood vessel with the blood's main components: erythrocytes (big red disks), leukocytes (white circles) and thrombocytes (small light purple disks); as well as nanoparticles (yellow spheres).

1.2.1. Human serum albumin

Human serum albumin (HSA) is the most abundant protein in plasma making up more than half of the total plasma protein content, and is involved in the following physiological functions: (1) Oncotic pressure maintenance in the liver, (2) Biomolecule, ion, metal and drug transport, (3) Antioxidation defense, (4) Metabolic acid-base buffering system, and (5) Enzymatic activity. This globular 66,478 Da protein is synthetized in the liver and circulates between the plasma and the interstitial space [20–22]. Albumin's quaternary structure (**Figure 1.13**) is conserved throughout the entire mammalian class and minor sequence divergences are due to speciation events. This homotrimer has a predominant α-helix motif held by 17 disulphide bonds. Its three active sites harbour a hydrophobic environment for ligand binding [20].

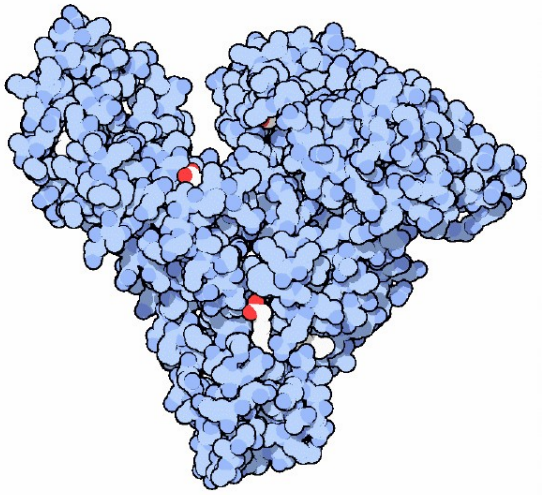

Figure 1.13. Quaternary structure of human serum albumin bound to three fatty acids [20].

This protein is highly soluble due to its high content in both acidic and alkaline residues, and for this reason its concentration in plasma can reach values up to 0.6 mM [22]. The isoelectric point of human albumin is 4.7, so at physiological pH this protein has a high negative net surface charge. Binding of ions and metals, fatty acids, hormones and various drugs occurs by hydrophobic interactions with the non-polar residues at albumin's three hydrophobic pockets [22]. Albumin is also the main component of the biocorona in citrate-functionalized gold nanoparticles [3,4]. The adsorption of this protein to the nanoparticle surface is led by its alkaline residues, which interact ionically with the citrate capping agent by electrostatic forces [3,4].

1.2.2. Human plasma fibrinogen

Fibrinogen is the second most common blood protein, taking part in the coagulation cascade [23]. This glycoprotein consists in pairs of three different polypeptide chains (α, β and γ) linked by disulphide bonds (

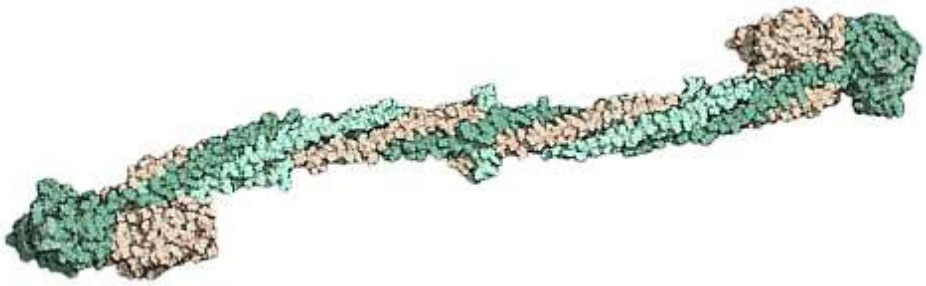

Figure 1.14) [24,25]. This 340 kDa rod-like shape protein is produced by the hepatocytes in response to tissue injury, infection or inflammation. During blood coagulation, fibrinogen in cleaved by thrombin resulting in fibrin monomers that polymerize and became insoluble, creating a blood clot [23].

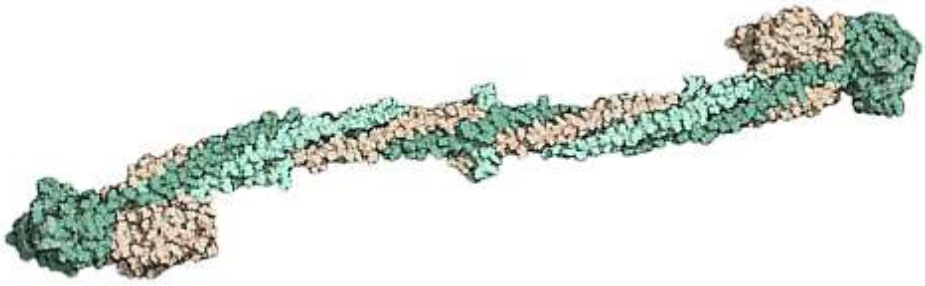

Figure 1.14. Human fibrinogen. αα', ββ' and γγ' chains are colored light-green, grey and dark-green, repectively [26].

Fibrinogen shows a negative net charge at physiological pH due to its isoelectric point of 5.2. The central region of the protein exhibits negative charge; however arginine and lysine residues at the two α chains result in local positive charge which can interfere with adsorption to nanoparticles, promoting a specific side-on orientation and allowing for multiple layer formation [24,25].

1.2.3. Human transferrin

Transferrin is the major iron transporter in the plasma that, together with a membrane transferrin receptor, controls iron levels in the bloodstream (**Figure 1.15**). Iron binding is a primitive biological function, as so the transferrin protein family is highly conserved in vertebrate and non-vertebrate organisms [27,28].

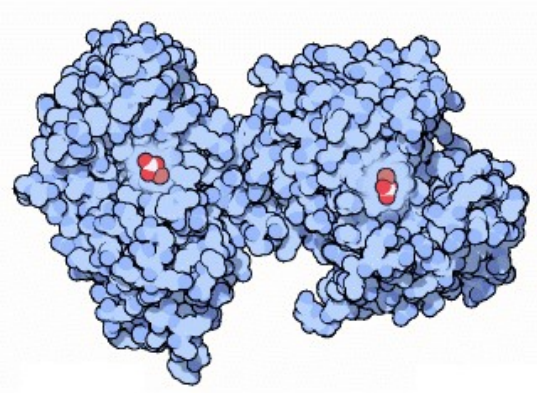

Figure 1.15. Transferrin's bilobal structure bound to two ferric ions (brown) and two carbonate ions (red and white) [29].

This 80 kDa protein holds two variable heterossacharide chains branched out from asparagine residues at the C-terminal, representing as much as 6% of the its total molecular weight. The terciary structure is composed of two non-identical lobes corresponding to the two iron-bonding domains at the N and C-terminals [24]; at physiological pH this protein's isoelectric point varies from 5.4 to 5.9 depending on its carbohydrate content.

1.3. Nanoparticle and bionanoconjugates characterization

Colloidal nanoparticles exhibit three significant differences in comparison to their respective macroscopic materials: their high surface to volume ratios, their chemical reactivity and quantum effects of the molecular orbitals, which originates chemical, optical, electrical, thermal and magnetic characteristics, unique at the nanoscale. Such effects shaped the impact of nanotechnology in a number of scientific, technical and industrial fields [2,10,12].

Considering their tuneable size, surface functionalization and biomolecular immobilization abilities, gold nanoparticles can be used as biochemical sensors. Molecular diagnostics using nanomaterials have pushed technological developments further in order to enhance detection and characterization of nanoparticle-based bioanalytical devices (**Figure 1.16**) [12].

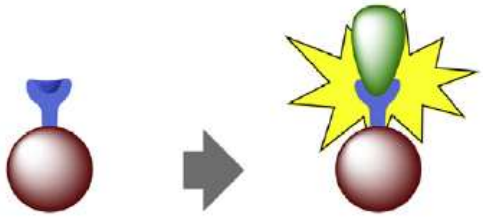

Figure 1.16. Schematics of a standard nanoparticle sensor composed of AuNP (red), recognition molecule (blue), and analyte (green) [12].

The signalling event created by the interaction of an analyte with the recognition molecule bound to a nanoparticle is the basis of these bionanosensors; which have been successfully used in functional and monitoring analysis of biomolecules in organisms, environmental samples and food industry [12].

The composition and structure of adsorbed biomolecules to a metallic nanoparticle surface forming a bionanoconjugate at physiological environment, can be assessed by addressing five specific parameters: (1) thickness and density of the bionanoconjugate, (2) identity and quantity of existing biomolecules, (3) arrangement and orientation of molecules at the NP's surface, (4) adopted conformation of adsorbed biomolecules, and (5) affinity of biomolecules to the nanoparticle surface [19]. **Table 1.3** shows the techniques used to examine the structure and composition of the protein corona of nanoparticles.

Table 1.3. Techniques to examine the protein corona of nanoparticles [19].

Corona parameter	Techniques
Thickness	Dynamic light scattering, differential centrifugal sedimentation, size exclusion chromatography, transmission electron microscopy, nanoparticle tracking analysis.

Density	Colorimetric protein assays, protein electrophoresis.
Identity and quantity	Circular dichroism, fluorescence quenching, computational simulation.
Affinity	Size exclusion chromatography, surface plasmon resonance, isothermal titration calorimetry.

1.3.1. UV-Vis spectroscopy

UV-Vis spectroscopy measures absorption or scattering events produced by electronic transitions happening in atoms and molecules. In absorption spectroscopy, ground state electrons absorb photons and transit to higher energy excited states. Fluorescence spectroscopy is complementary to this technique, because it deals with light emission of excited molecules or atoms to their ground state [8].

The absorbance maxima in the ultraviolet-visible-infrared (300-900 nm) regions of the electromagnetic spectrum (

Figure 1.17) provide crucial information about nanoparticle size and shape; as so for particle aggregation which can be detected in the visible light region (400-700 nm) by the human eye [8].

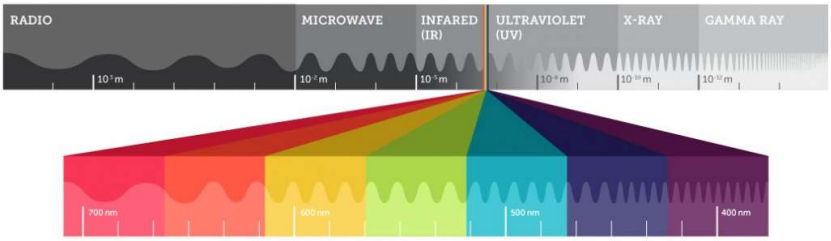

Figure 1.17. Electromagnetic spectrum zoomed in the visible light region 30.

Gold atoms have the electronic configuration of $1s^2\ 2s^2\ 2p^6\ 3s^2\ 3p^6\ 4s^2\ 3d^{10}\ 4p^6\ 5s^2\ 4d^{10}\ 5p^6\ 6s^1\ 4f^{14}\ 5d^{10}$. Light absorption of *d*-orbital electrons on gold nanoparticles enables transition to higher energy *sp*-orbitals with the energy of *circa* 2.4 eV, generating the SPR effect at 520 nm. This absorption of green visible light at this wavelength corresponds to the red color observed in spherical gold nanoparticles [31].

1.3.2. Dynamic light scattering

Dynamic light scattering (DLS) technique provides information on single scattering events intrinsic to suspended materials by detecting intensity variances over time [7,32–34]. The interaction of a monochromatic laser beam with suspended molecules scatters the incident light by propagating them out from their original direction. The nanoparticles' alternating positions promote continuous light interference resulting in intensity fluctuations detected over time, which contain information about the time scale of the scattering movement [33,34] (**Figure 1.18**).

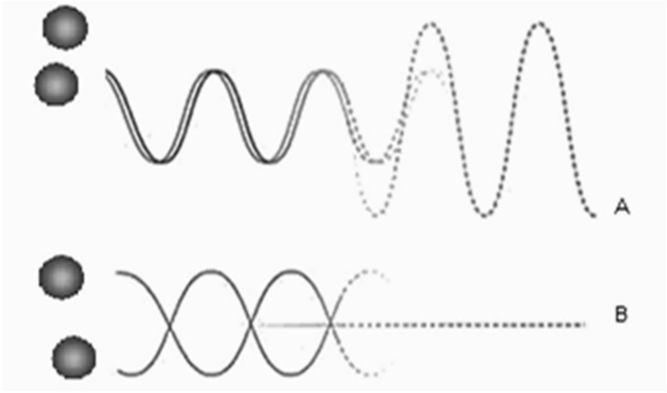

Figure 1.18. Light scattering on colloidal nanoparticles causes constructive (**A**), and destructive (**B**) wave interference.

The deviated light intensity is not constant because gold nanoparticles in suspension continuously collide with solvent molecules displaying random Brownian motion [33], which is modelled by the Stokes-Einstein equation ($D_h = \frac{k_B T}{3\pi\eta D_t}$, **Equation 1.1**). As we can observe from $D_h = \frac{k_B T}{3\pi\eta D_t}$, **Equation 1.1**, particle size is an important parameter in DLS technique. Particles much larger than the incident wavelength diffuse slowly through the solvent, leading to less detected intensity variations over time. Similarly, smaller particles move much faster and show substantial intensity changes over time [33,34].

$$D_h = \frac{k_B T}{3\pi\eta D_t}, \qquad \textbf{Equation 1.1.}$$

where D_h represents the hydrodynamic radius of the molecule, k_B is the Boltzmann constant and T the absolute temperature, η is the medium viscosity and D_t represents the molecule translational diffusion coefficient.

Applying an autocorrelation function to the intensity data acquired enables comparison between intensity signals at different times of the experiment, elucidating on the dynamics of the system. When comparing the intensity at a certain time t to the intensity at a tiny fraction of time later (δt), these signals show strong similarity and therefore are well correlated. This correlation between signals decreases over time due to the Brownian characteristic of suspended samples, described by an exponentially decaying function ($C(\tau) = 1 + \beta . e^{-2\Gamma\tau}$, with $\Gamma = \left[D_t . \frac{4\pi\eta}{\lambda} . \sin\left(\frac{\theta}{2}\right)\right]^2$, **Equation 1.2**). Cumulants analysis is performed on the data by fitting the correlation function to an exponential one, enabling the determination of mean size or dispersity index of the sample [33].

$$C(\tau) = 1 + \beta . e^{-2\Gamma\tau}, \text{ with } \Gamma = \left[D_t . \frac{4\pi}{\lambda} . \sin\left(\frac{\theta}{2}\right)\right]^2, \qquad \textbf{Equation 1.2.}$$

where β represents the intercept of the correlation function, D_t is the translational diffusion coefficient, λ is the laser wavelength and η the medium refractive index, and θ is the scattering angle.

Solution heterogeneity is a major issue when performing DLS experiments. Applying the Rayleigh approximation to $(I = I_0 \frac{1+\mathrm{co}\ ^2\theta}{2R^2}\left(\frac{2\pi}{\lambda}\right)^2\left(\frac{n^2-1}{n^2+2}\right)^2\left(\frac{d}{2}\right)^6,$ **Equation 1.3**$I = I_0 \frac{1+\cos^2\theta}{2R^2}\left(\frac{2\pi}{\lambda}\right)^2\left(\frac{n^2-1}{n^2+2}\right)^2\left(\frac{d}{2}\right)^6,$ **Equation 1.3**), the amplitude (λ) of the scattered light of a sample varies as the sixth power of its size (d) [8,33]. So the light intensity detected from a nanoparticle can be masked by the scattering of a larger contaminant, *i.e.* nanoparticle or protein aggregates.

$$I = I_0 \frac{1+\cos^2\theta}{2R^2}\left(\frac{2\pi}{\lambda}\right)^2\left(\frac{n^2-1}{n^2+2}\right)^2\left(\frac{d}{2}\right)^6, \qquad \textbf{Equation 1.3.}$$

1.4. Electrophoresis-based techniques

Owing to the fact that most of all biological molecules are charged, electrostatics plays an important role in inter and intra-molecular interactions [19,35,36]. Applying an electric field to charged particles is a well-established separating method; in which a porous polymeric matrix serves as physical support for the molecules to migrate according to its size and/or net charge [19,35,36] (**Figure 1.19**).

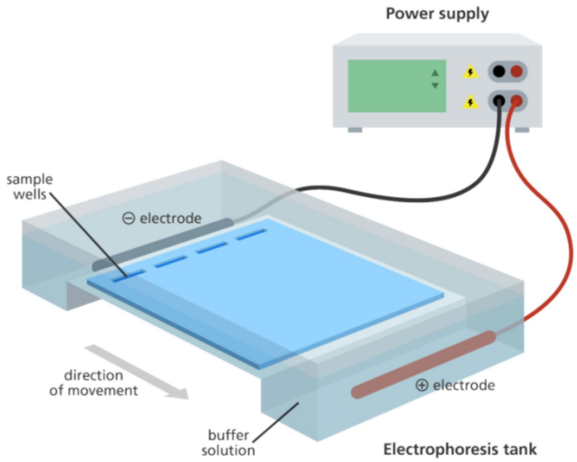

Figure 1.19. Agarose gel electrophoresis setup [37].

1.4.1. Denaturing polyacrylamide gel electrophoresis

When separating biomolecules by their size, a previous denaturation step is required to assure equal net charge of the samples. Polyacrylamide gel electrophoresis (PAGE) is usually performed on proteins after heat denaturation in the presence of the anionic surfactant sodium dodecyl sulphate (SDS). This promotes disruption of weak bonds and loss of secondary and

partial tertiary and quaternary structure, resulting in a non-functional rod-like shape protein [38]. Reduction of disulphide bonds by β-mercaptoethanol (βME) can be performed to disrupt these bonds that promote tertiary or quaternary structures (**Figure 1.20**).

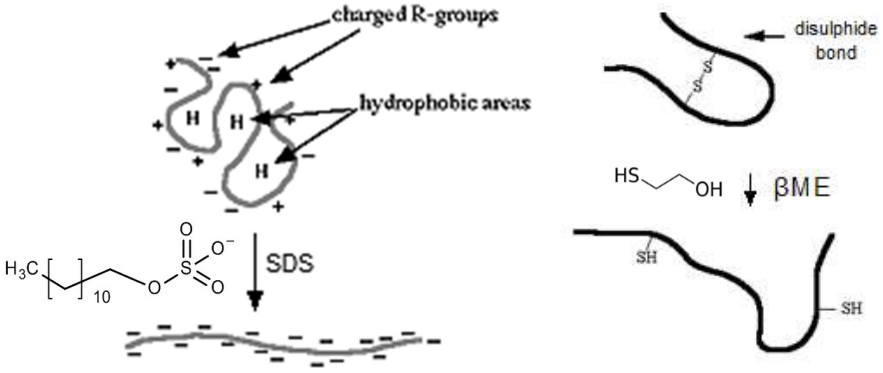

Figure 1.20. Action of SDS and βME on a native protein structure. *Adapted from* [39].

1.4.2. Agarose gel electrophoresis

Considering that protein adsorption generally occurs by electrostatic interaction of opposite charged residues [3,4,35], the global charge of gold nanoparticles is reduced when conjugated with proteins. The surface charge of bionanoconjugates is therefore less negative; as they require fewer applied electric voltage to achieve electrostatic neutrality, ceasing its migration sooner than free nanoparticles. These migrated distances can be defined as electrophoretic mobility ($\mu_e = \frac{v_e}{E}$, **Equation 1.4**).

$$\mu_e = \frac{v_e}{E}, \qquad \textbf{Equation 1.4.}$$

where v_e represents the drift velocity of the bionanoconjugates and E is the applied electric field.

The variation of electrophoretic mobilities of bionanoconjugates can be related to the degree of protein coverage of nanoparticles [1,35]. Higher mobility values correspond to a loosely packed bionanoconjugate; while tightly-packed bionanoconjugates display lower migration distances and electrophoretic mobility values. The unified theory for gel filtration and electrophoresis developed by Rodbard and Chrambach predicts the relationship between electrophoretic mobility, partition coefficient, gel concentration, and molecular radius ($log(\mu_e) = log\ _0) - K_r\,.T$, **Equation 1.5**), enabling the determination of zeta-potential of bionanoconjugates [19,35,36,40].

$$log(\mu_e) = log\ _0) - K_r\,.T, \qquad \textbf{Equation 1.5.}$$

where μ_0 represents electrophoretic mobility in the absence of agarose, K_r is the retardation coefficient and T is agarose percentage of the gel.

1.4.3. Zeta-potential

All materials acquire surface charge when dissolved in a polar medium; inducing solvent flux in a very particular way, and creating a so-called electric double-layer (EDL) around the solute molecules [3,19,32,41] (**Figure 1.21.** Model of the electric double-layer at a charged interface in aqueous solution. *Adapted from* [41].**Figure 1.21**). Ion distribution at the EDL creates three distinct regions: (1) the Stern layer is the solvated area closest to the molecular surface. It is considered immobile, and exhibits high counter-ionic density, giving rise to greater electrical potential values (ψ_δ). The outer region (2) is termed the diffuse layer, where electrical and thermal forces influence ion diffusion. From this point on, electric potential decreases exponentially with distance and achieves neutral values in the bulk solvent (3) [40–42].

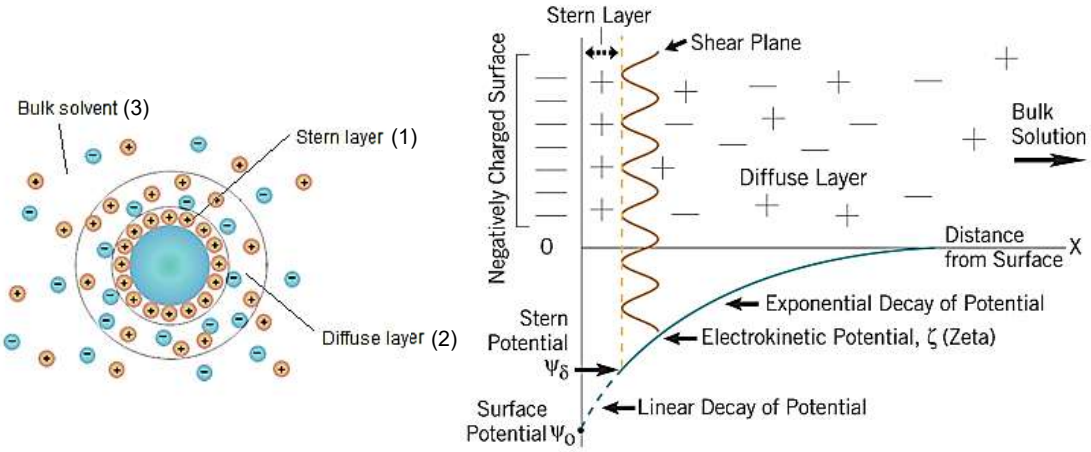

Figure 1.21. Model of the electric double-layer at a charged interface in aqueous solution. *Adapted from* [41].

Zeta-potential (ζ) is an indirect measurement of the electrical potential at the partition between the Stern and the diffuse layers, also called the shear plane. In practical terms, the zeta potential of a solute is frequently taken to be the identical as the Stern potential; and as so has become a useful parameter in monitoring changes in electrokinetic behaviour of suspensions [41].

A potentially stable colloidal system has solid charged particles dispersed in liquid solvent, whose zeta-potential values fall inside the range of ± 30 mV due to electrostatic stabilizing repulsion forces. A decrease in zeta-potential values of suspended particles can disrupt colloidal stability and promote particle flocculation [41].

By the fact that solutes in suspension exhibit surface charge, the application of electric field to the medium can induce migration effects on the particles. Therefore, electrophoretic mobility for

zero agarose percentage (μ_0) and zeta-potential (ζ) can be interconverted using the following expression [40] ($\zeta = \frac{3\eta_s\mu_0}{2\epsilon_s.H(\kappa R)}$, **Equation 1.6**).

$$\zeta = \frac{3\eta_s\mu_0}{2\epsilon_s.H(\kappa R)} , \qquad \textbf{Equation 1.6}$$

where η_s is the medium viscosity and ϵ_s the relative permittivity of the solvent. $H(\kappa R)$ is the Henry function, in which the Smoluchowski approximation of $H(\kappa R)$≈1.5 is used for a large electrolyte layer (κ) value; dependent on the particle geometric radius R.

When specific adsorption takes place at suspended molecules, the ionic response of the solvent is altered, usually by increasing the molecular weight of the species. This shifts the shear plane further away from the Stern layer; thus changing the zeta potential in regard to the free solute. Consequently, this electrokinetic parameter can effectively show particle surface charge in solution [41].

1.5. Computational modelling of protein-nanoparticle interaction

The description of the mechanism of protein adsorption to nanoparticles is dependent not only in experimental data, but also in computational results. Hence, computational methods were used with the intention of (1) performing surface charge studies of plasma proteins, (2) making docking experiments with capping agent CALNN on plasma proteins, (3) automate experimental results with agarose gel digital images processing, (4) fit adsorption models on these experimental results; and (5) use geometric packing systems to determine protein to nanoparticle ratios forming a monolayer protein corona.

Computational simulation of protein-nanoparticle and inter-protein interactions provides information on protein's physicochemical properties and conformation within a short time frame, enabling the visualization at atomic resolution over femtosecond timescales [19]. Several strategies can be applied to simulate protein adsorption to a nanoparticle [19]. For example, Zuo and colleagues have successfully predicted by computational means the maintenance of enzymatic activity after adsorption to a NP [43]; however the complexity of protein adsorption at physiological media is yet to be perfected through solvation descriptors and relevant force fields within the models [19]. Alternative methods can be applied to predict this interaction, by combining computational and experimental approaches on bionanoconjugates, and the ones used throughout this work are described below.

The following computational approaches were done in order to obtain different parameters which can be combined and interpreted to describe a mechanism of protein adsorption to nanoparticles after entrance in the bloodstream.

1.5.1. Analysis of electrophoretic mobility on agarose gels

One of the parameters studied when working with bionanoconjugates is the electrophoretic mobility, determined by their surface charge and molecular weight. Digital images of electrophoretic mobility assays can be processed using the eReuss application (source code freely available at https://github.com/lkrippahl/eReuss) with the purpose of avoiding errors caused by direct measurement of the migration distances by enhancing gel analysis automation.

Migration distances of an electrophoretic assay are usually obtained using a ruler, by measuring from the top of the gel to the sample band front. This type of direct measurement is frequently associated with systematic errors intrinsic to the operator and the instrument itself. The sensibility of a metric ruler is 0.5 mm, *i.e.* half of the smallest division, the millimetre. Bioconjugates of gold nanoparticles generally show differences in migration in this error range, so interpretation of the results tends to be faulty and uncertain.

The eReuss program detects the position of migrated samples in electrophoretic gels by relating it with the highest intensity pixels of each gel lane. The colored digital images are converted to greyscale by selecting the color channel closest to the sample color. In this way, the digital image will carry only brightness intensity information, from black having the weakest light intensity to white at its strongest (**Figure 1.22**); relating to the distribution of samples throughout the agarose gel lane. For gold nanoparticles the light intensity in the red color channel is selected, and the gel digital image is represented exclusively in shades of grey.

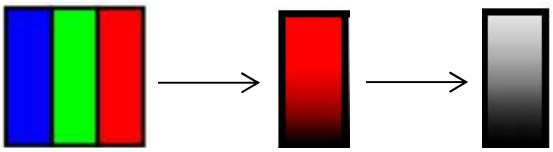

Figure 1.22. Color to greyscale conversion using intensity of the red color channel.

The migrated distance for each bionanoconjugate samples is identified by detection of maximum intensity brightness, and intensity profile is displayed along the gel lanes. Gaussian functions are fitted to the maximum intensity values to assign them the migrated position for each sample (**Figure 1.23**).

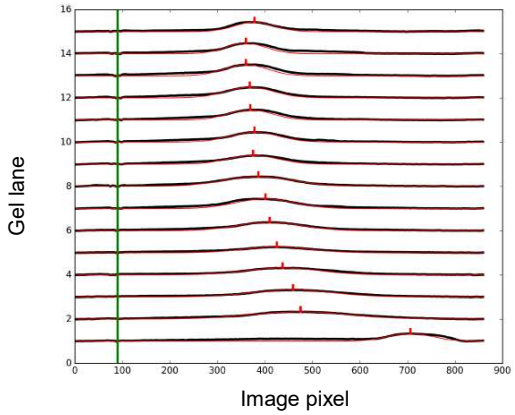

Figure 1.23. Peak identification step in eReuss program. *From the eReuss user manual.*

This application also provides some interpretation of the electrophoretic mobilities obtained. By fitting a Langmuir isotherm to the data, the protein binding constant to nanoparticle is determined; providing information on the affinity for the nanoparticle surface for each plasma protein. A Hill cooperativity plot can also be obtained, whose Hill coefficient and dissociation constant can elucidate about protein-protein interactions on the nanoparticle surface.

On a practical point of view, the analysis of an agarose gel digital image requires the following steps:

1) The digital photos undergo a first preprocessing step, in which the contrast and color channel are specified in order to improve the detection of the intensity of the migration bands.

2) The specification of the region of interest in the digital image ensures the correction of image orientation and the dimensions of the agarose gel and well comb; and also the number of used wells. This step defines the number of migration bands to be detected.

3) The lane identification step enables correction of the position of each lane, as well as the concentration ratios specification for each lane, to be used further on Langmuir and Hill plots.

4) In band profiling the average brightness intensity is measured along each lane and represented as black lines. Red lines show Gaussian curves that fit the intensity maximum. The resulting file shows a plot, in which the vertical scale represents the peak positions for each lane, and image pixels as the horizontal one. The computed migration distances gathered from the maximum intensity fitted peak are used to determine electrophoretic mobility (μ_e) values using $\boldsymbol{\mu e} = \frac{v_e}{E}$, **Equation 1.4**.

5) The final report enables the specification of the electrophoretic assay conditions: time, voltage, and agarose concentration. A Langmuir adsorption isotherm and Hill equation plot can also be produced using the maximum intensity values, providing information on adsorption and cooperativity behaviour of the bionanoconjugates.

1.5.2. Electrostatic potential surface

The hydration shell around a protein is fundamental to biological function [44]. Implicit solvent models describe polar solvent medium as a continuous field showing average properties of the real solvent, and surrounding the solutes at their van der Waals surface (**Figure 1.24**).

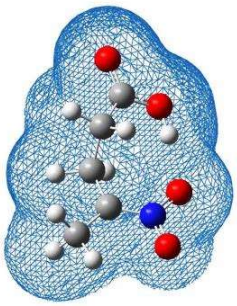

Figure 1.24. Implicit solvation model of a small molecule [45].

The Poisson-Boltzmann equation utilizes implicit solvation to describe the electrostatic potential and equilibrium distribution of ions around a solvated macromolecule (**Figure 1.25**). A three-dimensional grid is built around the molecule; and for each grid cell electrostatic potential is determined, generating an electrostatic potential map.

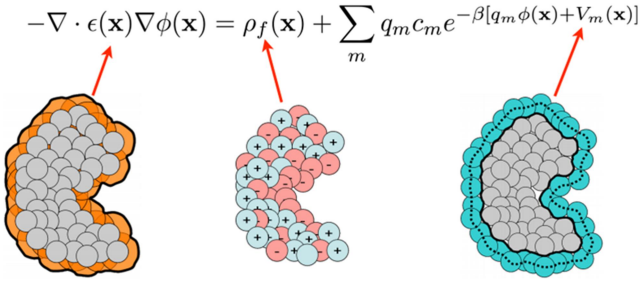

Figure 1.25. Oversimplified Poisson-Boltzmann equation [44].

The coefficients on this differential equation are related to the molecular structure. The dielectric function $\epsilon(x)$ describes change in local polarizability; $\rho_f(x)$ is the charge density in a grid cell, and the latter coefficient is based on van der Waals volumes V_m. The Poisson-Boltzmann model can be used to predict the electrostatic surface potential and solvation energies of proteins, useful in interaction site identification [44].

1.5.3. Estimation of a protein monolayer around a nanoparticle

The prediction of the silhouette of several plasma proteins enables estimation of the number of proteins at the nanoparticle surface. The van der Waals radius [46] ($r_w = \sqrt[3]{\frac{3V_w}{4\pi}}$, **Equation 1.7**) can be used to model the occupied volume of each atom in a protein. The projected areas of several protein orientations are determined, and these values are used

to estimate the number of proteins around a nanoparticle, when a monolayered protein corona is formed.

$$r_w = \sqrt[3]{\frac{3V_w}{4\pi}}, \qquad \textbf{Equation 1.7.}$$

where V_w is the van der Waals volume and r_w the van der Waals radius.

1.5.4. Protein-ligand docking

Molecular docking is a computational modelling method for identifying the preferred orientation between two molecules when forming a stable complex; and consists in (1) exploring the ligand's possible orientations, and (2) ranking the results to determine the best binding mode for each protein-ligand complex (**Figure 1.26**) [47].

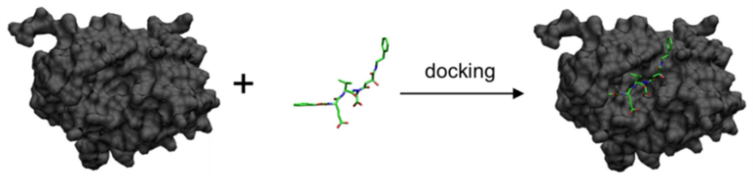

Figure 1.26. Schematic illustration of protein-ligand docking.

Docking assays usually start by producing a conformer library of a known ligand; by creating a set of three-dimensional molecule orientations, also considering bond flexibility. This searching step relies on systematic or stochastic exploration methods for conformer prediction. The searching algorithms utilised should depend on the system at study, and the objective of the docking experiment [30]. A scoring function is afterwards applied to rank the produced binding modes. Scoring functions can be empirical, knowledge-based of molecular mechanics-based; and again, each approach needs to be properly selected in order to originate the most representative protein-ligand complex [47].

By decreasing the accuracy of the search space, lowering energy differences on the protein structure, and increasing number of binding modes generated; a huge number of CALNN orientations are obtained as result from the docking assay. The obtained ligand 'family' is then represented on the protein structure in order to access if any particular local in the protein shows a higher affinity for the CALNN capping agent.

This approach contradicted the purpose of traditional ligand-protein docking experiment, in which the ligand best binding mode has the highest score and represents the most probable binding orientation of the ligand to the protein. During these docking assays the preferential interaction sites for several CALNN capping agents on three plasma proteins were identified without searching for the best binding modes; but for their distribution at the protein's surface.

These docking results could be interpreted as a representation of multiple peptide molecules anchored on a nanoparticle, interacting with specific sites of several circulating plasma proteins (**Figure 1.27**).

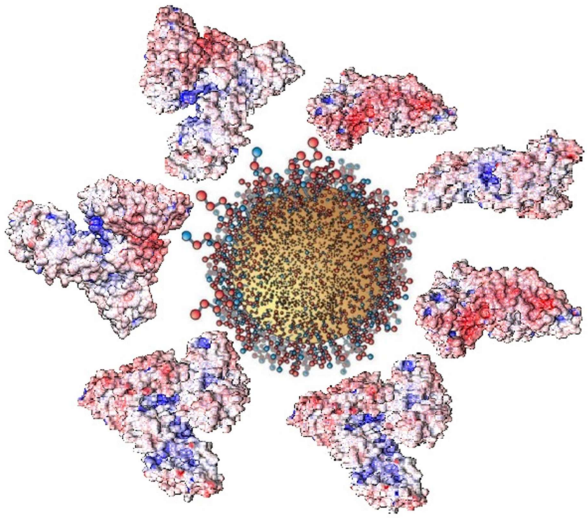

Figure 1.27. Schematic illustration of albumin corona on a nanoparticle. *Nanoparticle model adapted from* [48].

1.5.5. Protein adsorption models and assumptions

1.5.5.1. Langmuir adsorption model

Modelling the adsorption and kinetics happening in nanoscale interactions, such as adsorption of proteins to gold nanoparticles, is based on the concept of Langmuir adsorption layer [49,50]. His hypothesis states that molecular species adsorb to a homogenous solid surface with constant binding energies, independently of reactant quantity and surface coverage. The affinity constant of the molecules forming the first layer is much greater than the one between the first and second layers [50]. This model can be described using a Langmuir adsorption isotherm ($\Theta = \frac{K_{eq}[protein]}{1+K_{eq}[protein]}$, **Equation 1.8**).

$$\Theta = \frac{K_{eq}[protein]}{1+K_{eq}[protein]}, \qquad \textbf{Equation 1.8.}$$

where Θ represents the occupation factor of the adsorption sites, and K_{eq} the binding constant for a given protein.

Figure 1.28 shows a standard Langmuir isotherm plot, in which adsorbate concentration (χp) rises as molecules adsorb to the surface, until reaching full surface coverage at the highest occupancy factor.

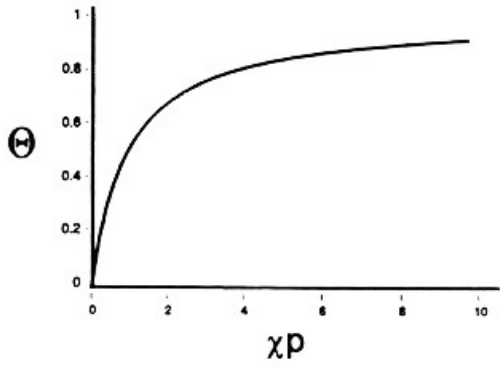

Figure 1.28. Langmuir adsorption isotherm.

1.5.5.2. Hill cooperativity model

Langmuir adsorption isotherm is formally equivalent to the Hill equation ($\theta = \frac{[ligand]^n}{K_d+[ligand]^n}$, **Equation 1.9**), which describes the concentration influence in kinetics of ligand binding to a protein (**Figure 1.29**). The Hill coefficient (n) in the equation quantifies cooperativity effects [51].

$$\theta = \frac{[ligand]^n}{K_d+[ligand]^n}, \qquad \textbf{Equation 1.9.}$$

where θ represents the occupation fraction, n the Hill cooperativity coefficient and K_d the ligand's dissociation constant.

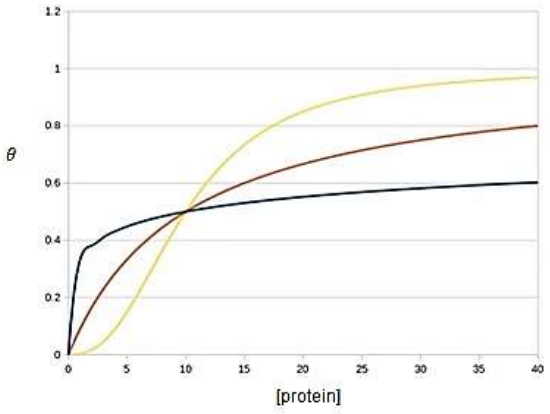

Figure 1.29. Hill equations for negative (blue), positive (yellow) and non-cooperative (red) binding behaviour of a ligand to a protein.

1.5.5.3. Face-centered cubic for nanoparticle atomic packing

Face-centered cubic (fcc) is the usual crystalline structure of gold atoms in a nanoparticle, as described by Petkov *et al.* [52] (**Figure 1.30 A and B**). It has the highest packing efficiency within the cubic crystal system (74 %) with a coordination number of twelve. Each fcc unit cell holds four similar atoms (**Figure 1.30 C**).

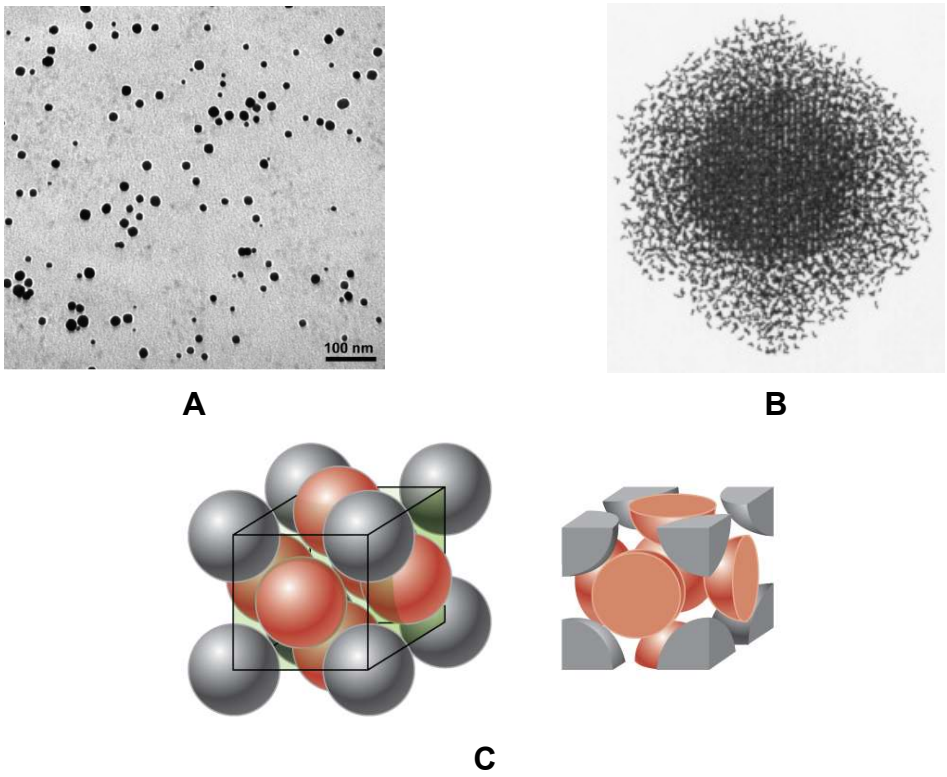

Figure 1.30. TEM image of 15 nm gold nanoparticles (A), computational model of 3 nm gold nanoparticle in water (B), and face-centered cubic unit cell representations (C) [52].

Computational and experimental data obtained by Kao *et al.* provided an adequate description of the three-dimensional structure of gold nanoparticles as showing a face-centered cubic packing geometry [53]. In addition, work by Liang *et al.* showed that the packing geometry of protein structure could also be described using a face-centered cubic system model. With this, it is reasonable to assume that protein adsorption phenomena would happen with similar packing between proteins and the nanoparticle surface, and would show the same fcc geometry.

2. Objectives and main focuses

Protein adsorption to nanoparticles in the blood is still an unclear mechanism. The formation of a protein corona is dependent on protein binding affinities and concentrations intrinsic to this system, as well as nanoparticle size and type of surface functionalization. Multiple physiological factors also affect the corona's protein composition. Due to strong SPR absorption in the UV-Vis spectrum region, nanoparticles provide a highly sensitive detection system which has been applied in therapeutics and diagnostics, scientific research, environmental, and industrial fields.

Computational methods will enable the electrostatic study of the surface charge distribution on plasma proteins, and their possible interaction sites with CALNN-functionalized nanoparticles. Using some theoretical assumptions on packing geometry around nanoparticles, the number of proteins forming a monolayer corona can be predicted for albumin, transferrin and fibrinogen. Electrophoresis assays on bionanoconjugates of plasma proteins will be able to confirm the formation of a protein corona on gold nanoparticles by the difference in migration distances, which is related to molecular weight and surface charge of bionanoconjugates and free nanoparticles. This technique also allows for determination of zeta-potential values of bionanoconjugates by relating electrophoretic mobilities in the presence of increasing agarose media. Comparison of hydrodynamic radii measured by dynamic light scattering data, the size of bionanoconjugates can be determined and the layer architecture of the protein corona can be suggested.

By combining these very distinct experimental and computational data, a small step to the description of the adsorption mechanism of proteins to nanoparticles can be taken, and future perspectives on this subject include protein affinity constants determination using kinetic assays, pH dependency assays of protein adsorption, additional computational simulations of proteins and nanoparticle properties and interactions.

Blank page

3. Methods

3.1. AuNP synthesis by citrate reduction method

The required glass materials were previously immersed in *aqua regia* (1:3 nitric acid (HNO_3) and chloride acid (HCl)) and washed thoroughly with Mili-Q water. During the last wash the pH was monitored using pH indicator strips (Macherey-Nagel, pH-Fix 0 – 14), and the value of pH established was 7. 100 mL of 30% (w/w) Au (III) chloride solution in diluted HCl (Sigma, 99.99% purity, boiling point (BP)=254 ^{o}C, molecular weight (MW)=339.79 Da, density (ρ)=1.637) were added to a round-bottom flask under gentle agitation and kept away from sunlight. The solution was boiled for 1 h and then 10 mL of 1% (w/v) sodium citrate tribasic dihydrate (Sigma, MW=294.10 Da, pH=7.0-9.0 at 25 ºC) were gently added and the mixture was left to reduce for 15 min. After this time, the colloidal nanoparticles were cooled for about 2 h, and divided into two aliquots of *circa* 50 mL each. These aliquots were refrigerated at 4 ºC and kept away from sunlight. The UV-Vis 900-300 nm absorbance spectrum of a 1:6 solution of the resulting nanoparticles was obtained using a VARIAN Cary 50 Bio spectrophotometer, and the diameter and concentration of the nanoparticles were determined according to the relation described by Haiss *et al.* [54]. The synthesis was repeated as many times as necessary for the nanoparticle quantities used in the following assays.

3.2. AuNP functionalization with CALNN

Freshly synthetized AuNPs were functionalized with 1:1000 [AuNP]/[CALNN] ratio of CALNN peptide 4.68 mM overnight at room temperature and kept away from sunlight, after which a second UV-Vis 900-300 nm absorbance spectrum of the solution was obtained, in the same conditions as above. Functionalization was performed as many times as necessary for the quantities used in the following assays.

3.3. *Bionanoconjugates electrophoretic mobility assay*

AuNP-CALNN conjugates of human serum albumin (HSA), human transferrin (HT) and bovine plasma fibrinogen (BPF) were produced by overnight incubation at 4 ºC of increasing volumes of HSA solution (Sigma, lyophilized powder ≥97% purity, MW=66.478 Da), HT solution (Sigma, powder ≥98% purity, MW=76.000-81.000 Da), BPF solution (Sigma, powder, Type I-S, 65-85% protein, ≥75% of clottable protein, MW=340.000 Da) and two human plasma samples (kindly provided by Instituto de Medicina Molecular (IMM) and Marta Giza (MG)) on aliquots of 500 µL of AuNP-CALNN nanoparticles, resulting in increasing [protein]:[AuNP-CALNN] ratios. These samples were then centrifuged for 5 min at 4 ºC and 19173.7 g (Centurion Scientific K3 Series centrifuge, BRK5424 rotor) and the supernatant was removed. The pellets were resuspended in 13.5 µL of 5 mM phosphate buffer pH=7.2 and 1.5 µL of glycerol and then loaded on a 0.5% (w/v) agarose (invitrogen, UltraPure™ Agarose) gel in ⅛x tris-acetate-EDTA (TAE) buffer, and ran using a Bio Rad PowerPac™ Basic power supply (electrode separation 15 cm, E=10 V/cm) at 150 V, 400 mA for 30 min. The digital gel image processing and

Langmuir and Hill plots, and the respective binding constants, were produced using the eReuss software package. This protocol was repeated until meaningful results were obtained.

3.4. Bionanoconjugates incubation-time dependency adsorption

2.79 nM AuNP-CALNN nanoparticles were conjugated with 1 g/L HSA with increasing [HSA]:[AuNP-CALNN] ratios using the protocol mentioned in ***3.3***, varying the incubation time (1 h, 3 h, 7 h, 24 h). Each sample was then loaded on a 15-well 0.5% (w/v) agarose gel (invitrogen, UltraPure™ Agarose) run for 30 min at 150 V, 400 mA. This protocol was repeated until meaningful results were obtained.

3.5. Zeta-potential determination using agarose gel electrophoresis

1.1 nM AuNP-CALNN nanoparticles were conjugated with 1 g/L HSA using the protocol mentioned in ***3.3***, and then loaded on a 15-well agarose (invitrogen, UltraPure™ Agarose) gel with increasing agarose percentages from 0.3-2.0% (w/v) ran at 150 V, 400 mA for 50 min. The migration distances were obtained using the eReuss application as explained previously. Following the procedure described by Pons *et al.* the respective electrophoretic mobilities for each [HSA]:[AuNP-CALNN] ratio were plotted *versus* gel concentration [40] in order to determine the zeta-potential of free nanoparticles and bionanoconjugates, using $\zeta = \frac{3\eta_s \mu_0}{2\epsilon_s . H(\kappa R)}$, **Equation 1.6** (see ***1.4.3. Zeta-potential***). This protocol was repeated until meaningful results were obtained.

3.6. Light scattering assays

Dynamic light scattering measurements of the particle size of AuNP-CALNN bionanoconjugates and unconjugated HSA, bovine serum albumin (BSA, Sigma, lyophilized powder, ≥96% purity, MW=66.000 Da) HT and BPF were performed on a Horiba's SZ-100 nanoPartica Dynamic Light Scattering (DLS) system, using a 532 nm laser with a fixed 90º scattering angle at 25 ºC. Every sample was prepared using filtered Mili-Q water (10 mL Luer Solo sterile syringes, B. Braun Melsungen AG with 0.45 µm porosity HT Tuffryn® membrane filters, Sigma). 600 µL of each sample were transferred using sterile syringes (1 mL Luer Solo sterile syringes, B. Braun Melsungen AG) to a disposable sizing cuvette. Using the Horiba software package, the autocorrelation curves were analysed using both cumulants analysis (Z-average and polydispersity) and determination of size distributions. The size distribution analysis was specified as a monodispersed sample monodispersivity with a standard distribution form. Both temperature and water's viscosity (η=0.893 mPa.s) were used as inputs $Dh = kBT 3\pi\eta Dt$, **Equation 1.1.** (see $Dh = kBT 3\pi\eta Dt$, **Equation 1.1.**). The results shown are representative of at least three measurements for each sample showing satisfactory autocorrelation curves, and represented as scattering light intensity, volume and number when adequate.

3.7. Plasma proteins SDS-PAGE assay

Sample buffer (5 μL) was added to 15 μL of HSA, BSA, HT, BPF and two human plasma samples (provided by IMM and MG). Low range molecular weight (LMW) standards sample was prepared adding 2 μL of distilled water to 2 μL of sample buffer and 2 μL of SDS-PAGE low range molecular weight standards (BioRad, Cat. no. 16500-500). All samples were then denatured for 4 min in boiling water, after which the samples were loaded in a 10-well 10% resolving acrylamide and 5% stacking acrylamide gel, ran using a Bio Rad Mini-PROTEAN Tetra Cell system at 180 V, 50 mA for 45 min. The resulting gel was stained for 1 h minimum with 0.5% Coomassie blue solution, and left in destaining solution for 8 h minimum, kept in a 1:1 destaining and water solution. This protocol was repeated until meaningful results were obtained.

3.8. Bicinchoninic acid (BCA) assay for total protein concentration of human plasma

Total protein concentration in human plasma was determined by the bincichoninic acid method [55]. Six standard BSA (Sigma, Micro-standard 1 mg/mL liquid solution) solutions of increasing concentrations were added to 1 mL solution of 100:2 bicinchoninic acid (Sigma) to copper (II) sulphate (Sigma, 4% (w/v) solution, prepared from Cu (II) sulphate penta-hydrated) and the absorbance at 562 nm was measured using a VARIAN Cary 50 Bio spectrophotometer. The absorbance at 562 nm of human plasma samples (kindly provided by IMM and MG) of increasing concentrations in 1 mL of 100:2 BCA:$CuSO_4$ was then measured in triplicate, and total protein concentration was determined from a calibration curve using BSA as standard.

3.9. Human and bovine fibrinogen homology analysis

Within the NCBI BLAST [56] online server, a protein blast search was conducted using the blastp algorithm, fasta sequences of bovine serum fibrinogen (PDB 1DEQ) and human serum fibrinogen (PDB 3GHG) with BLOSUM62 [57] as the scoring matrix. A search for conserved domains in the two proteins was conducted using the RPS-BLAST [58] search tool.

3.10. Protein-ligand docking

3.10.1. Docking transferrin-CALNN and transferrin-NNN

The ligands secondary structures were predicted (> 89% probability for CALNN, > 96% for NNN) using NetSurfP [59] online server, and its torsion angles (ϕ=-51º, ψ=153º, Ω=180º) were later on used for predicting their 3D coordinates using VEGA [60] within the ProBuilder [61] online tool. Transferrin's biological unit pdb file was obtained from the RCSB PDB website (PDB 3V83). Using AutoDockTools (ADT) [62] the solvent molecules were removed by default and polar hydrogens were added to the macromolecule. The pdbqt files for the protein and the ligands were obtained with ADT. The search space parameters were defined as the integral biological unit of transferrin and the macromolecule grid was constructed using ADT. The amine bonds in CALNN and NNN were considered rigid and all the remaining bonds were assumed as flexible.

The docking assay was performed using AutoDock Vina [63] (with exhaustiveness parameter=4), producing nine CALNN modes and nine NNN modes.

3.10.2. Docking HSA-CALNN and HT-CALNN

HSA and HT (PDB 1E7I and 3V83, respectively) preparation and ligand atomic coordinates were produced as previously described. Using AutoDock Vina, ten runs were performed with exhaustiveness=1, num modes=10 and energy_range=10, resulting in 1000 modes of CALNN peptide for each protein. The 100 most energetically favourable modes were represented for each protein docked, and were colored by their temperature factor (b-factor).

3.11. Molecular visualizations

All molecular visualizations were produced using the UCSF Chimera 1.10.1 software package [64]. Protein representations are obtained by 90 º rotations of each structure, representative of a biological protein unit in a cubic unit cell.

3.12. Estimation of protein number around a nanoparticle

The diameter of each plasma protein and CALNN was measured using the 'distance' command of the UCSF Chimera 1.10.1 package [64]. The surface area of each plasma protein was estimated using the Open Chemera Library pdbtools utility tool (source code available at https://github.com/lkrippahl/Open-Chemera). Estimation of the protein number around a theoretical 20 nm nanoparticle was made assuming a face-centered cubic unit cell packing of each protein [53,65].

3.13. Digital images processing

The analysis of all agarose gels was done using eReuss, a gel analysis application currently under development and freely available at https://github.com/lkrippahl/eReuss. The migration distances for each concentration ratio were computed from the digital image of each electrophoresis gel by fitting Gaussian curves to the image intensity profiles averaged for each lane.

Blank page

4. Results and discussion

4.1. Whole plasma protein content

In order to determine which blood plasma proteins are most likely to become part of a nanoparticle protein corona, identification and quantification of protein content in two whole plasma samples was performed by means of denaturing electrophoresis and the Bicinchoninic acid method, respectively. Total protein concentration of two human plasma samples resulted in 9.43 mg/mL for sample MG, and 23.7 mg/mL for sample IMM (**Supplementary data**, **Table I.3**), using 1 mg/mL BSA as standard (**Supplementary data**, **Figure I.1**). The values obtained for total protein content of the plasma samples were under the reference range of *circa* 94 g/L [18]. The two plasma samples were taken from healthy subjects (IMM and MG) and are representative of average protein composition in human blood plasma. The 24 g/L IMM sample was previously submitted to an albumin removal method that could have decreased the initial protein content. The MG sample was obtained from a whole blood sample, whose preservation and/or fractionation methods might not have removed the proteolytic enzymes. This can have caused sample degradation [66] and therefore can justify the low 9 g/L total plasma concentration. **Figure 4.1** shows a denaturing polyacrylamide gel electrophoresis of two plasma samples and the most abundant blood plasma proteins.

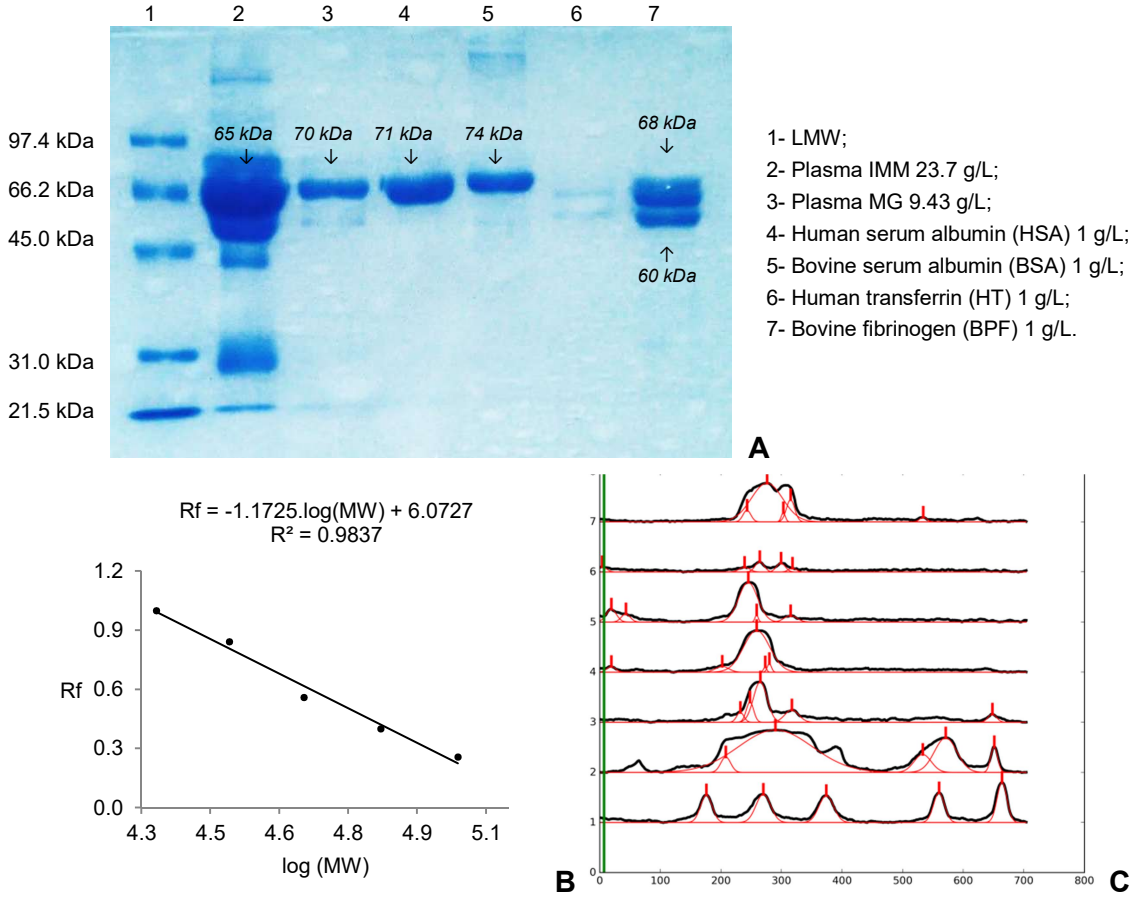

Figure 4.1. 10 % resolving SDS-PAGE of plasma samples and pure proteins (**A**), low range molecular weight calibration curve (**B**), and computed migrated distances (**C**).

From the SDS-PAGE in **Figure 4.1**, it becomes obvious that the purified proteins used throughout this work are part of the human plasma proteome. Human serum albumin (lane 4) is a main component of blood plasma (lanes 2 and 3), as the three samples show the same relative migration representative of albumin standard (lane 1). Bovine albumin (lane 5) displays a similar migration to the human albumin samples, with a determined molecular mass of 74 kDa.

Human transferrin sample in lane 6 shows two dim bands showing the same molecular weights of fibrinogen in lane 7. As the estimated molecular weight for this protein is around 80 kDa, and no bands are visible for this molecular weight, this could be a result of fibrinogen lane overflow. There is no information obtained from this SDS-PAGE on the molecular weight or monomeric structure of denatured human transferrin.

In lane 7 we can observe two fragments of the fibrinogen molecule, weighting 60 and 68 kDa. The intense higher molecular weight band agrees with the presence of two pairs of superimposed monomers. As fibrinogen is composed of two monomers of each polypeptide chain, the presence of four 68 kDa monomers and two 60 kDa monomers make up its 340 kDa molecular weight.

4.2. Homology analysis of human and bovine fibrinogen

Sequence and structural homology assays were performed to determine the similarity between human and bovine fibrinogen, in order to validate the latter protein in the context of this work. **Figure I.2** in **Supplementary data** shows the sequence alignment for human and bovine fibrinogen, and the results are summarized below.

Table 4.1. Summarized results of the sequence alignment of bovine with human fibrinogen.

Chain	Query cover	Sequence identity	Score	E-value
α	98 %	60 %	460	6E-163
α’	38 %	15 %	19	4E0
β	38 %	15 %	19	4E0
β’	12 %	27 %	37	1E-5
γ	98 %	60 %	460	6E-163
γ’	12 %	27 %	37	1E-5

Amino acid sequences of human and bovine fibrinogen from blood plasma were aligned to investigate the degree of similarity between the two proteins. **Table 4.1** shows that sequence similarities for polypeptide chains α and γ of human fibrinogen are 60 %, making them homologue with bovine fibrinogen. A lower homology of 27 % is observed in polypeptide chains β’ and γ’; and for chains β and α’ there is no homology observed due to low similarity of 15 % between bovine and human amino acid sequences. These results mean that α and β’ polypeptide chains, as well as the γγ’ chain pair of fibrinogen from bovine are homologue to the same amino acid sequences in human fibrinogen, and the two sequences probably have the

same structure and function in the plasma because they share the same common ancestor [67]. A search for conserved structural domains in the two proteins was done in order to test this hypothesis, whose results are shown in **Table 4.2** and **Table 4.3**.

Table 4.2. Summarized results of the search for conserved domains in bovine fibrinogen (PDB 1DEQ).

Chain	Structural domain family	Location (aa)	Score	E-value
α	Fib_alpha	31-168	207	7E-65
	Fibrinogen_aC	426-490	98	3E-25
α'	Fib_alpha	31-168	207	7E-65
	Fibrinogen_aC	426-490	98	3E-25
β	Fib_alpha	62-204	210	1E-66
	FreD	207-456	337	2E-115
β'	FreD	207-456	337	2E-115
	Fib_alpha	62-204	209	1E-66
γ	Fib_alpha	5-146	214	2E-69
	FreD	149-388	346	1E-119
γ'	Fib_alpha	5-146	214	2E-69
	FreD	149-388	346	1E-119

The most noticeable structural domains observed in bovine fibrinogen fall in the Fib_alpha superfamily, whose structural motifs are located in the coiled coil region of the three intertwined pairs of polypeptide α, β and γ chains. The Fibrinogen_aC domain contains the C-terminal of the α chain of mammal fibrinogen, as observed in the αα' structural domain structures. The FReD superfamily designation stands for 'fibrinogen-related domains', which includes the C and N-gobular termini of the beta and gamma polypeptide chains.

Table 4.3. Summarized results of the search for conserved domains in human fibrinogen (PDB 3GHG).

Chain	Structural domain family	Location (aa)	Score	E-value
α	Fib_alpha	34-173	200	4E-64
α'	Fib_alpha	34-173	200	4E-64
β	Fib_alpha	9-151	204	3E-65
	FreD	154-389	325	1E-111
β'	Fib_alpha	9-151	203	3E-65
	FreD	154-404	325	1E-111
γ	Fib_alpha	5-146	212	1E-68
	Fibrinogen_C	149-389	357	3E-124
γ'	Fib_alpha	5-146	212	1E-68
	Fibrinogen_C	149-389	357	3E-124

Similar conserved structural domains in human and bovine fibrinogen are observed (**Table 4.2** and **Table 4.3**). With this results, a highly identical amino acid sequence and structural domains are present in human and bovine fibrinogen; being that results obtained for bovine fibrinogen can be extrapolated to human fibrinogen due to their high similarity.

4.3. Gold nanoparticle synthesis, concentration determination and functionalization

The various steps of the citrate reduction method for nanoparticle synthesis were monitored by change in color during reaction (**Figure 4.2**). Gold (III) chloride solution is a yellow-colored solution that - by addition of citrate - turns transparent, after which black-colored gold nanoclusters and small nanoparticles begin to form. At the end of the synthesis, the solution shows a wine-red color, typical of a colloidal suspension of spherical nanoparticles with an average diameter of 15 nanometres.

Figure 4.2. Following the steps during nanoparticle synthesis. **A**- Gold (III) chloride yellow solution; **B**- reduced by citrate, **C**- formation of black-colored gold nanowires, and **D**- the resulting red monodispersed colloidal nanoparticles.

Following AuNP synthesis and concentration determination, their functionalization with CALNN was performed. The UV absorbance spectra of the nanoparticles before and after functionalization are shown in **Figure 4.3**. A four nanometer deviation in the SPR band is observed from 520.0 nm in synthetized gold nanoparticles to 523.9 nm in CALNN-functionalized nanoparticles.

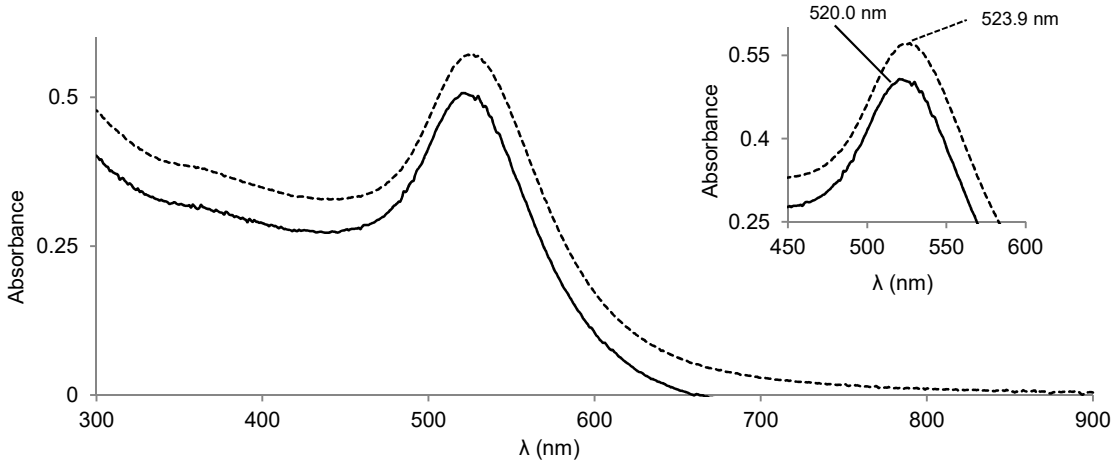

Figure 4.3. UV-visible 900-300 nm absorbance spectra of AuNP (full line) and AuNP-CALNN (dotted line). Insert shows the absorbance maximum wavelenght for each spectrum.

Haiss and colleagues established a correlation between a nanoparticle's diameter and the molar extinction coefficient (ε_{450nm}) of the colloidal solution [54]. For nanoparticles from 5 to 100

nanometers in diameter, the determination of their diameter is made by substituting the nanoparticle's SPR absorbance value and the absorbance at 450 nm in $\frac{Abs_{(SPR)}}{Abs_{(450\ nm)}} = 0.3350\ ln\ \phi + 0.7301,$ **Equation 4.1**. The correspondent ε_{450nm} value (Supplementary data, Table I.2) of the nanoparticles can be used in the Lambert-Beer law to determine the final nanoparticle concentration.

$$\frac{Abs_{(SPR)}}{Abs_{(450\ nm)}} = 0.3350\ ln\ \phi + 0.7301, \qquad \textbf{Equation 4.1}$$

where ϕ represents the nanoparticle's diameter (nm).

An intense absorbance peak at 520.0 nm is present due to the SPR phenomenon of conducting gold valence electrons. A slight bathochromic shift upon functionalization is a result of increase in nanoparticle diameter due to covalent binding of CALNN to the AuNP surface. The surface plasmon resonance effect is maintained by nanoparticles; however this small size increment produces resonance at a lower frequency detected by UV-Vis spectroscopy.

The maximum absorbance peak, together with change in solution color, can be an indicator of nanoparticle stability. The collective electronic oscillations of aggregated nanoparticles resonate with lower energy radiation, and its absorbance is detected in the red spectrum region showing the complementary blue color. In this case, a solution of spherical 15 nm nanoparticles shows a bluish color (**Figure 4.4 A**) and lower frequency maximum absorbance.

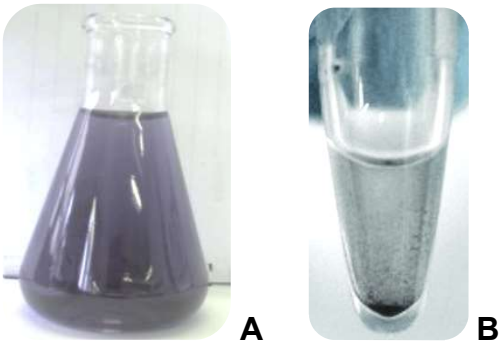

Figure 4.4. Nanoparticle aggregates with deviated SPR band (**A**), and extensive nanoparticle aggregation with no SPR effect (**B**).

In the case of black precipitated aggregates on a transparent solution, the SPR effect is no longer occurring and an extended aggregation is observed (**Figure 4.4 B**) providing information on nanoparticle stability over time and under different conditions, such as varying pH values, ionic strength, .

4.4. Prediction of the number of plasma proteins adsorbed to AuNP-CALNN

In order to define a starting point on a mechanistic model of protein adsorption to a nanoparticle, silhouette areas of five plasma proteins have been calculated, and are shown in

Table 4.4. In parallel, diameters of human proteins were determined as shown in **Figure 4.5** and **Figure 4.6**. These properties can give information on the expected number of proteins necessary to achieve full nanoparticle coverage, and help to the design of additional experiments.

Table 4.4. Estimated silhouette areas of plasma proteins.

Plasma protein	Silhouette area (Å^2), solvated protein				Silhouette area (Å^2), without solvation waters			
	Average	Median	Maximum	Minimum	Average	Median	Maximum	Minimum
HSA	3785	3725	4672	3071	3785	3724	4672	3071
BSA	3837	3804	4544	3087	3837	3804	4544	3087
HT	4009	4014	4801	2778	3827	3819	4614	2622
BPF	--	--	--	--	10929	11680	12999	3602
HPF	--	--	--	--	13186	14159	15734	4363

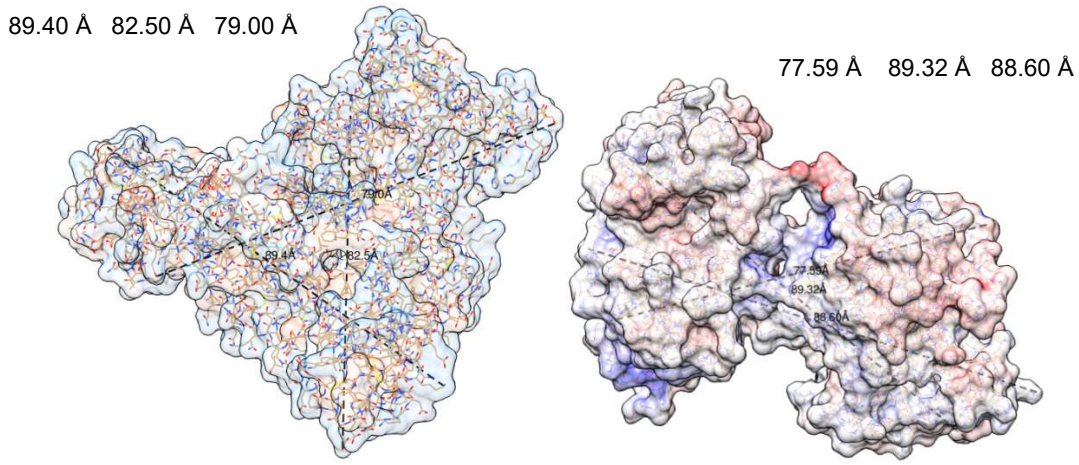

Figure 4.5. Left: Diameter of human serum albumin (PDB 1E7I). Right: Diameter of human transferrin (PDB 3V83).

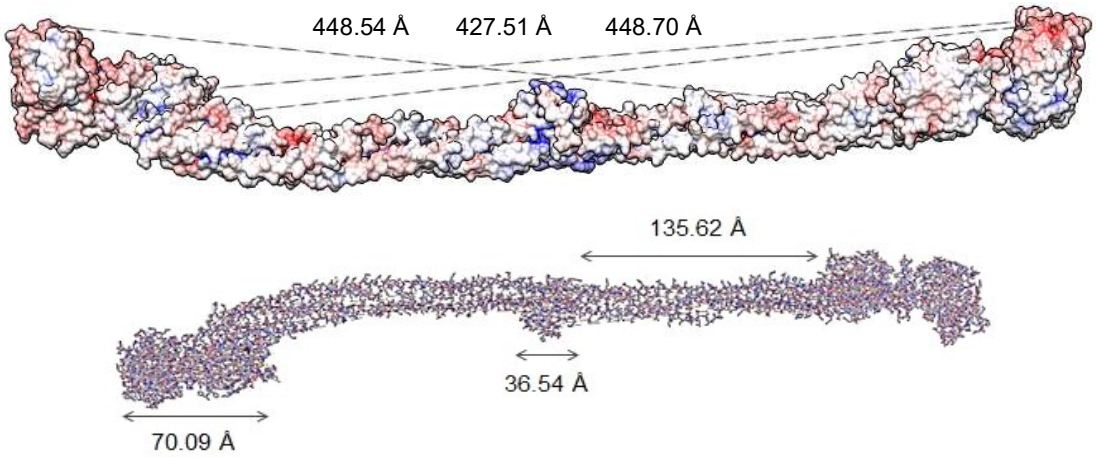

Figure 4.6. Top: End-to-end diameter of human fibrinogen. Bottom: Average diameter of the terminal nodules, central region and linking polypeptide chain of human fibrinogen. (PDB 3GHG).

By predicting the size of each plasma protein, it is possible to estimate the amount of proteins adsorbed to a 20 nm nanosphere. These intermediate assumptions can be used to establish a model for protein adsorption to nanoparticle upon arrival at the bloodstream.

The silhouette area of human albumin is in average 3785 Å^2, and its average diameter is 83.6 Å. Assuming a face-centered cubic unit cell packing, meaning full nanoparticle coverage, and applying it to $r_w = \sqrt[3]{\frac{3V_w}{4\pi}}$, **Equation 1.7** it is estimated that eighteen similar HSA proteins can adsorb to a 20 nm spherical nanoparticle.

The same process can be applied to human transferrin, with a silhouette area of 3827 Å^2 and an average diameter of 85.2 Å, resulting in a nanoparticle covered with seventeen transferrin proteins. As both proteins exhibit globular shape; one can assume that these molecules have no global orientation preference when adsorbing to a nanoparticle, and their hypothetical binding sites are roughly spread out across the entire protein surface (**Figure 4.7**).

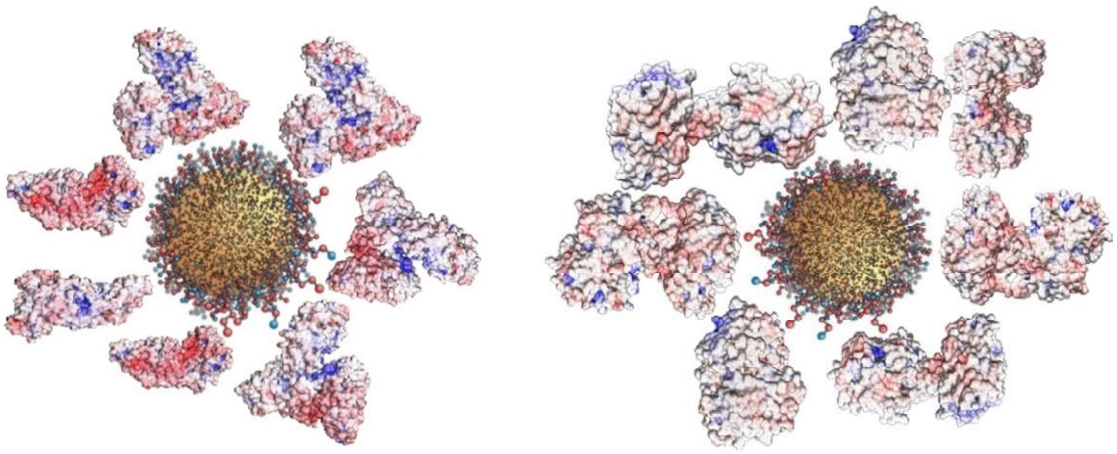

Figure 4.7. Schematic representation of nanoparticles' albumin (left) and transferrin (right) coronas (not drawn to scale). *Nanoparticle model adapted from* [48].

Fibrinogen's adsorption to nanoparticles shows a different adsorption configuration, owing to its thread-like shape. End-to-end measurements (**Figure 4.6**) show an average diameter of 441.6 Å, with a silhouette area of 13186 Å^2. The diameter of the central region is 36.54 Å, and the terminal nodules show 70.09 Å in diameter, with 15425.6 Å^2 of surface area [25] (**Figure 4.6**). Assuming an end-on adsorption orientation carried out by one of the terminal nodules, there would be about twenty-nine fibrinogen molecules around a 20 nm nanoparticle (**Figure 4.8**).

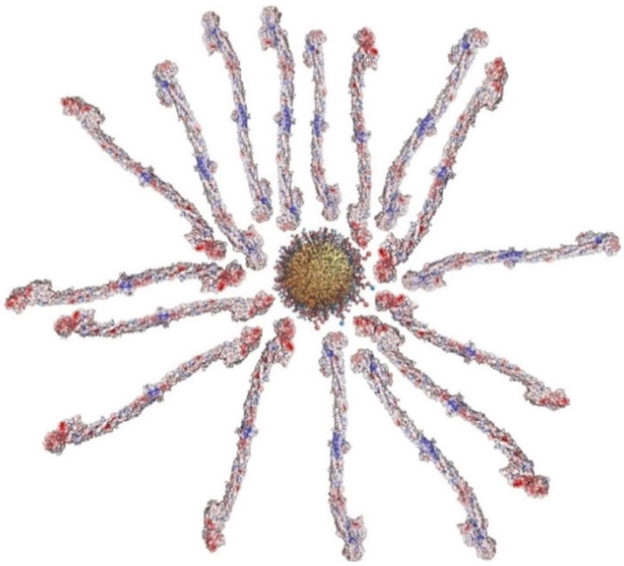

Figure 4.8. Schematics of fibrinogen adsorbed to a nanoparticle (not drawn to scale). *Nanoparticle model adapted from* [48].

4.5. Electrostatic potential surfaces of plasma proteins

Accessing the surface potential of plasma proteins is a tool for finding possible interaction sites with nanoparticles. **Figure 4.9** shows the electrostatic potential surface of human serum albumin at pH 7.4 (also in **Supplementary data**, **Figure I.5**).

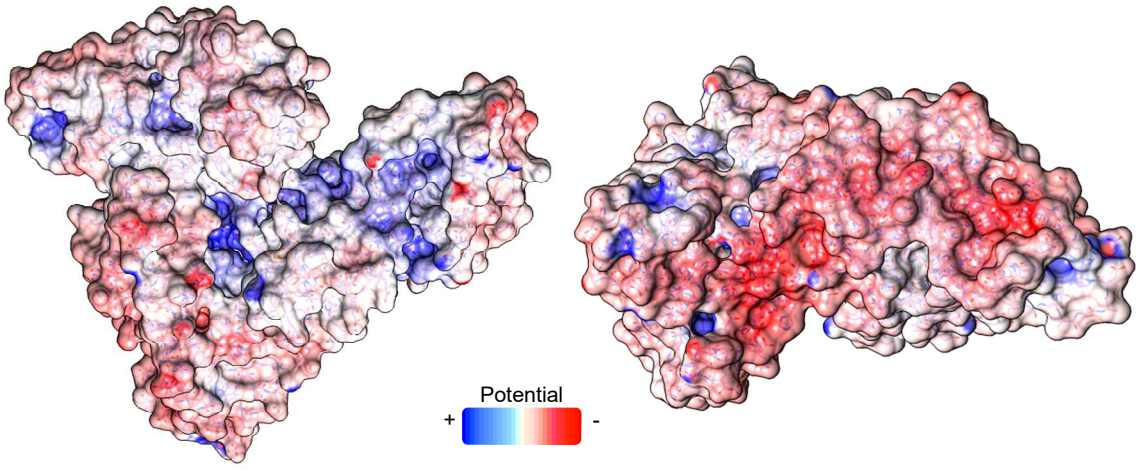

A. Back-view **B**. Bottom-view

Figure 4.9. Electrostatic potential surface of human serum albumin at pH 7.4.

Human albumin shows three hydrophobic pockets for ligand binding. These regions exhibit at their surface positive electrostatic potential at physiological conditions (**Figure 4.9 A,**), and the pocket environment is hydrophobic. The protein shows overall negative surface charge, whose intensity is stronger at the bottom of the protein (**Figure 4.9 B**). The surface charge distribution in albumin suggests that this protein could interact with the alanine and leucine CALNN residues by hydrophobic interactions in its ligand pockets.

Human transferrin's electrostatic potential surface (**Figure 4.10**) displays an even charge distribution spreading throughout the tertiary structure (**Supplementary data**, **Figure I.7**). The region that interacts with its membrane receptor shows negative potential values (**Figure 4.10 A**), and the opposite protein side displays positive potential values (**Figure 4.10 B**), showing higher intensities at the upper side of its right lobe.

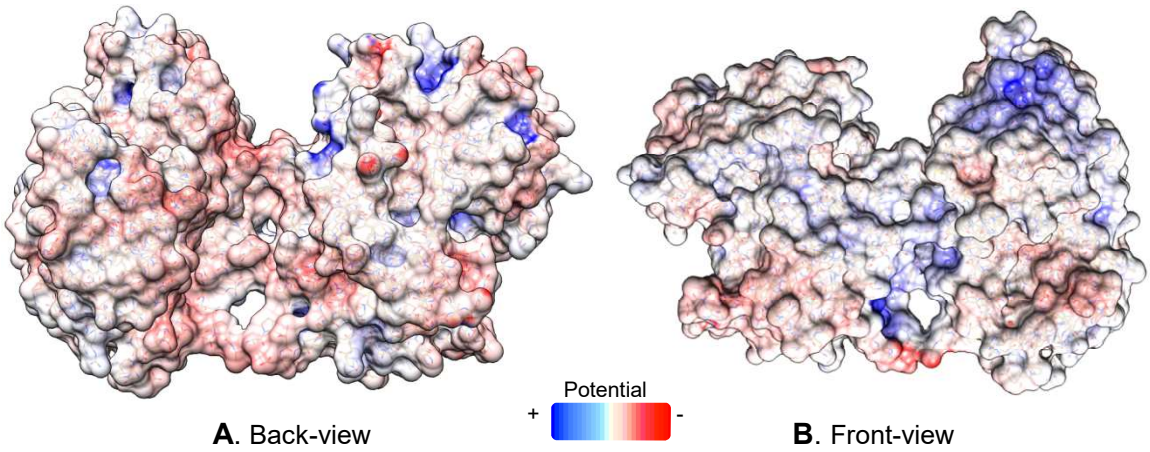

Figure 4.10. Electrostatic potential surface of human transferrin at pH 7.4.

In **Figure 4.10 B**, a high intensity of positive potential values is also visible at the top-right side of transferrin. This could indicate a possible interaction area for negatively-charged residues like the carboxylic end of CALNN peptide. This result could be a starting point to access the interaction site of transferrin with CALNN-functionalized nanoparticles; if transferrin has a localized positive charge at its surface, its adsorption to negatively-charged nanoparticles could be processed by van der Waals interactions of close opposite-charged residues.

Fibrinogen displays a more complex potential distribution on its surface (**Figure 4.11**, and **Figure I.8** in **Supplementary data**). The three pairs of intertwined chains (**Figure 4.11 D**) show residues with both positive and negative charge, giving this structure overall neutral charge. Terminal nodules display positive global charge (**Figure 4.11 B** and **C**) while the central region of fibrinogen is predominantly negative (**Figure 4.11 A**).

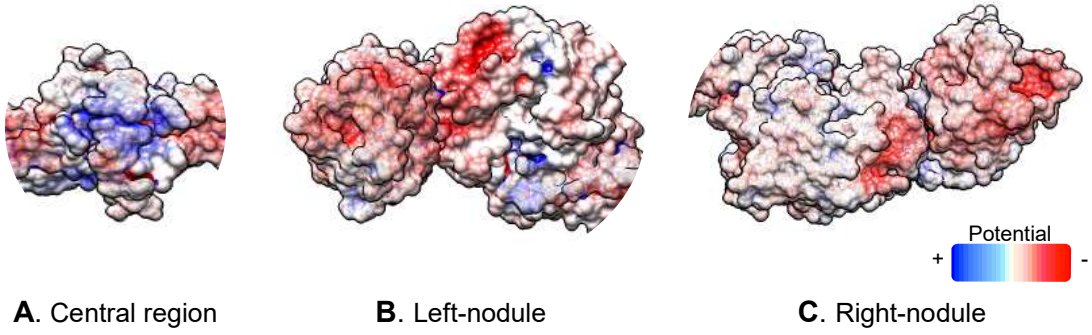

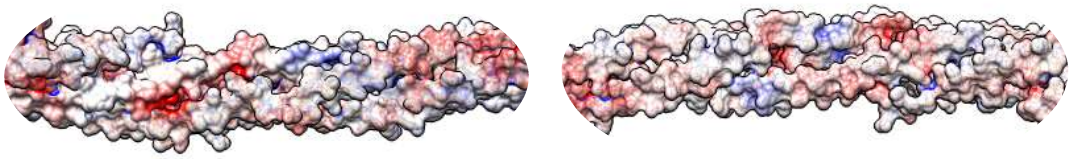

D. Chains

Figure 4.11. Electrostatic potential surface of human fibrinogen at pH 7.4.

This fibrillary shape and localized intense surface charges can originate a couple of hypotheses on the way fibrinogen can interact with nanoparticles: (1) via its central region, by electrostatic interactions between positive charged protein residues and negatively-charged CALNN residues; and (2) by its terminal nodules, through van der Waals bonds between adjacent nuclei.

The first requires that adsorption is made assuming a side-on orientation preference, leaving out the linking chains and nodular termini to interact with the negatively-charged nanoparticle surface, which could promote conformational changes to the protein structure. Interaction through the terminal nodules could be promoted by an end-on adsorption orientation, in which fibrinogen proteins would spread out from the nanoparticle surface (**Figure 4.8**).

Using these computational results, electrophoretic mobility assays were produced for bionanoconjugates of three plasma proteins with increasing concentration ratios in order to obtain experimental data regarding formation of protein corona, binding and dissociation constants and nanoparticle surface saturation with plasma proteins.

4.6. Human albumin bionanoconjugates adsorption behaviour over time

Incubation time is crucial for the formation of protein corona on nanoparticles [14]. The main focus of this assay was to examine the influence of protein incubation time on the HSA adsorption to nanoparticles. The digital images of 1 h, 3 h, 7 h, and 24 h incubation assays for increasing [HSA]:[AuNP-CALNN] ratios are shown in **Figure 4.12**.

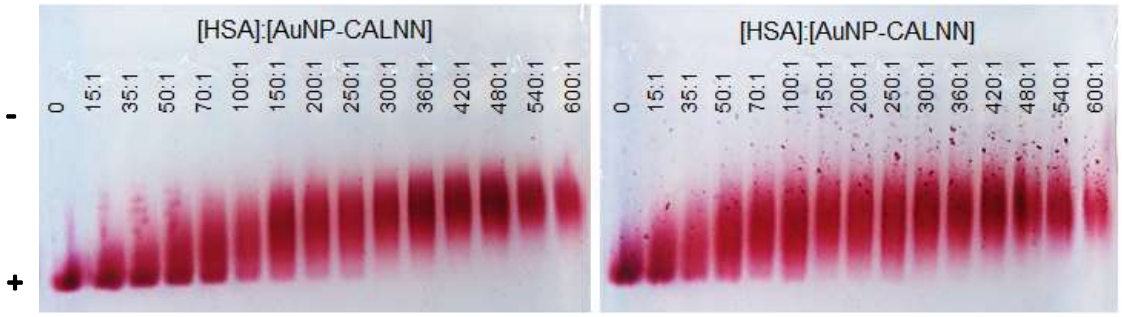

A **B**

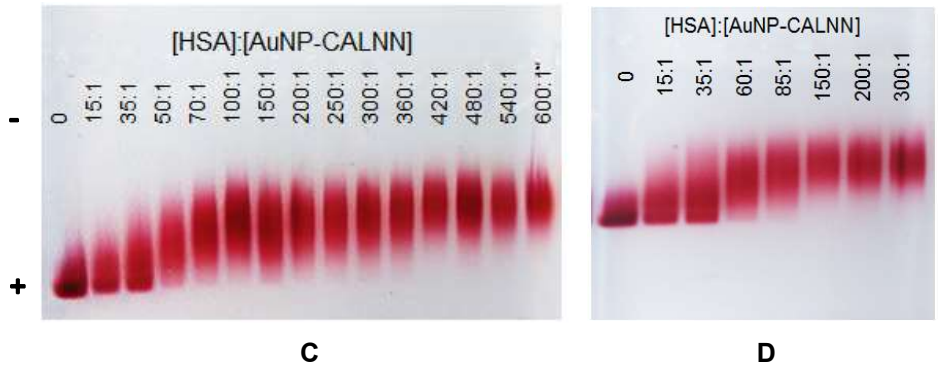

C **D**

Figure 4.12. Agarose gel digital images of 1 h (**A**), 3 h (**B**), 7 h (**C**), and 24 h (**D**) incubation assays with increasing [HSA]:[AuNP-CALNN] ratios.

Several authors have already studied the dynamics of protein adsorption to nanoparticles and the formation of the protein corona (see ***1.1. Protein corona***). This process is governed by the Vroman effect, which relies on the protein's thermodynamic and kinetic behaviours. Studying the formation protein corona composed of only one type of protein allows the determination of variances in affinity constants and assessment of protein-protein interactions during the formation of the protein corona around nanoparticles. **Figure 4.12** shows the evolution of human serum albumin corona adsorption to nanoparticles over time.

Figure 4.12 A and **B** represent shorter incubation times of protein corona formation. Human albumin adsorption to nanoparticles starts by creating diffuse bionanoconjugates bands, result of nanoparticles coated with distinct albumin quantities. These bionanoconjugates seem to have the most varying protein content, which reflects on their molecular weight and surface charge; and finally on their electrophoretic mobility. The initial formation of albumin corona appears to be a dynamic process in which albumin proteins start interacting with the nanoparticle surface, forming uneven protein coronas with varying protein content and molecular weights.

Figure 4.12 C represents an overnight (7 h) incubation of HSA with gold nanoparticles. Overall the compactness of the bionanoconjugates bands seems to have improved with increase of incubation time. This can account for the fact that establishment of stronger interactions between albumin and the nanoparticle surface could be a slow process only achieved in this time interval. Tighter bionanoconjugates bands also explain the formation of more uniform protein corona, showing less variable molecular weights which in consequence exhibit a more even migration in the agarose gel.

After twenty four hours incubation, albumin corona around nanoparticles are well formed, which is visible in **Figure 4.12 D**. The bands have become even more compact then in the 7 h assay, and any noticeable smear is explained by protein dissociation equilibrium from nanoparticle surface to bulk solvent and *vice versa*.

For practicality reasons and with these results in mind, further electrophoretic assays were performed to predict the concentration ratios necessary to produce a full protein corona on nanoparticles, using 7 h incubation time for all the plasma proteins and whole plasma bionanoconjugates.

4.7. Electrophoretic mobility of AuNP-CALNN bionanoconjugates

The digital image of an agarose gel of AuNP-CALNN bionanoconjugates of human serum albumin produced with increasing protein concentration is displayed in **Figure 4.13 A**, with the objective of determine the concentration ratio where a protein corona is formed around nanoparticles. The compact red band of nanoparticles alone in lane 1 is an indicator of the homogeneity present in the functionalized nanoparticle sample. Its migration distance and band shape also confirm successful nanoparticle functionalization, due to consistently even binding of CALNN capping agent to all nanoparticles. This creates uniform functionalized nanoparticles which migrate similarly in the agarose gel.

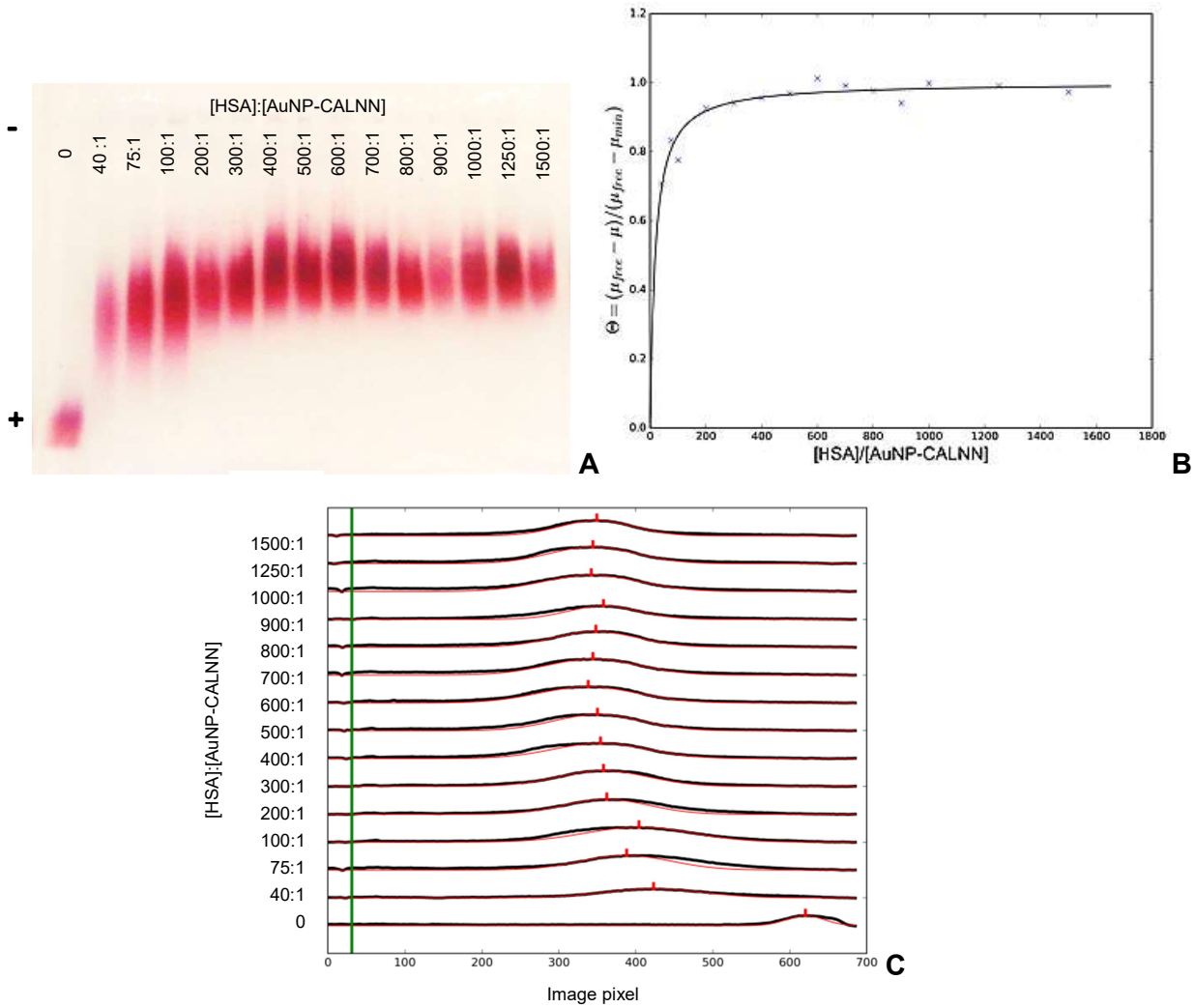

Figure 4.13. Electrophoretic mobility assay of HSA:AuNP-CALNN bionanoconjugates (**A**), Langmuir isotherm plot (**B**), and computed migration distances (**C**).

Conjugation promotes increase in molecular weight and decrease in the surface charge of the bionanoconjugates, resulting in decreased mobility when comparing to unconjugated AuNPs. Protein to nanoparticle ratios ([HSA]:[AuNP-CALNN]) used in this assay ranged from 0 to 1500, and show full nanoparticle coverage starting at 400:1 protein to nanoparticle ratio is confirmed by the plateau of electrophoretic mobility of **Figure 4.13 C**.

Fitting a Langmuir isotherm to the electrophoretic mobility values for bionanoconjugates allows the determination of the binding constant for albumin to nanoparticles (K_{eq} = 5.56E-2 ± 1.18E-2 M^{-1}). In addition, Hill equation fitting of the data enabled the prediction of dissociation constant of K_{eq} = 2.05E0 ± 2.72E0 M^{-1}; the Hill cooperativity coefficient was disregarded owing to its negative value (n = -2.54).

By decreasing the [HSA]:[AuNP-CALNN] ratios, resolution of mobility distances was assumed to improve. The assay for protein:nanoparticle ratios from 0 to 400 presented in

Figure 4.17 A reveals formation of a plateau for albumin bionanoconjugates starting already at a 200:1 ratio, also supported by the Langmuir isotherm in **Figure 4.14 B**.

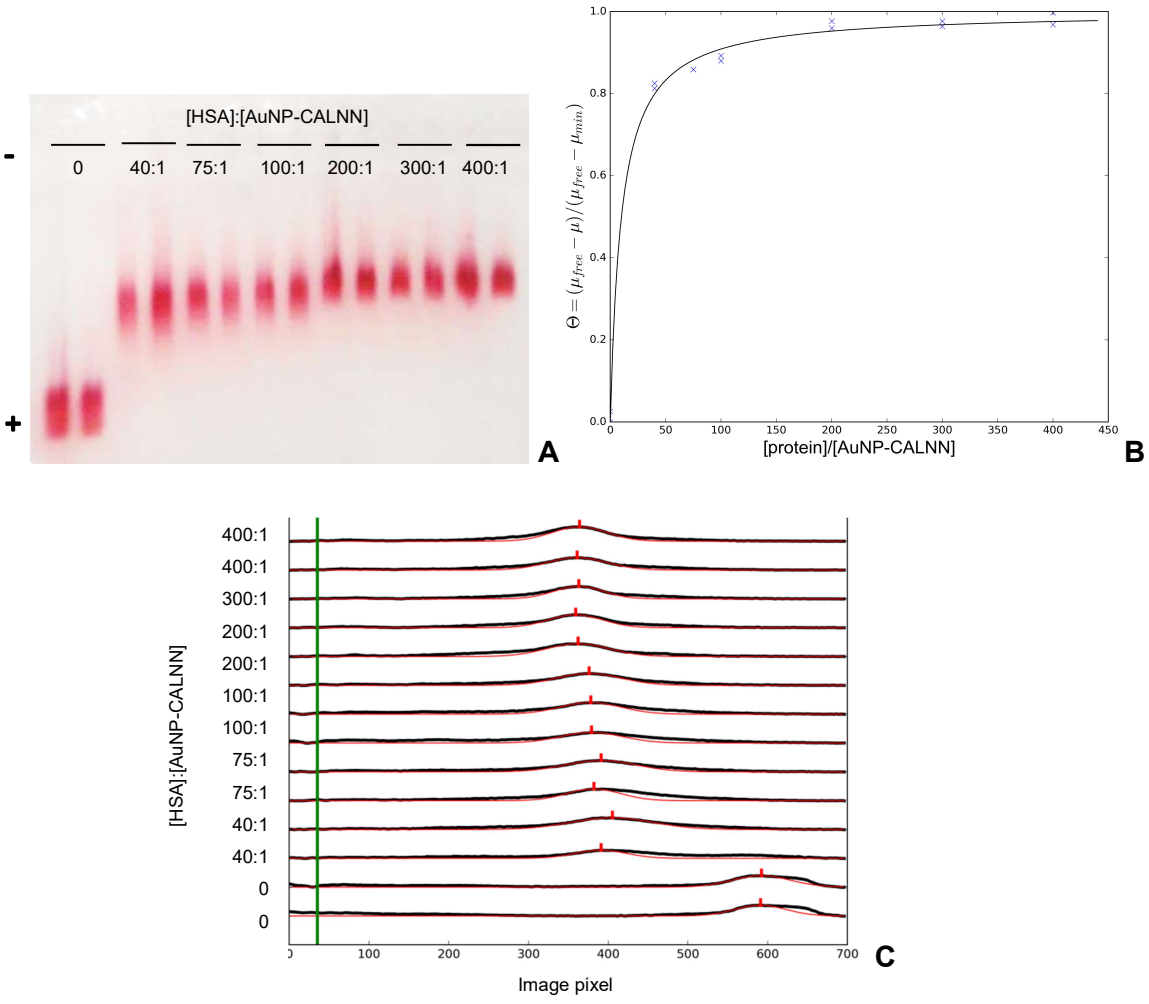

Figure 4.14. Electrophoretic mobility assay of HSA:AuNP-CALNN bionanoconjugates (**A**), Langmuir isotherm plot (**B**) and computed migration distances (**C**).

Functionalization produced compact bands observed in the first two lanes in **Figure 4.14 A**. Smear in bionanoconjugates with 40:1 up to 100:1 ratios can be explained by the formation of bionanoconjugates with varying protein content, which migrate differently in the agarose support. The binding constant for albumin was derived from the fitting in **Figure 4.14 B** and resulted in K_{eq} = 9.92E-2 ± 2.07E-2 M^{-1}. Hill cooperativity coefficient was determined by fitting Hill's equation to the electrophoretic mobility data, n =0.138. The dissociation constant was also derived from Hill's equation K_d = 3.05E0 ± 4.99E-4 M^{-1}; as well as the Hill coefficient n = 0.299.

The value for the dissociation constant K_d, together with the low Hill coefficient obtained for the formation of albumin corona seem to reflect the influence of protein-protein uncooperative interactions at the nanoparticle surface. The value for equilibrium of albumin at the nanoparticle surface seems to show a slow exchange time between free and bound protein. The albumin:nanoparticle ratios appear to be not high enough to promote nanoparticle saturation producing full albumin corona, due to repulsive crowding effect of albumin proteins on the nanoparticle surface.

The digital image of AuNP-CALNN bionanoconjugates of human serum albumin are displayed in **Figure 4.15**. The purpose of this assay was to observe the migration behaviour of even smaller concentration ratios of albumin to nanoparticle, close to those estimated for a monolayer corona. In fact these concentration ratios are not related to the number of proteins forming a monolayer corona; nevertheless the low concentrations ratios were used in this assay.

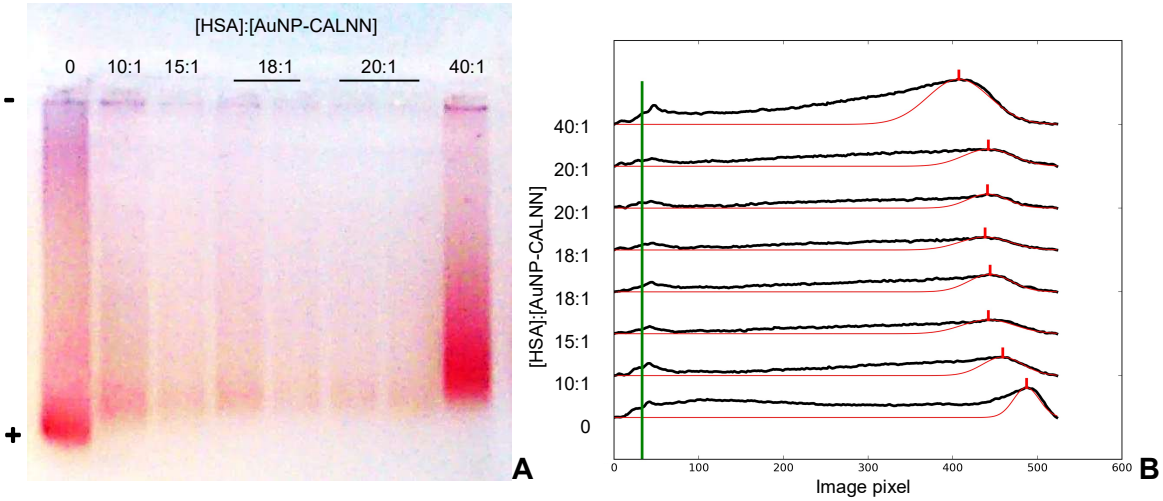

Figure 4.15. Electrophoretic mobility assay of HSA:AuNP-CALNN bionanoconjugates (**A**), and computed migration distances (**B**).

The visible smear prevalent across all samples can be justified by the following phenomena: (1) protein dissociation from bionanoconjugate, (2) inefficient nanoparticle functionalization, and (3) nanoparticle aggregation. Loss in protein content is also confirmed by the pale red color in samples with concentration ratios from 10:1-20:1. Widespread nanoparticle aggregation can

cause unsuccessful interaction with CALNN molecules and/or albumin. Even so a decrease in mobility is observed between bionanoconjugates lower protein:nanoparticle concentration ratios. Again, no plateau was established with the highest ratio being 40:1. Protein to nanoparticle ratios do not give information on the amount of protein at the nanoparticle surface, they provide information of the proportionality between species in solution; in fact these ratios are not high enough to produce a protein corona because no migration plateau was achieved. In order to determine protein concentration (not number) required to produce a protein corona around nanoparticles, binding constants should be determined from fitting Langmuir isotherm plot to electrophoretic mobility data. As no plateau is observed for these protein to nanoparticle concentration ratios, the data obtained from Langmuir and Hill equations fitting cannot be considered because there was no established equilibrium between free and adsorbed proteins.

The second most abundant blood protein is fibrinogen. The digital images of AuNP-CALNN bionanoconjugates of bovine plasma fibrinogen (BPF) are displayed in **Figure 4.16 A**. As before, functionalization was assessed by the shape and migration of the unbound nanoparticle band, displaying the highest migration distance. Complete fibrinogen corona on nanoparticles is visible starting at 600:1 [fibrinogen]:[AuNP-CALNN] ratio (**Figure 4.16 A**).

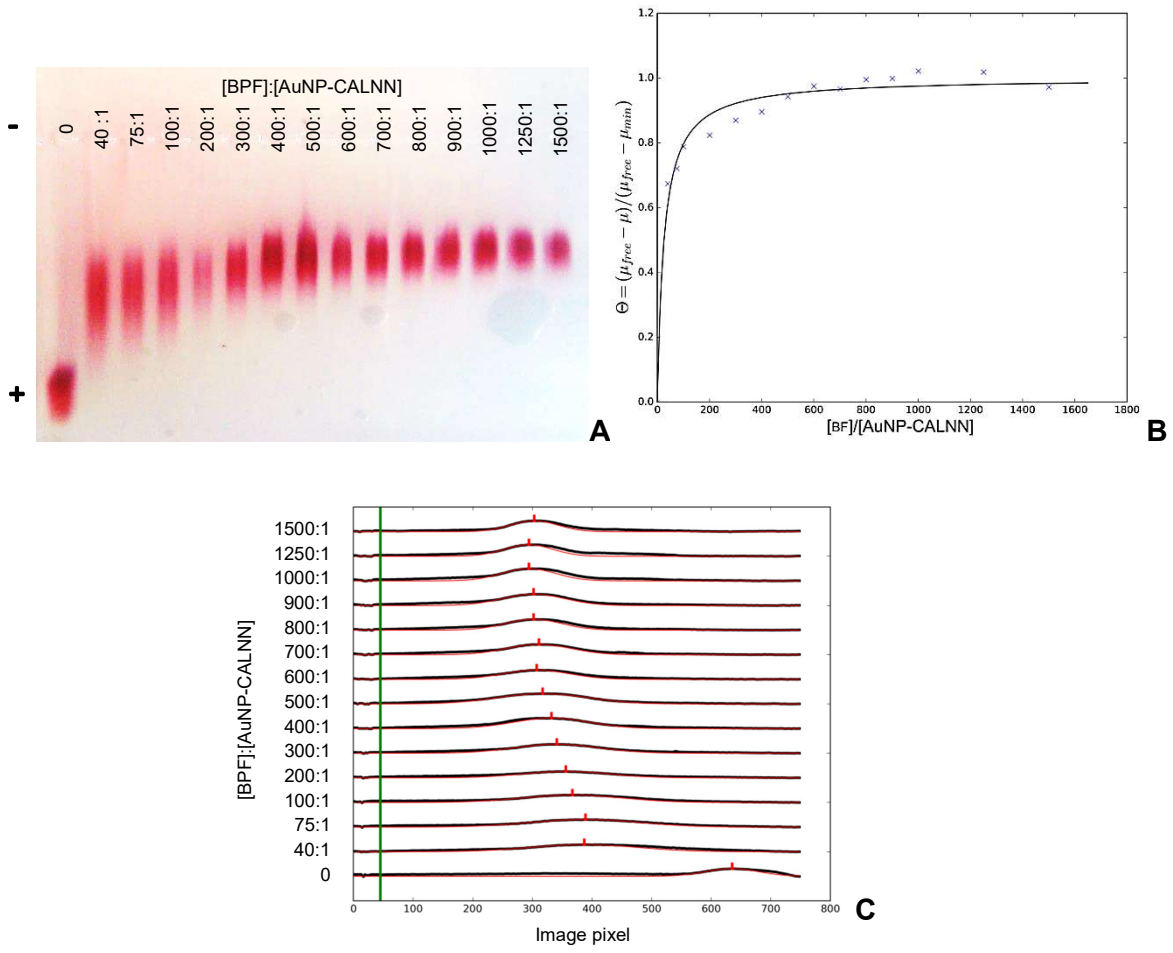

Figure 4.16. Electrophoretic mobility assay of BPF:AuNP-CALNN bionanoconjugates (**A**), its computed migration distances (**B**), and Langmuir isotherm plot (**C**).

Fibrinogen shows decreasing electrophoretic mobilities due to progressive nanoparticle coverage. Lanes with concentration ratios from 40:1-200:1 show broader bands, possibly due to the presence of several degrees of protein coverage. At 600:1 concentration ratio a full corona of bovine fibrinogen is observed. The Langmuir adsorption isotherm fitting these electrophoretic mobility results gives an equilibrium constant for fibrinogen binding to nanoparticle surface of K_{eq} = 3.91E-2 ± 1.08E-2 M^{-1}. The Hill cooperativity coefficient obtained by fitting the Hill equation to the data was n = 0.224, and the dissociation constant was K_d = 3.75E0 ± 2.33E-3 M^{-1}.

These results show that fibrinogen dissociation from nanoparticles is favoured as opposed to adsorption, due to the higher K_d constant obtained. In addition, the Hill coefficient is also low, maybe caused by negative cooperativity effects from adsorption of a high concentration of fibrinogen to nanoparticles. The fibrinogen concentration ratios promoted nanoparticle saturation, provoking dissociation of the fibrinogen corona.

Electrophoretic assays with transferrin have been disregarded due to the consistent aggregation of bionanoconjugates, visible in **Figure I.3**, **Supplementary data**. Owing to the impossibility of obtaining electrophoretic mobility values for transferrin bionanoconjugates, there was consequently not possible to obtain values for the binding constant K_{eq} from the Langmuir isotherm plot, neither for Hill coefficient n or dissociation constant K_d from the nanoparticle. Because of this, no information can be discussed on the transferrin saturation at nanoparticle surface.

4.8. Electrophoretic mobility of plasma-conjugated nanoparticles

Conjugation of nanoparticles with plasma samples enables the formation of plasma protein corona, mimicking the process of injecting nanoparticles into the bloodstream.

Figure 4.17 shows the electrophoretic mobility assays of two whole plasma-conjugated nanoparticles with increasing plasma concentrations.

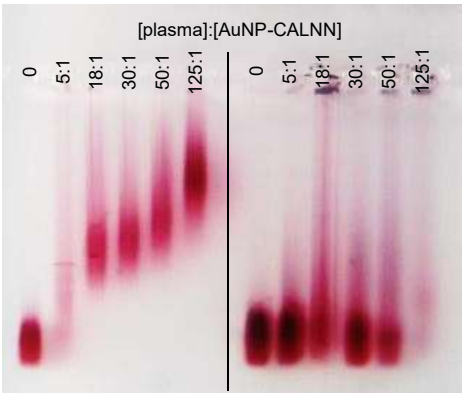

Figure 4.17. Electrophoretic mobility assays of AuNP-CALNN bionanoconjugates with increasing concentrations of two human plasma samples, from Instituto de Medicina Molecular (**A**), and Marta Giza (**B**).

The electrophoretic mobility assay in

Figure 4.17 A shows a distinct decrease in bionanoconjugate migration due to plasma protein corona formation at the nanoparticle surface. The 125:1 plasma protein to nanoparticle ratio was not high enough to reach a plateau, so it is still unclear if full nanoparticle coverage has been achieved. Nevertheless, the diffuse bands observed in this assay can be explained by the formation of multiple nanoparticle coronas with (1) distinct plasma protein quantities; and/or (2) different plasma protein content. These unevenly-coated nanoparticles would show variable molecular weights; and so their migrations would differ, even for the same plasma:nanoparticle ratio.

Assay of

Figure 4.17 B exhibits little or no variance in electrophoretic mobility of the plasma protein bionanoconjugates; hence it is reasonable to assume that (1) either adsorption to nanoparticles did not occur; or (2) there was a very small amount of plasma proteins conjugated with nanoparticles. Total protein concentration of 9 g/L, determined by BCA method and also observed in the SDS-PAGE in **Figure 4.1**, was lower in comparison to average plasma concentration; and this can explain the small difference in migration between unbound nanoparticles and plasma bionanoconjugates. Again, smeared bands in this assay can be a result of variable protein content and/or quantity for each ratio.

4.9. Hydrodynamic radii of AuNP-CALNN, plasma proteins and bionanoconjugates

The hydrodynamic radius of blood plasma proteins was determined by dynamic light scattering in order to compare these results with the hydrodynamic radius of bionanoconjugates and free nanoparticles, and characterize the diameter of protein corona around nanoparticles.

Volume distributions of dynamic light scattering data provide information about the proportionality between different size populations in suspension, and their autocorrelation curves elucidate on accuracy of measurements; while Z-average results are directly derived from $D_h = \frac{k_B T}{3\pi\eta D_t}$, **Equation 1.1** using cumulants technique on intensity light scattering data. Both results are important, either for the determination of diameter of bionanoconjugates, nanoparticles and proteins; or the assessment of consistent results during DLS experiments.

Dust and aggregates exhibit hydrodynamic radii in the size range of micrometres; a thousand times larger than the diameter of bionanoconjugates or even free proteins or nanoparticles in suspension. The scattered light by these entities is a million times more intense then the signal obtained for bionanoconjugates. This is why masking of hydrodynamic radii signal intensity of smaller nanoparticles or proteins, due to this scattering effect of aggregates or dust, is a major concern in DLS experiments. Consistently ‘good-fitting’ autocorrelation curves were the selection criteria in each measurement, and the hydrodynamic radius and Z-average results

described ahead are representative of meaningful experiments. Taking into account the effects of protein aggregation on the measured scattered light (see $I = I_0 \frac{1+\cos^2\theta}{2R^2}\left(\frac{2\pi}{\lambda}\right)^2\left(\frac{n^2-1}{n^2+2}\right)^2\left(\frac{d}{2}\right)^6$, **Equation 1.3** in ***1.3.2. Dynamic light scattering***), several protein concentrations were tested in order to detect consistent proteins' hydrodynamic radii. The results are shown below on **Table 4.5**.

Table 4.5. Hydrodynamic radii of plasma proteins determined using dynamic light scattering.

Protein	Concentration	Z-average (nm)
BSA	50 g/L	9.0
	25 g/L	8.8
	12.5 g/L	8.8
HSA	10 g/L	9.5
BPF	12.5 g/L	320.8

Hydrodynamic radius of bovine albumin was determined to be 8.8 nm, or 88 Å. Radii of 313 Å, 2061 Å and 3208 Å were determined and attributed to protein aggregation and dust contaminants. This protein showed satisfactory results for all the concentrations tested. For human albumin 9.52 nm was the resulting hydrodynamic radius (

Figure 4.18); other measurements of 790 Å, 21114 Å, and 2053 Å were assigned to dust or protein aggregates.

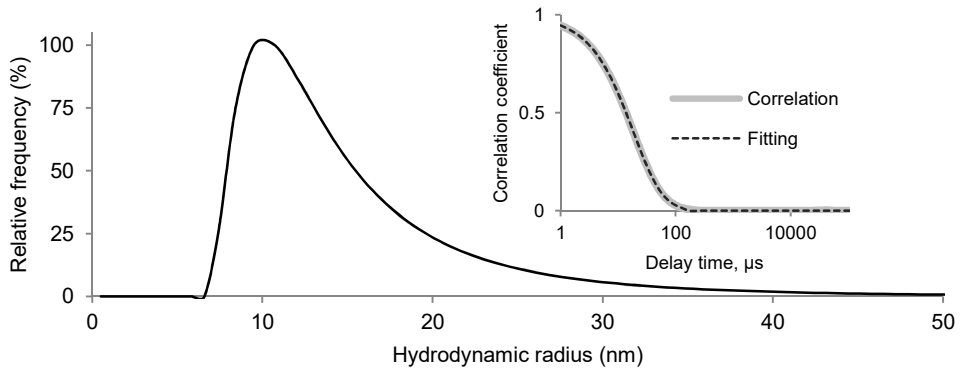

Figure 4.18. Volume distribution of human serum albumin 10 g/L. Inlet shows autocorrelation curve.

Fibrinogen showed an average hydrodynamic radius of 3208 Å, corroborating the value described by Hall *et al.*, and the computational result in **Figure 4.6**. Different assays resulted in 16113 Å that were assigned to polymerization of fibrinogen [25], protein aggregates or dust contamination. Human transferrin's hydrodynamic radius was measured as 4361 Å. Protein aggregation was also detected with a value of 12753 Å.

Light scattering assays of unconjugated nanoparticles provide useful information for size determination of the protein corona, by comparison of the hydrodynamic radii of bionanoconjugates with the ones of free proteins and nanoparticles. The following volume distributions of hydrodynamic radii of bionanoconjugates of three distinct plasma proteins are representative of at least three distinct measurements.

Figure 4.19 shows volume distribution of albumin bionanoconjugates with increasing protein:nanoparticle ratios. The free nanoparticles show a sharp peak at 15.9 nm, with Z-average of 24.6 nm.

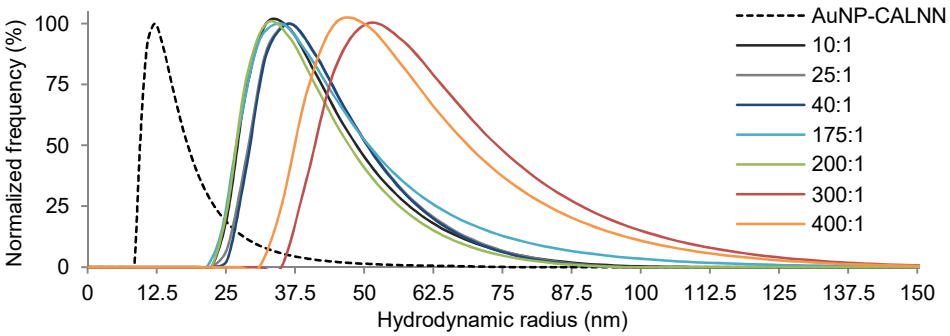

Figure 4.19. Volume distribution of gold bionanoconjugates with increasing human albumin ratios.

From the volume distributions of albumin bionanoconjugates in **Figure 4.19**, a two-sized population seems apparent; one composed of lower concentration ratios of human albumin which shows smaller hydrodynamic radii of *circa* 37 nm, and other with larger radii of about 50 nm correspondent with higher [HSA]:[AuNP-CALNN] ratios bionanoconjugates. This can be explained by saturation of nanoparticle surface with higher protein concentration ratios, resulting in adsorption of larger number of albumin proteins at the AuNP surface.

Comparing the hydrodynamic radius of this 'lower concentration ratios' population (D_h = 37 nm) with the radius of nanoparticles alone (D_h = 16 nm) gives information on the size of protein corona of bionanoconjugates with lower [HSA]:[AuNP-CALNN] ratios. The value for this radius is about the size of a human albumin hydrodynamic radius (D_h = 9.5 nm) forming a monolayer around the nanoparticle with side-on adsorption orientation.

Repeating this logic for the 'higher concentration ratios' albumin bionanoconjugates, the result obtained for the estimated hydrodynamic radius of protein corona is 17 nm. This value is not enough to 'fit' two albumin proteins around a nanoparticle to form a double layer protein corona. However, if adsorption to nanoparticles promotes conformational changes in the protein structure, this could explain the formation of a corona of 17 nm with albumin proteins having a tighter packing around the nanoparticle.

Other globular protein of blood plasma is transferrin. Its bionanoconjugates do not show different size populations as seen for human albumin, but instead have increasing bionanoconjugate hydrodynamic radii as the concentration ratios are higher (**Figure 4.20**).

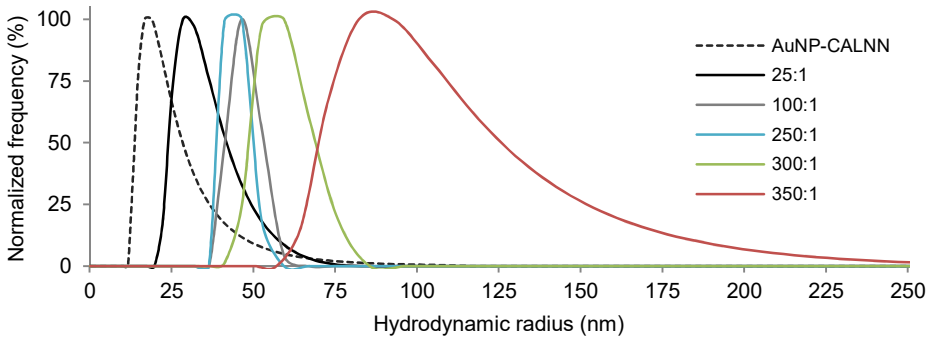

Figure 4.20. Volume distribution of gold bionanoconjugates with increasing transferrin ratios.

Nanoparticles alone show a hydrodynamic radius of 16.8 nm. From the volume distributions of bionanoconjugates of transferrin with increasing protein:nanoparticle ratios, hydrodynamic radii increase from 28.5 nm, 46.5 nm, 59.4 nm up to 82.3 nm (concentration ratios of 25:1, 100:1 and 250:1, 300:1, 350:1; respectively). Because no binding constants could be obtained for transferrin adsorption to the nanoparticle surface (see ***1.2. Electrophoretic mobility of AuNP-CALNN bionanoconjugates***), it was impossible to determine if these concentration ratios were high enough to produce a full protein corona. If they were, transferrin's K_{eq} would be lower than the dissociation constant K_d and the dissociation of transferrin to the medium would be favoured. On the other hand, if these ratios are too low to achieve a complete protein corona, the favoured adsorption process would reflect on a high value of binding constant to the nanoparticle surface.

Figure 4.21 shows volume distributions of hydrodynamic radius of bionanoconjugates of bovine fibrinogen with increasing protein:nanoparticle ratios.

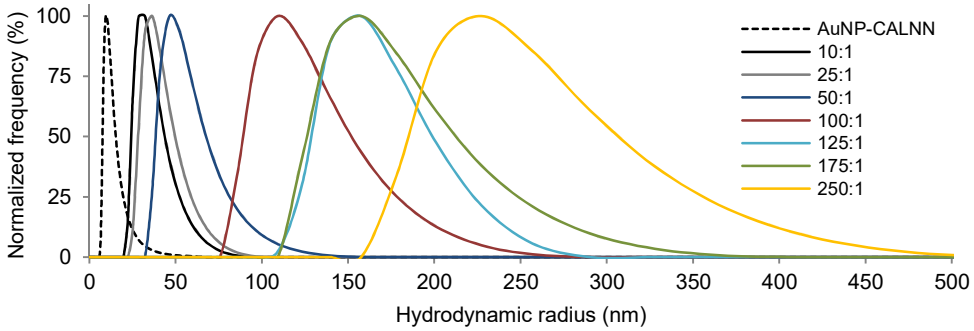

Figure 4.21. Volume distribution of gold bionanoconjugates with increasing fibrinogen ratios.

The hydrodynamic radius of unbound nanoparticles showed an average diameter of 16.9 nm. 10:1 fibrinogen:nanoparticle bionanoconjugates show a hydrodynamic radius of 32.3 nm; 25:1 ratio has a hydrodynamic radius of 36.4 nm, and 50:1 ratio bionanoconjugate is 46.5 nm.

The lower protein:nanoparticle ratios display little variance between themselves, which can point to a different adsorption preference to the nanoparticle surface. Fibrinogen has a central region with positive net charge (see **Figure 4.11**), which can easily interact with the overall negative nanoparticle surface. Due to its fibrillar shape, this could promote wrapping process around the nanoparticle creating a fibrinogen corona with a different adsorption orientation than the predicted end-on (**Figure 4.8**).

This wrapping event could generate bionanoconjugates showing hydrodynamic radii lower than the ones expected form an end-on adsorption orientation. Lower fibrinogen:nanoparticle ratios show radii differences up to 29.6 nm; which, again due to conformational changes upon adsorption of the firinogen's central region to the nanoparticle, would be a possible monolayer protein corona.

Higher fibrinogen:nanoparticle concentration ratios display increasing hydrodynamic radii of 109.3 nm for 100:1; 157.6 nm for 125:1 and 175:1 concentration ratios; and 201.2 nm for 250:1 fibrinogen:nanoparticle concentration ratio. From the electrophoretic data discussed earlier (see ***1.1. Electrophoretic mobility of AuNP-CALNN bionanoconjugates***), these concentration ratios produced a Langmuir binding constant for fibrinogen adsorption lower than the dissociation constant obtained by the Hill equation; supporting that nanoparticle saturation was achieved and fibrinogen concentration ratios promote some uncooperative binding events due to the Hill coefficient of n =0.224.

4.10. Zeta-potential of albumin bionanoconjugates

Zeta-potential values were determined for different HSA ratios at AuNP-CALNN surface by relating electrophoretic mobilities with increasing agarose percentages ($log(\mu_e) = log(\ _0) - K_r\ .T$, **Equation 1.5**). The digital images of HSA:AuNP-CALNN bionanoconjugates electrophoretic mobility assays with increasing agarose percentages are presented in **Supplementary data**, **Figure I.4**). .

As described by Pons *et al.* [40] and Rodbard *et al.* [35], the increase of agarose percentage on a gel tightens the polymer mesh by decreasing pore size, making electrophoretic movement of bionanoconjugates decrease. Relating the two parameters and converting the results with $\zeta = \frac{3\eta_s\mu_0}{2\epsilon_s.H(\kappa R)}$, **Equation 1.6**, one can derive the zeta-potential value for free nanoparticles and HSA bionanoconjugates with different protein concentration ratios.

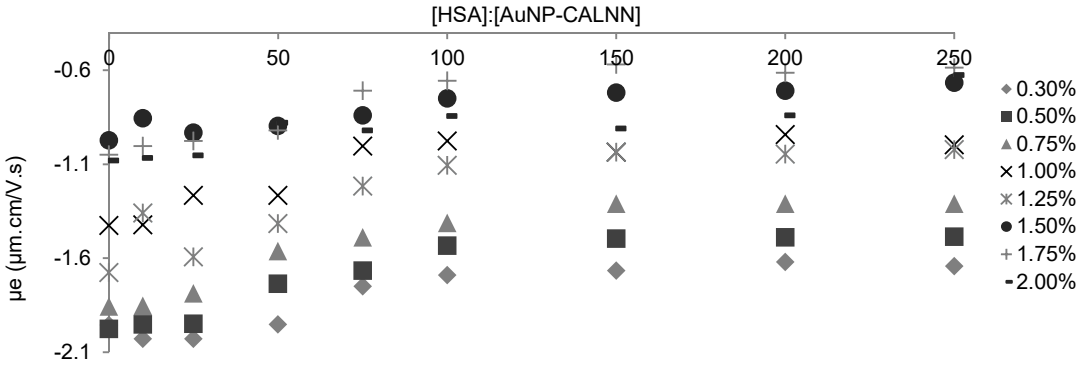

Figure 4.22. Electrophoretic mobility values for AuNP-CALNN albumin bionanoconjugates with increasing protein concentration ratios.

From **Figure 4.22**, a gradual loss of mobility is visible with increase of agarose concentration. This is a result of decrease of agarose pore size, slowing down the migration of bionanoconjugates and nanoparticles. Plotting the logarithm of electrophoretic mobility against agarose percentage, $log(\mu e) = log(\mu 0) - Kr \cdot T$, **Equation 1.5** can be determined (**Figure 4.23** and **Table 4.6**).

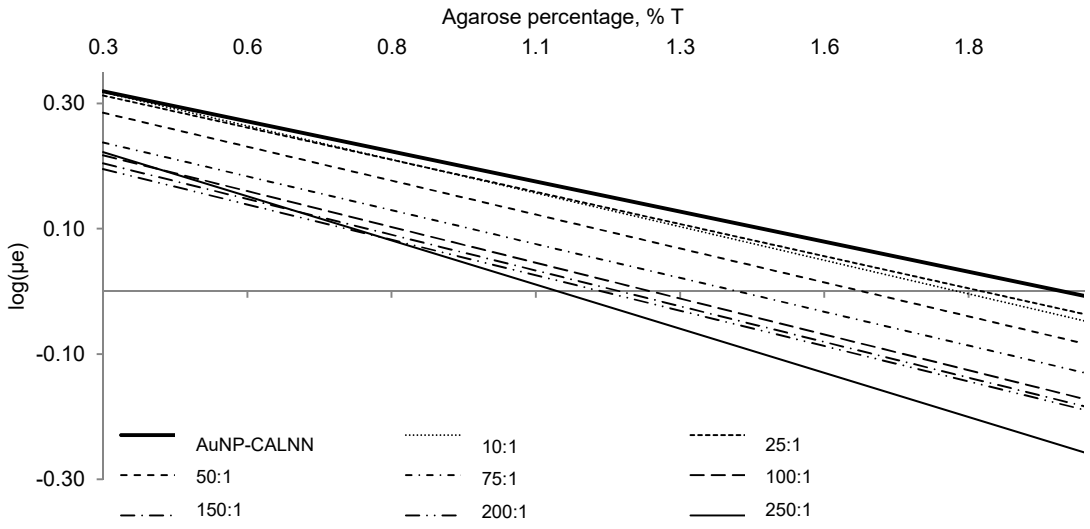

Figure 4.23. Logarithm of electrophoretic mobility *versus* agarose percentage for AuNP-CALNN albumin bionanoconjugates with increasing protein concentration ratios.

Table 4.6. Electrophoretic mobility results of bionanoconjugates for each AuNP-CALNN:HSA concentration ratio with increasing agarose percentage.

[HSA]:[AuNP-CALNN]	-Kr	$\log(\mu_e)$	R^2
0	-0.1919	0.3768	0.8023
10	-0.2146	0.3822	0.8237
25	-0.2055	0.3746	0.8031
50	-0.2168	0.3502	0.9067

75	-0.2164	0.3028	0.8047
100	-0.2286	0.2857	0.8318
150	-0.228	0.2727	0.7588
200	-0.2262	0.2631	0.8063
250	-0.2819	0.3068	0.9399

Figure 4.24 shows zeta-potential values for gold nanoparticles and bionanoconjugates of albumin with increasing concentration ratios, derived from $log(\mu_e) = log\ \ _0) - K_r\ .T$, **Equation 1.5** and converted using $\zeta = \frac{3\eta_s\mu_0}{2\epsilon_s.H(\kappa R)}$, **Equation 1.6**.

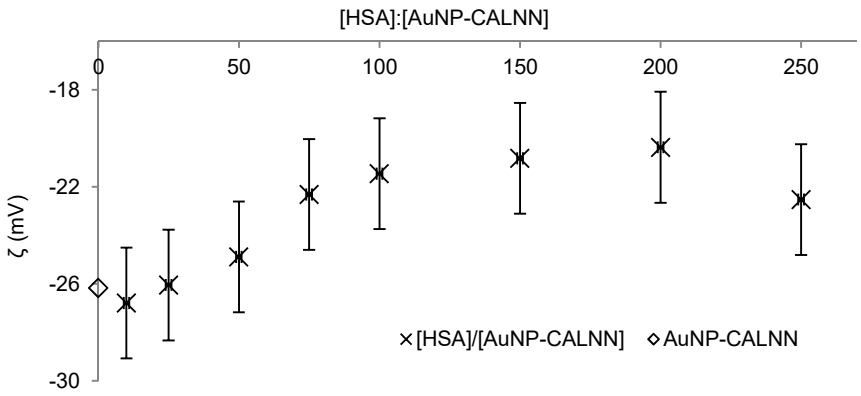

Figure 4.24. Zeta-potential values for HSA:AuNP-CALNN bionanoconjugates with increasing protein:nanoparticle ratios.

The results show a decrease in zeta-potential values for bionanoconjugates with concentration ratios starting on 25:1 to 250:1, with values from -26.05 mV up to -20.36 mV, when comparing with free gold nanoparticles (ζ= -26.16 ± 2.28 mV). The adsorption of albumin produces an increase in molecular weight of the nanoparticles, promoting shielding of the negative surface charge of the nanoparticle. This reflects on the displacement of the shear plane to lower potential values (see ***1.4.3. Zeta-potential***).

Variation between zeta-potential values (Δζ= 5.8 mV) is not enough to bring the potentials out of the colloidal stability range, so no significant flocculation of the bionanoconjugates was observed (see **Supplementary data**, **Figure I.4**). This means that conjugation with albumin proteins produces stable and dispersed bionanoconjugates.

4.11. Protein-ligand docking

4.11.1. Binding modes of CALNN peptide

The synthetic CALNN peptide is generally used in bionanotechnology to functionalize nanoparticles, creating an amino acid layer prone to interact with medium proteins and macromolecules. This capping agent is covalently bound to the nanoparticle from its cysteine

(C) terminal residue, exposing its alanine (A), leucine (L) and two asparagines (N). The first two are hydrophobic amino acids, and the asparagine residues provide functional groups for protein interaction – amine and carboxylic groups for hydrogen bonds, and two aliphatic side chains for non-polar interactions.

The purpose of this docking assay was to identify which binding modes for CALNN peptide would be valid, as this peptide is restricted to interact with proteins through its arginines residues, because of the sulphur covalent bond with gold nanoparticles. The transferrin-CALNN docking assay produced nine CALNN modes, revealing nine possible sites for this peptide to bind to this protein (**Figure 4.25**, and **Supplementary data**, **Table I.4**). The docking experiments revealed a localized preference of CALNN peptide on the transferrin structure. Most CALNN binding modes obtained were interacting with residues in the left lobe of transferrin (**Figure 4.25**, Front view).

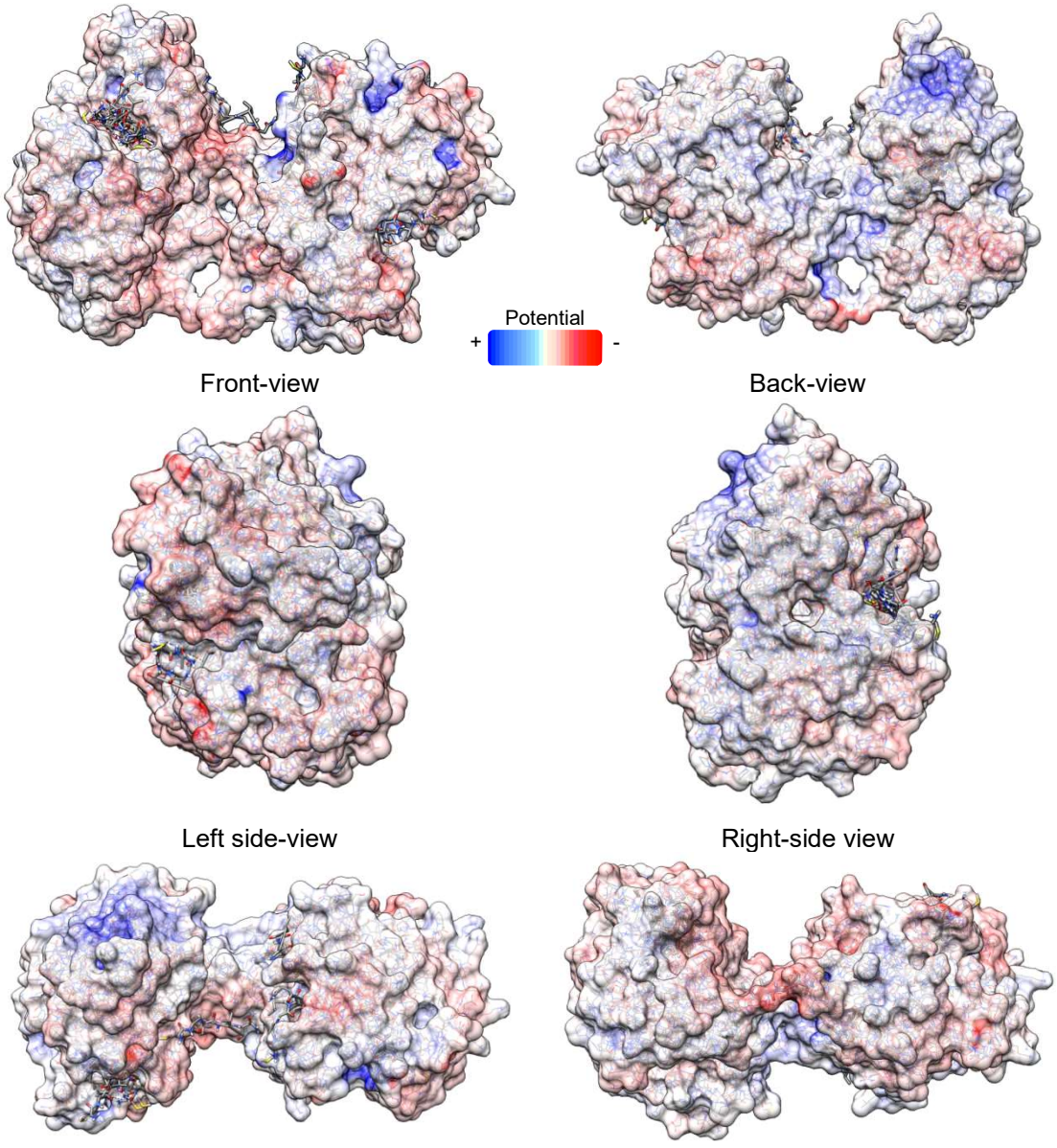

Top-view Bottom-view

Figure 4.25. Molecular visualizations of nine CALNN peptide modes on human transferrin (PDB 3V83) at pH 7.4.

This result contradicts the interpretation of transferrin's electrostatic potential surface made before (see ***4.5. Electrostatic potential surfaces of plasma proteins***), were the negatively-charged right lobe of transferrin was suggested for the most probable interaction site of CALNN peptide. However, docking results showed that the aliphatic interactions of asparagine's side chain, alanine and leucine prevailed over the van der Waals interactions between close opposite-charged nuclei. Most of the binding modes found seem to be making non-polar interactions with residues on the left lobe transferrin (**Figure 4.25**, Top-view). The hydrophobic interactions predicted above could only be made by the aliphatic side chains of asparagine, alanine or leucine residues, meaning that the prevalent CALNN binding modes are not performed through the cysteine residue.

Even though the binding modes obtained were valid for this docking assay, there is one more aspect to address in the interpretation of these results: these docking assays were performed using the CALNN peptide as a free ligand and, by doing so there was no limitation for binding modes via the cysteine residue of CALNN. In fact this does not reflect the reality, where CALNN peptide interactions are restricted to the exposed residues and the cysteine sulphur atom is covalently bound to gold. One suggestion for the improvement of this interaction search is to restrict binding modes that interact through the cysteine sulphur atom.

To develop on this CALNN orientation restriction, and based on the assumption that the C-terminus of CALNN exhibits higher mobility and thus higher interaction with transferrin, and that its cysteine and alanine residues are tightly bound to the AuNP surface, a second protein-ligand docking assay was performed using a hypothetical NNN peptide and human transferrin. This transferrin-NNN docking assay produced nine NNN modes, revealing nine possible binding sites for this peptide to bind to transferrin (**Figure 4.26**, and **Supplementary data**, **Table I.5**).

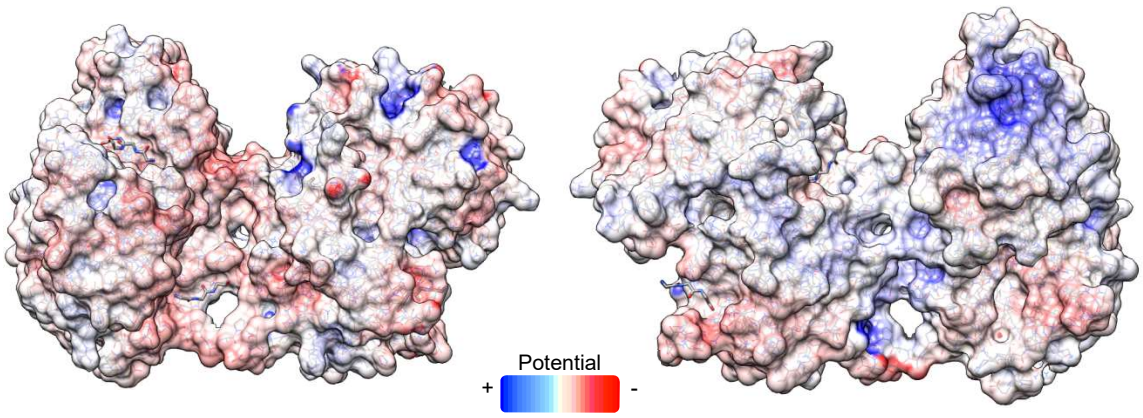

Front-view Back-view

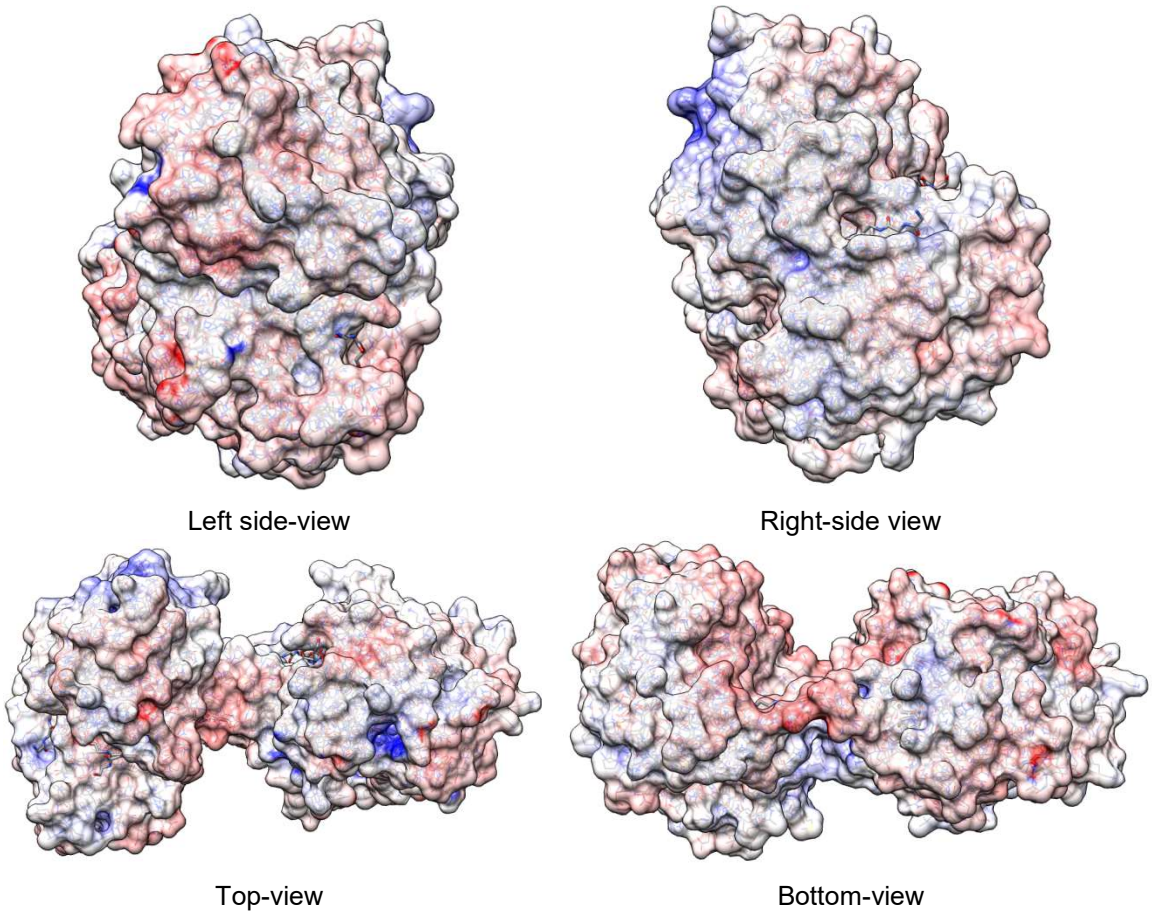

Figure 4.26. Molecular visualizations of nine NNN peptide modes on human transferrim (PDB 3V83) at pH 7.4.

The results obtained from this docking experiment were surprisingly different from the ones obtained before: the nine NNN peptide binding modes obtained showed a homogeneous distribution on transferrin's surface as opposing to the results obtained for CALNN peptide. The three asparagines revealed interactions with hydrophobic and/or aliphatic sites of transferrin (**Figure 4.26**). As no interaction site was particularly obvious with this docking assay, the interpretation of the electrostatic potential surface of transferrin (see **Figure 4.10.** Electrostatic potential surface of human transferrin at pH 7.4. and **Supplementary data, Figure I.7**) is maintained, and aliphatic interactions with the upper right lobe residues seems an acceptable argument for the adsorption of transferrin to nanoparticles.

From these docking experiments one can conclude that (1) the results for NNN peptide were inconclusive, and (2) the CALNN peptide docking produced acceptable results for the prediction of valid binding modes for interaction with plasma proteins. Given this, a new docking approach was taken to investigate the possible interaction sites when nanoparticles become in contact with plasma proteins.

4.11.2. Interaction sites for nanoparticle interaction

The following docking experiment was performed by increasing the number of binding modes generated, and lowering the accuracy of the search space. The idea behind this was to estimate if there would be a particular location on the protein structure where CALNN peptide shows a higher affinity to. This could represent the interaction site of gold nanoparticles as they encounter plasma proteins in the bloodstream. Docking results of human transferrin-CALNN are presented in **Figure 4.27**, and the binding modes are colored from cyan to magenta, from the lowest to the highest B-factor.

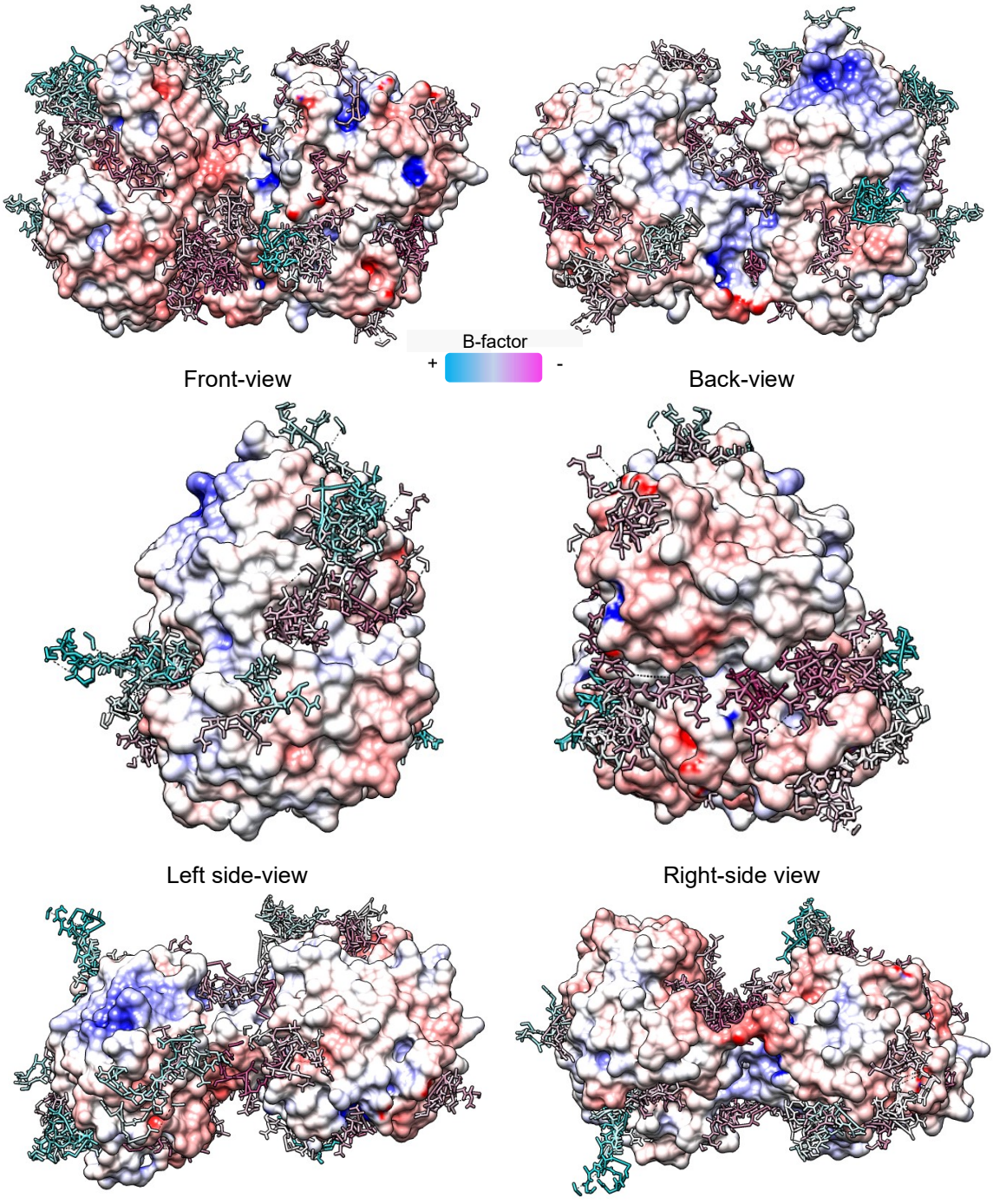

Top-view Bottom-view

Figure 4.27. Molecular visualizations of CALNN peptide modes on human transferrim (PDB 3V83) at pH 7.4.

The results obtained for this docking assay show heterogeneous distribution of CALNN peptide throughout transferrin surface. Apparently the regions showing mostly neutral or positive charges have higher affinity for CALNN peptide, because in these areas the temperature factors of CALNN are higher. Transferrin's right-side view in **Figure 4.27** shows a particular 'hot spot' for CALNN affinity, due to the intense magenta coloring representative of high B-factor. This high temperature is proportional to the binding energy for this interaction. It seems that CALNN hydrophobic residues have a great importance in the interaction with proteins, and these are observed preferentially in complementary hydrophobic regions. Another docking experiment was performed using human albumin (**Figure 4.28**), with the same color scale for CALNN temperature factor as before.

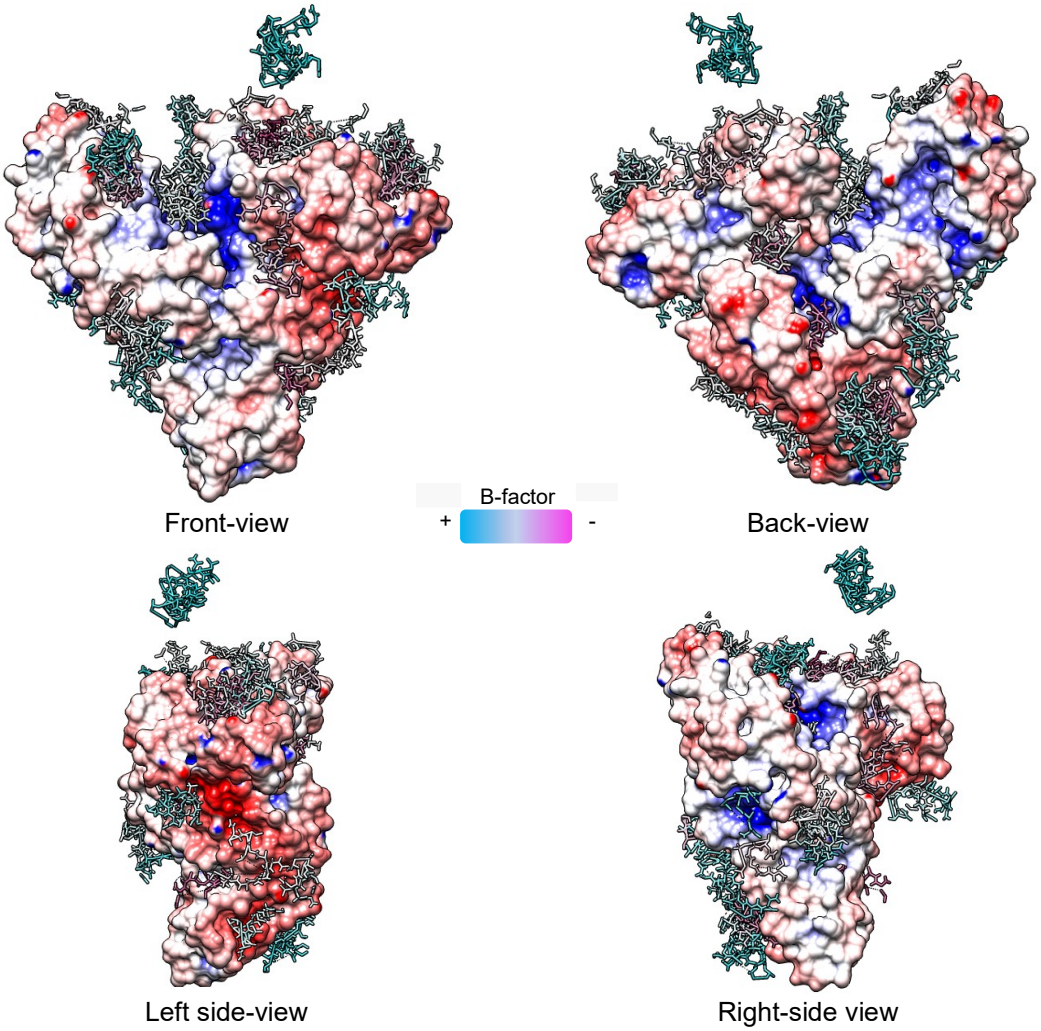

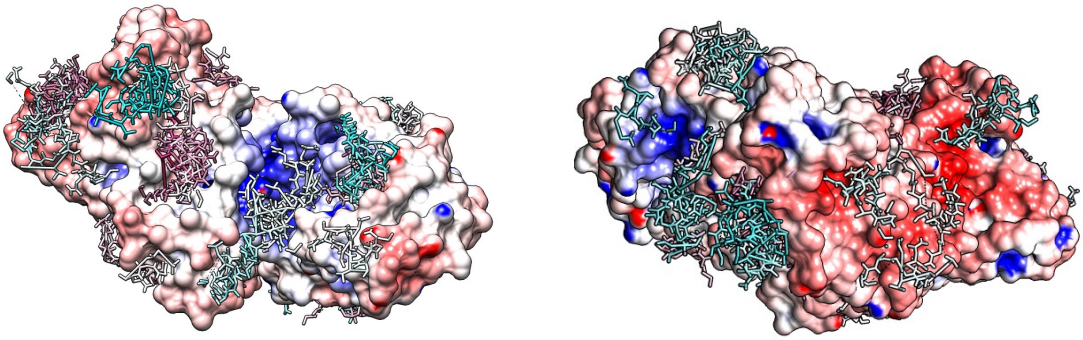

Top-view Bottom-view

Figure 4.28. Molecular visualizations of CALNN peptide modes on human albumin (PDB 3E7I) at pH 7.4.

These docking results are in fact similar to the ones found for transferrin. The preferred interactions of CALNN are low positive charges and mostly neutral surfaces (**Figure 4.28**, front-view, on the upper left side of albumin). This indicates for aliphatic and hydrophobic interactions between the protein's residues and alanine, leucine and arginine hydrophobic side chains.

My final suggestion for this process is that interaction of CALNN-functionalized nanoparticles is made preferentially via its hydrophobic and aliphatic side chains onto the hydrophobic regions of plasma proteins.

4.12. A first glance into the adsorption mechanism of plasma proteins to gold nanoparticles

After intravenous injection, functionalized gold nanoparticles enter the bloodstream and are in contact with all the biomolecules present in this physiological medium. These spherical gold nanoparticles exhibit between themselves a face-centered cubic packing, the same packing geometry as observed inside protein structures, which are also in circulation in the aqueous phase of the blood: the plasma. Due to their conducting valence electron shell, gold nanoparticles have characteristic physicochemical properties, such as negative surface charge and stability within ± 30 mV zeta-potential range. The functionalization process has provided gold nanoparticles the ability to produce hydrophobic interactions between the capping agent's aliphatic side chains with hydrophobic regions of albumin and transferrin. These interactions give rise to protein adsorption at the nanoparticle surface, showing for albumin a minimum 200:1 concentration ratio with a side-on orientation adsorption, orientation also predicted for transferrin. For fibrillary-shaped fibrinogen this value is 600:1, and its adsorption happens from its positively-charged central region promoting chain wrapping around the nanoparticle. Uncooperativity effects are observed for multiple protein adsorptions, favouring the dissociation of proteins from the nanoparticle.

5. Conclusions

The formation of a plasma protein corona around nanoparticles is a dynamic process determined by protein availability and affinity to the AuNP surface, as well as physiological conditions and the individual's plasma proteome. Whole plasma SDS-PAGE determined that human albumin, fibrinogen and transferrin were in fact part of the human blood proteome. Synthesis of gold nanoparticles by the citrate reduction method produces nanospheres with diameters from 10-30 nm that, when functionalized with the pentapeptide CALNN, show exposed amino acid residues capable of interacting with circulating blood proteins creating bionanoconjugates. A monolayer protein corona of seventeen albumin and eighteen transferrin proteins with a side-on adsorption orientation was predicted using a fcc packing geometry. Establishment of protein:nanoparticle concentration ratios promoters of protein corona formation around nanoparticles have been applied to agarose gel electrophoresis; in which the decrease in bionanoconjugates migration relative to nanoparticles alone proofs the formation of protein corona, and Langmuir and Hill equation fittings allow determination of binding and dissociation constants for nanoparticle adsorption; as well as estimation of cooperativity behaviour of protein binding from the Hill coefficient. Both albumin and fibrinogen showed nanoparticle corona saturation, supported by higher dissociation constants and low Hill cooperativity coefficients. Albumin and fibrinogen bionanoconjugates show formation of protein corona with 200:1 and 600:1 [protein]:[nanoparticle] ratios, respectively. Zeta-potential determination of albumin bionanoconjugates resulted in potentially stable colloidal bionanoconjugates that shield the nanoparticle's -26.16 mV potentials decreasing its surface charge up to -20.36 mV. DLS methods on albumin bionanoconjugates enabled the detection of a monolayered and two-layered protein corona with the increase in [HSA]:[AuNP-CALNN] ratio; while for fibrinogen the hydrodynamic radii obtained suggested wrapping effect upon adsorption to nanoparticles. Transferrin bionanoconjugates showed increase in hydrodynamic radius linearly with the increase in protein:nanoparticle ratios. Aggregation issues impaired the determination of binding constants, cooperativity coefficients, molecular weight and electrophoretic mobilities for transferrin bionanoconjugates. Plasma proteins electrostatic potential surfaces also provide information on surface charge, and unveil details on binding sites at nanoparticle surface. Human albumin shows predominant interaction sites via its hydrophobic pockets by aliphatic interactions with CALNN hydrophobic side chains; transferrin hydrophobic regions also show high affinity for CALNN aliphatic interaction; and fibrinogen shows two adsorption orientation preferences: side-on via its negatively-charged nodular termini, or through its positively-charged central region promoting wrapping around the nanoparticle. Understanding and combining these very distinct properties will allow the creation of nanoparticle surface models for predicting adsorption events of one, and in the future, multiple plasma proteins in the bloodstream. This can further develop into a model and hopefully into a mechanistic understanding of plasma proteins adsorption to gold nanoparticles, and unravel glowing applications in bionanotechnology.

Blank page

6. References

1. Franco, R. & Pereira, E. in *Encyclopedia of Metalloproteins* 908–915 (Springer, 2013). doi:10.1017/CBO9781107415324.004
2. Doria, G. *et al.* Noble metal nanoparticles for biosensing applications. *Sensors* **12,** 1657–1687 (2012).
3. Sperling, R. a & Parak, W. J. Surface modification, functionalization and bioconjugation of colloidal inorganic nanoparticles. *Philos. Trans. A. Math. Phys. Eng. Sci.* **368,** 1333–1383 (2010).
4. Rahman, M., Laurent, S., Tawil, N., Yahia, L. & Mahmoudi, M. Protein-Nanoparticle Interactions. **15,** 21–45 (2013).
5. Liz-Marzán, L. M. Nanometals. *Mater. Today* **7,** 26–31 (2004).
6. Iberian Nanotechnology Laboratory. (2015). Available at: www.inl.int.
7. Amendola, V. *et al. Chapter 3 - Physico-Chemical Characteristics of Gold Nanoparticles*. *Gold Nanoparticles in Analytical Chemistry* **66,** (2014).
8. Ramer, G. & Lendl, B. *Spectroscopic Techniques for Characterization of Gold Nanoparticles*. *Comprehensive Analytical Chemistry* **66,** (Elsevier, 2014).
9. Nanocomposix.eu. Gold Nanoparticles: Optical Properties. (2016).
10. Gold: Chemistry , Materials and Catalysis. *Chem. Soc. Rev.* **37,** 1909–30 (2008).
11. Lévy, R. *et al.* Rational and combinatorial design of peptide capping ligands for gold nanoparticles. *J. Am. Chem. Soc.* **126,** 10076–10084 (2004).
12. Peixoto de Almeida, M. *et al. Gold Nanoparticles as (Bio)Chemical Sensors*. *Comprehensive Analytical Chemistry* **66,** (2014).
13. Rocha, S. *et al.* Influence of fluorinated and hydrogenated nanoparticles on the structure and fibrillogenesis of amyloid beta-peptide. *Biophys. Chem.* **137,** 35–42 (2008).
14. Goy-López, S. *et al.* Physicochemical characteristics of protein-NP bioconjugates: The role of particle curvature and solution conditions on human serum albumin conformation and fibrillogenesis inhibition. *Langmuir* **28,** 9113–9126 (2012).
15. Nanjappa, V. *et al.* Plasma Proteome Database as a resource for proteomics research : 2014 update. **42,** 959–965 (2014).
16. Hajipour, M. J. *et al.* Personalized protein coronas: a 'key' factor at the nanobiointerface. *Biomater. Sci.* **2,** 1210 (2014).
17. Swaminathan, R. in *Handbook of Clinical Biochemistry* 149–161 (World Scientific, 2011).
18. Okutucu, B., Dınçer, A., Habib, Ö. & Zıhnıoglu, F. Comparison of five methods for determination of total plasma protein concentration. *J. Biochem. Biophys. Methods* **70,** 709–711 (2007).
19. Walkey, C. D. & Chan, W. C. W. Understanding and controlling the interaction of nanomaterials with proteins in a physiological environment. *Chem. Soc. Rev.* **41,** 2780–99 (2012).
20. Bhattacharya, A. A., Grüne, T. & Curry, S. Crystallographic analysis reveals common modes of binding of medium and long-chain fatty acids to human serum albumin. *J. Mol. Biol.* **303,** 721–732 (2000).
21. Boldt, J. Use of albumin: An update. *Br. J. Anaesth.* **104,** 276–284 (2010).
22. Kragh-Hansen U., M. L. Albumin Website. (2015). Available at: albumin.org/.
23. Muszbek, L., Bagoly, Z., Bereczky, Z. & Katona, E. The involvement of blood coagulation factor XIII in fibrinolysis and thrombosis. *Cardiovasc. Hematol. Agents Med. Chem.* **6,** 190–205 (2008).
24. Tennent, G. a *et al.* Human plasma fibrinogen is synthesized in the liver Human plasma fibrinogen is synthesized in the liver Short title : **109,** 1971–1975 (2009).

25. HALL, C. E. & SLAYTER, H. S. The fibrinogen molecule: its size, shape, and mode of polymerization. *J. Biophys. Biochem. Cytol.* **5,** 11–6 (1959).
26. Kollman, J. M. *et al.* Crystal Structure of Human Fibrinogen Crystal Structure of Human Fibrinogen †,‡. (2009). doi:10.1021/bi802205g
27. Lambert, L. A., Perri, H., Halbrooks, P. J. & Mason, A. B. Evolution of the transferrin family : Conservation of residues associated with iron and anion binding. **142,** 129–141 (2005).
28. Chung, M. C. M. Stucture and function of transferrin. *Biochem. Educ.* **12,** 146–154 (1984).
29. Hall, D. R., Leonard, G. A., Neu, M. & Lindley, P. F. research papers The crystal and molecular structures of diferric porcine and rabbit serum transferrins at resolutions Ê , respectively research papers. 70–80 (2002).
30. Neil Humphrey. When the Invisible Becomes Visible. (2016). Available at: http://possibility.teledynedalsa.com/invisible-becomes-visible/.
31. Ghosh, S. K. & Pal, T. Interparticle Coupling Effect on the Surface Plasmon Resonance of Gold Nanoparticles: From Theory to Applications. *Chem. Rev.* **107,** 4797–4862 (2007).
32. Park, S. & Hamad-Schifferli, K. Evaluation of hydrodynamic size and zeta-potential of surface-modified Au nanoparticle-DNA conjugates via ferguson analysis. *J. Phys. Chem. C* **112,** 7611–7616 (2008).
33. Johnson, C. S. & Gabriel, D. A. Laser Light Scattering. (1994).
34. Jans, H., Liu, X., Austin, L., Maes, G. & Huo, Q. Dynamic light scattering as a powerful tool for gold nanoparticle bioconjugation and biomolecular binding studies. *Anal. Chem.* **81,** 9425–9432 (2009).
35. Rodbard, D. & Chrambach, A. Unified theory for gel electrophoresis and gel filtration. *Proc. Natl. Acad. Sci. U. S. A.* **65,** 970–977 (1970).
36. Sandström, P. & Åkerman, B. Electrophoretic properties of DNA-modified colloidal gold nanoparticles. *Langmuir* **20,** 4182–4186 (2004).
37. Genome Research Limited. Gel Electrophoresis. (2016). Available at: http://www.yourgenome.org/facts/what-is-gel-electrophoresis.
38. Shapiro, a L., Viñuela, E. & Maizel, J. V. Molecular weight estimation of polypeptide chains by electrophoresis in SDS-polyacrylamide gels. *Biochem. Biophys. Res. Commun.* **28,** 815–820 (1967).
39. David R. Caprette. Introduction to SDS-PAGE. (2016). Available at: http://www.ruf.rice.edu/~bioslabs/studies/sds-page/gellab2.html.
40. Pons, T., Uyeda, H. T., Medintz, I. L. & Mattoussi, H. Hydrodynamic dimensions, electrophoretic mobility, and stability of hydrophilic quantum dots. *J. Phys. Chem. B* **110,** 20308–20316 (2006).
41. Particle Sciences. An Overview of the Zeta Potential. *Part. Sci.* **2,** 1–4 (2012).
42. Dougherty, G. M. *et al.* The zeta potential of surface-functionalized metallic nanorod particles in aqueous solution. *Electrophoresis* **29,** 1131–1139 (2008).
43. Zuo, G., Huang, Q., Wei, G., Zhou, R. & Fang, H. Plugging into proteins: Poisoning protein function by a hydrophobic nanoparticle. *ACS Nano* **4,** 7508–7514 (2010).
44. APBS & PDB2PDBQT Online Server. (2016). Available at: http://www.poissonboltzmann.org/.
45. Implicit solvation. *2016* Available at: http://personalpages.manchester.ac.uk/staff/neil.burton/.
46. Bondi, A. van der Waals Volumes and Radii. *J. Phys. Chem.* **68,** 441–451 (1964).
47. Morris, G. M. & Lim-Wilby, M. Molecular docking. *Methods Mol. Biol.* **443,** 365–382 (2008).
48. Van Rijt, S. H., Bein, T. & Meiners, S. Medical nanoparticles for next generation drug delivery to the lungs. *Eur. Respir. J.* **44,** 765–774 (2014).
49. Murzin, D. Y. On the validity of Langmuir adsorption on supported nanoparticles. *React. Kinet.*

Catal. Lett. **91,** 37–43 (2007).

50. Langmuir, I. The Adsorption of Gases on Plane Surfaces of Glass, Mica and Platinum. *J. Am. Chem. Soc.* **40,** 1361–1403 (1918).
51. Hill, A. V. The possible effects of the aggregation of the molecule of hemoglobin on its dissociation curves. *J. Physiol.* **40,** iv–vii (1910).
52. Petkov, V. *et al.* Structure of gold nanoparticles suspended in water studied by x-ray diffraction and computer simulations. *Phys. Rev. B - Condens. Matter Mater. Phys.* **72,** 1–8 (2005).
53. Kao, P. *et al.* Volumetric interpretation of protein adsorption: Interfacial packing of protein adsorbed to hydrophobic surfaces from surface-saturating solution concentrations. *Biomaterials* **32,** 969–978 (2011).
54. Haiss, W., Thanh, N. T. K., Aveyard, J. & Fernig, D. G. Determination of Size and Concentration of Gold Nanoparticles from UV − Vis Spectra Determination of Size and Concentration of Gold Nanoparticles from UV - Vis Spectra. **79,** 4215–4221 (2015).
55. Smith, P. K. *et al.* Measurement of protein using bicinchoninic acid. *Anal. Biochem.* **150,** 76–85 (1985).
56. Altschul, S. F., Gish, W., Miller, W., Myers, E. W. & Lipman, D. J. Basic local alignment search tool. *J. Mol. Biol.* **215,** 403–10 (1990).
57. Henikoff, S. & Henikoff, J. G. Amino acid substitution matrices from protein blocks. *Proc. Natl. Acad. Sci. U. S. A.* **89,** 10915–10919 (1992).
58. Marchler-Bauer, A. *et al.* CDD: NCBI's conserved domain database. *Nucleic Acids Res.* **43,** D222–D226 (2015).
59. Petersen, B., Petersen, T., Andersen, P., Nielsen, M. & Lundegaard, C. A generic method for assignment of reliability scores applied to solvent accessibility predictions. *BMC Struct. Biol.* **9,** 51 (2009).
60. Pedretti, A., Villa, L. & Vistoli, G. Atom-type description language: A universal language to recognize atom types implemented in the VEGA program. *Theor. Chem. Acc.* **109,** 229–232 (2003).
61. Pedretti, A. and Vistoli, G. ProBuilder On-Line. (2016). Available at: http://www.vegazz.net/.
62. Goodsell, D. S. & Olson, a J. Automated docking of substrates to proteins by simulated annealing. *Proteins* **8,** 195–202 (1990).
63. Trott, O. & Olson, A. J. AutoDock Vina. *J. Comput. Chem.* **31,** 445–461 (2010).
64. Pettersen, E. F. *et al.* UCSF Chimera - A visualization system for exploratory research and analysis. *J. Comput. Chem.* **25,** 1605–1612 (2004).
65. Liang, J. & Dill, K. A. Are proteins well-packed? *Biophys. J.* **81,** 751–66 (2001).
66. Proteolytic Enzymes in Blood . (1950).
67. Lemey, P., Salemi, M. & Vamdamme, A. *The phylogenetic handbook*. *Book* (2009). doi:10.1017/CBO9780511819049

Blank page

I. Supplementary data

Table I.1. Monitoring steps of synthesis and functionalizations of AuNP by UV-Vis absorbance bands intensity.

Sample	SPR (nm)	Abs (SPR)	Abs (450 nm)	diameter (nm)	ε_{450nm} ($M^{-1}cm^{-1}$)	concentration (nM)
AuNP	523.0	0.418	0.227	28	1.58E+09	0.86
AuNP	523.1	0.401	0.235	18	3.87E+08	3.64
AuNP-CALNN	525.0	0.414	0.236	21	6.31E+08	2.25
AuNP	521.1	0.511	0.264	37	3.84E+09	0.41
AuNP-CALNN	521.1	0.511	0.281	26	1.24E+09	1.36
AuNP	521.1	0.533	0.289	28	1.58E+09	1.10
AuNP-CALNN	520.0	0.650	0.343	32	2.41E+09	0.85
AuNP	521.1	0.604	0.332	26	1.24E+09	1.61
AuNP-CALNN	522.0	0.566	0.300	31	2.18E+09	0.83
AuNP	520.0	0.507	0.277	27	1.40E+09	1.19
AuNP	523.0	0.591	0.347	18	3.87E+08	5.37
AuNP-CALNN	523.9	0.571	0.330	20	5.41E+08	3.66
AuNP	521.0	0.550	0.316	20	5.41E+08	3.51
AuNP-CALNN	524.0	0.620	0.360	19	4.60E+08	4.70
AuNP	523.0	0.553	0.317	21	6.31E+08	3.01
AuNP-CALNN	524.9	0.593	0.351	18	3.87E+08	5.43
AuNP	520.1	0.525	0.275	33	2.66E+09	0.62
AuNP	520.1	0.593	0.326	26	1.24E+09	1.58
AuNP	519.9	0.598	0.323	28	1.58E+09	1.23
AuNP-CALNN	520.1	0.513	0.271	32	2.41E+09	0.67
AuNP	524.1	0.609	0.354	19	4.60E+08	4.62
AuNP-CALNN	523.0	0.540	0.304	23	8.42E+08	2.17
AuNP-CALNN	524.1	0.305	0.178	19	4.60E+08	2.33

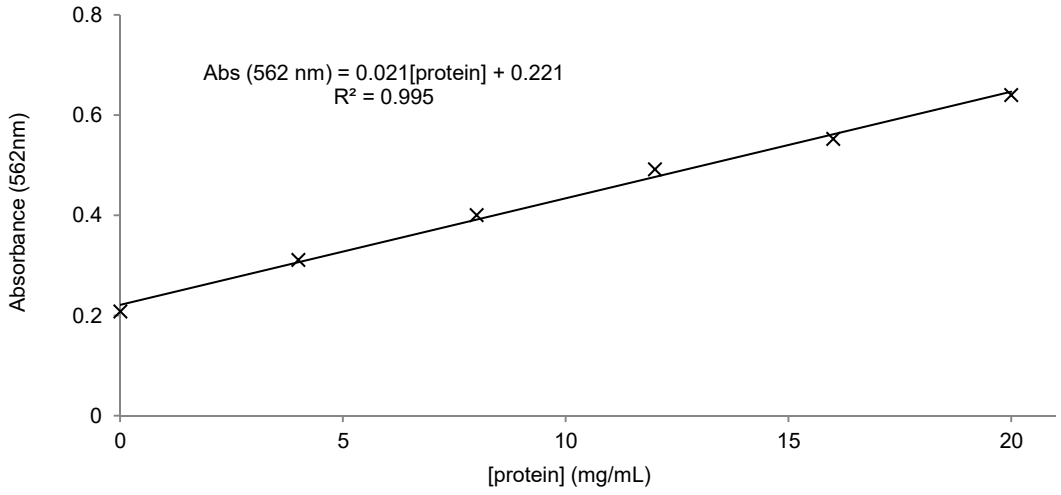

Figure I.1. Calibration curve for BCA method using 1 mg/mL of bovine serum albumin as standard.

Table I.2. Molar extinction coefficient (ε) at λ = 450 nm for gold nano particles in water with diameter *d* ranging from 2 to 100 nm [54]).

d/ nm	ε_{450} / $M^{-1}cm^{-1}$	*d*/ nm	ε_{450} / $M^{-1}cm^{-1}$	*d*/ nm	ε_{450} / $M^{-1}cm^{-1}$
2	4.25E+05	35	3.21E+09	68	2.50E+10
3	1.49E+06	36	3.52E+09	69	2.61E+10
4	3.62E+06	37	3.84E+09	70	2.71E+10
5	7.20E+06	38	4.18E+09	71	2.82E+10
6	1.26E+07	39	4.54E+09	72	2.93E+10
7	2.03E+07	40	4.92E+09	73	3.05E+10
8	3.07E+07	41	5.32E+09	74	3.16E+10
9	4.43E+07	42	5.74E+09	75	3.28E+10
10	6.15E+07	43	6.18E+09	76	3.40E+10
11	8.27E+07	44	6.65E+09	77	3.52E+10
12	1.09E+08	45	7.13E+09	78	3.64E+10
13	1.39E+08	46	7.65E+09	79	3.77E+10
14	1.76E+08	47	8.18E+09	80	3.89E+10
15	2.18E+08	48	8.74E+09	81	4.02E+10
16	2.67E+08	49	9.32E+09	82	4.14E+10
17	3.24E+08	50	9.92E+09	83	4.27E+10
18	3.87E+08	51	1.06E+10	84	4.40E+10
19	4.60E+08	52	1.12E+10	85	4.53E+10
20	5.41E+08	53	1.19E+10	86	4.65E+10
21	6.31E+08	54	1.26E+10	87	4.78E+10
22	7.31E+08	55	1.33E+10	88	4.91E+10
23	8.42E+08	56	1.41E+10	89	5.04E+10
24	9.64E+08	57	1.48E+10	90	5.17E+10
25	1.10E+09	58	1.57E+10	91	5.30E+10
26	1.24E+09	59	1.65E+10	92	5.43E+10
27	1.40E+09	60	1.73E+10	93	5.56E+10
28	1.58E+09	61	1.82E+10	94	5.69E+10
29	1.76E+09	62	1.91E+10	95	5.82E+10
30	1.96E+09	63	2.00E+10	96	5.94E+10
31	2.18E+09	64	2.10E+10	97	6.07E+10
32	2.41E+09	65	2.19E+10	98	6.19E+10
33	2.66E+09	66	2.29E+10	99	6.31E+10
34	2.93E+09	67	2.40E+10	100	6.44E+10

Table I.3. Average absorbance values, and total protein concentration of human plasma samples MG and IMM.

sample	Abs (562 nm)	[protein] (mg/mL)
MG	0.2789	7.7
	0.2878	7.9
	0.3025	8.3
	0.3725	10.2
	0.3896	10.7
	0.4291	11.8

sample	Abs (562 nm)	[protein] (mg/mL)
IMM	0.2458	13.6
	0.3001	16.6
	0.3592	19.8
	0.4389	24.2
	0.5667	31.2
	0.6670	36.6

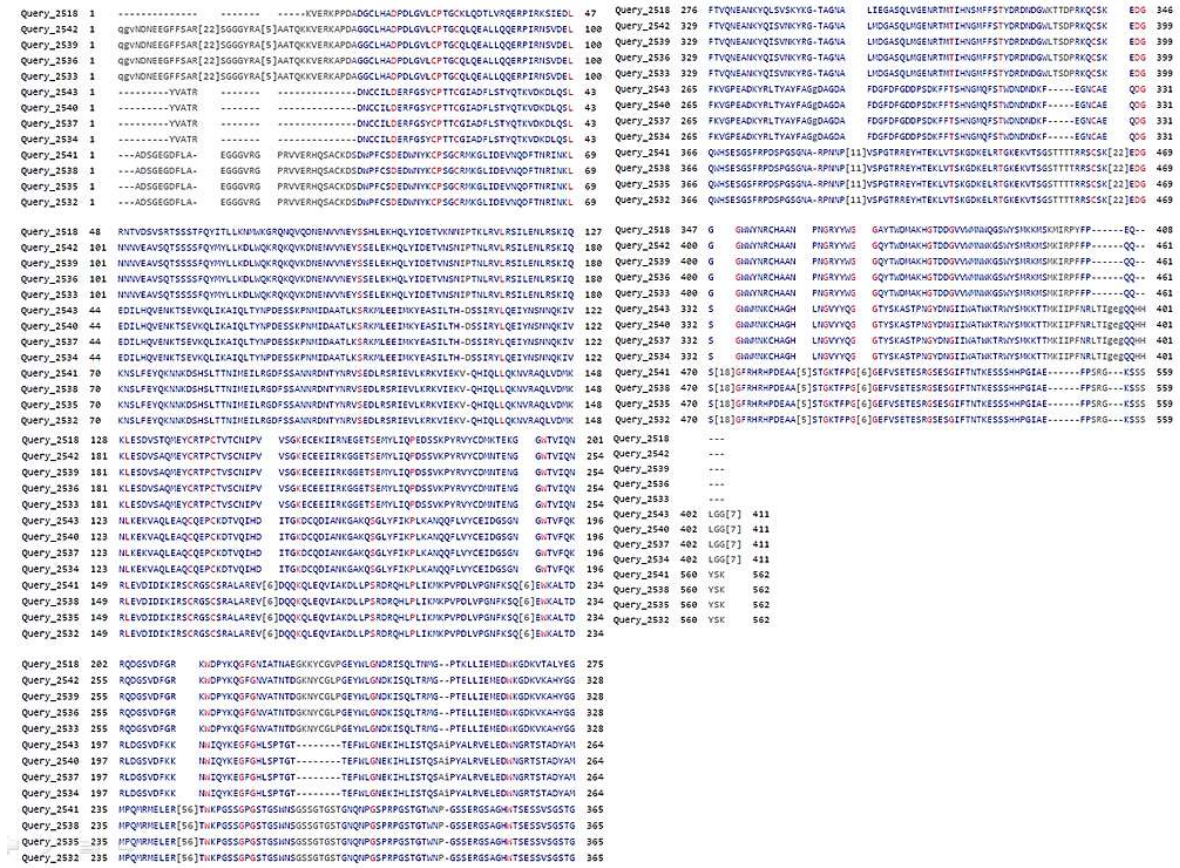

Figure I.2. Sequence alignment for human (PDB 3GHG) and bovine (PDB 1DEQ) fibrinogen.

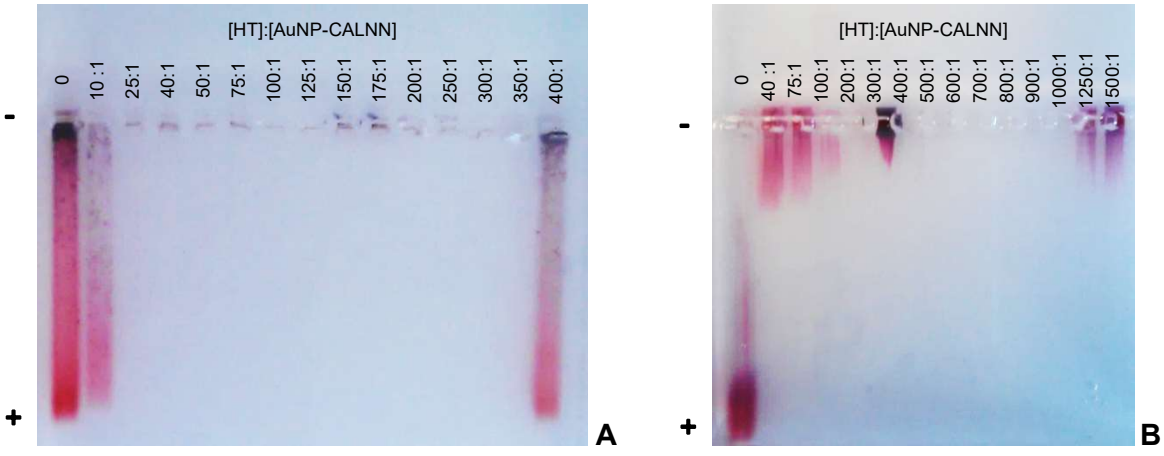

Figure I.3. Electrophoretic mobility assays for HT:AuNP-CALNN bionanoconjugates with increasing transferrin to nanoparticle ratios.

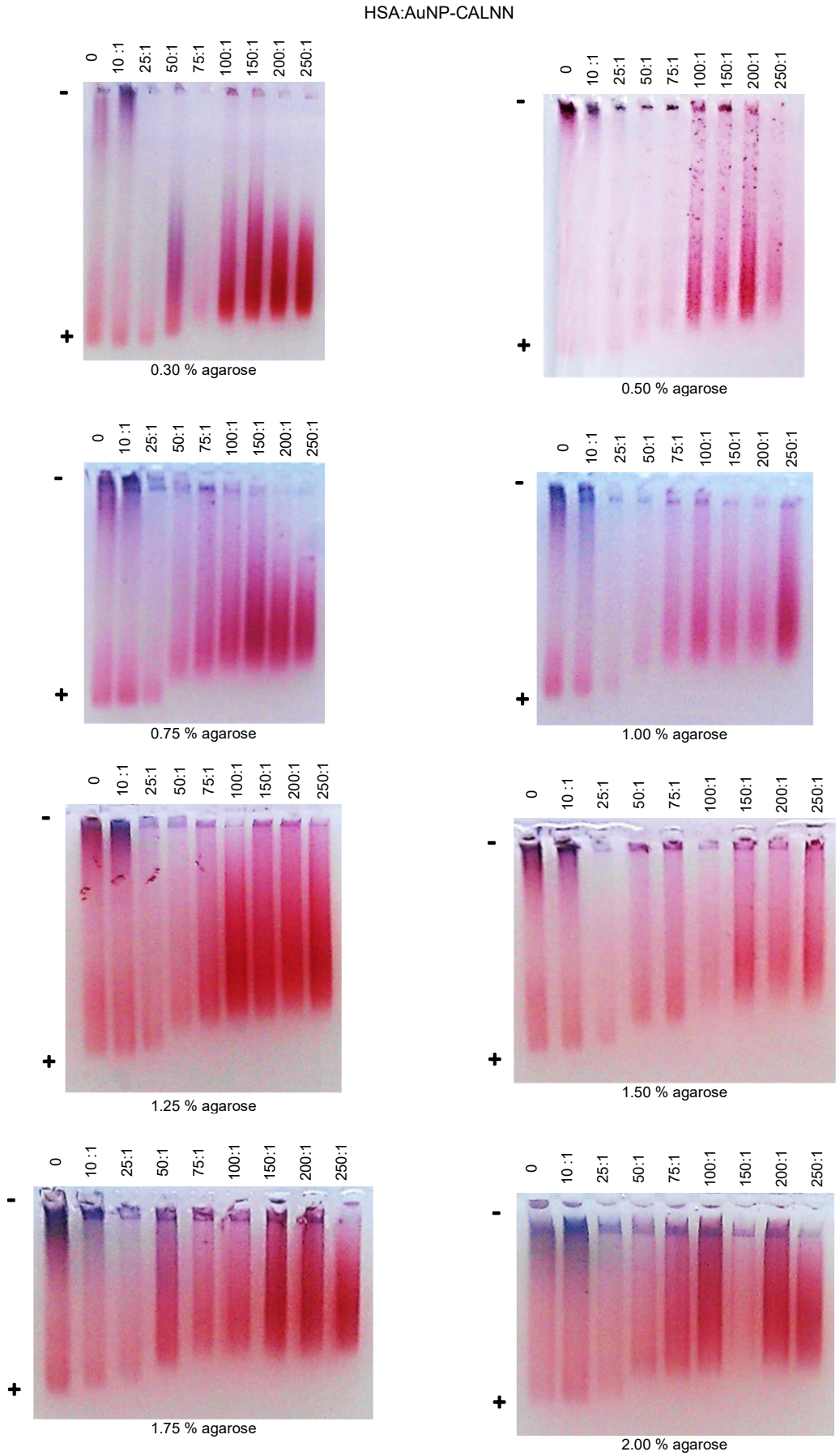

Figure I.4. Electrophoretic mobility assays of HSA:AuNP-CALNN bionanoconjugates with increasing concentration ratios, run in agarose gels with increasing agarose percentage.

Table I.4. Docking results for binding modes of CALNN ligand with the biological unit of transferrin (PDB 3V83), affinity energies and rmsd deviation values.

Mode	Affinity (kcal/mol)	Distance from best mode	
		rmsd l.b.	rmsd u.b.
1	-5.3	0.000	0.000
2	-5.1	3.286	4.717
3	-4.7	52.441	55.494
4	-4.5	4.560	8.024
5	-4.5	40.463	42.773
6	-4.4	3.724	6.400
7	-4.4	3.712	6.234
8	-4.4	37.006	40.116
9	-4.3	21.987	26.080

Table I.5. Docking results for binding modes of NNN ligand with the biological unit of transferrin (PDB 3V83), their affinity energies and rmsd deviation values.

Mode	Affinity (kcal/mol)	Distance from best mode	
		rmsd l.b.	rmsd u.b.
1	-3.9	0.000	0.000
2	-3.9	34.638	37.119
3	-3.7	38.561	39.800
4	-3.6	2.073	2.636
5	-3.6	37.305	39.091
6	-3.4	28.592	29.799
7	-3.4	14.634	15.329
8	-3.2	38.214	39.269
9	-3.1	59.847	61.725

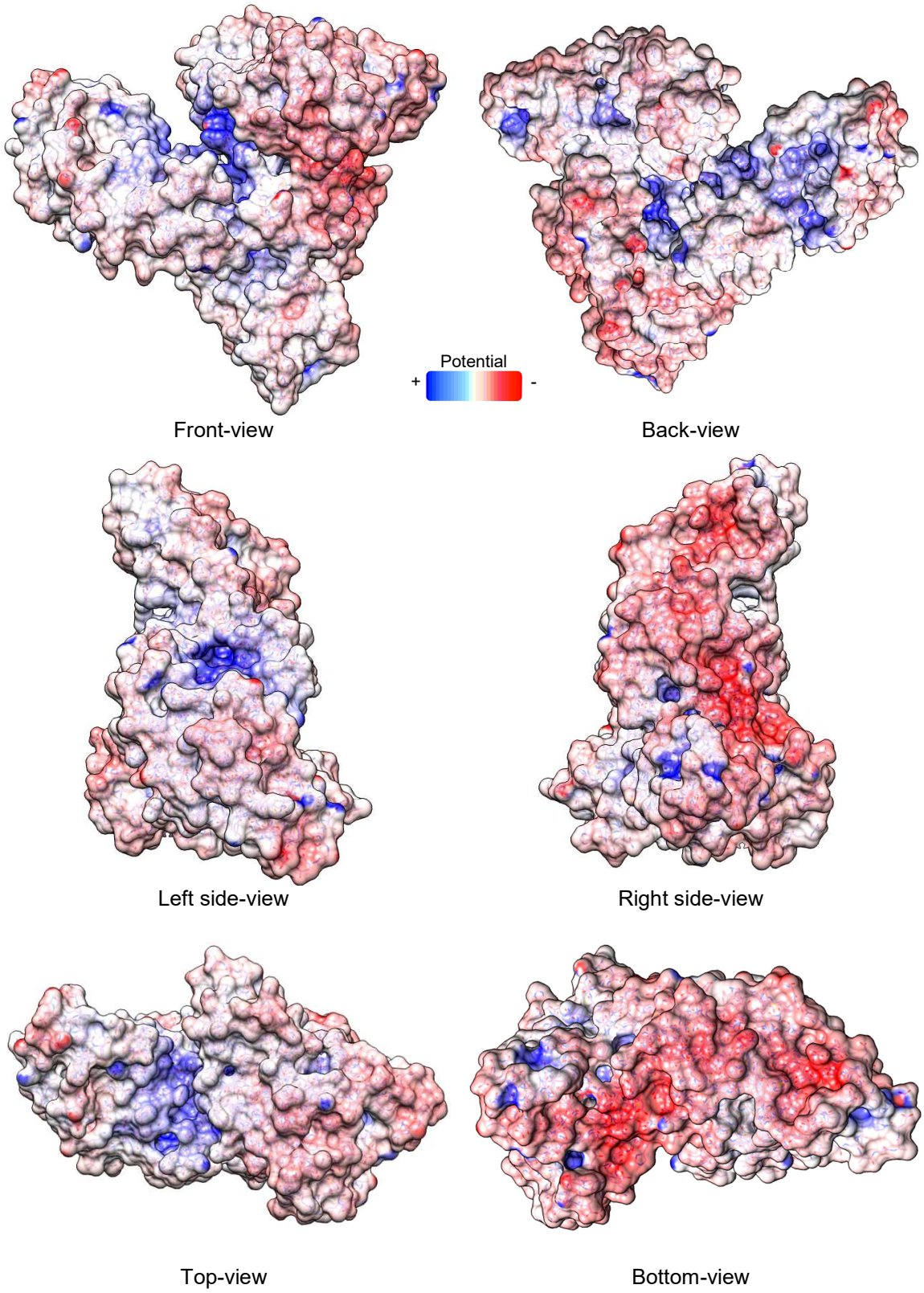

Figure I.5. Molecular visualizations of the electrostatic potential surface (EPS) of human serum albumin (PDB 1E7I) at pH 7.4.

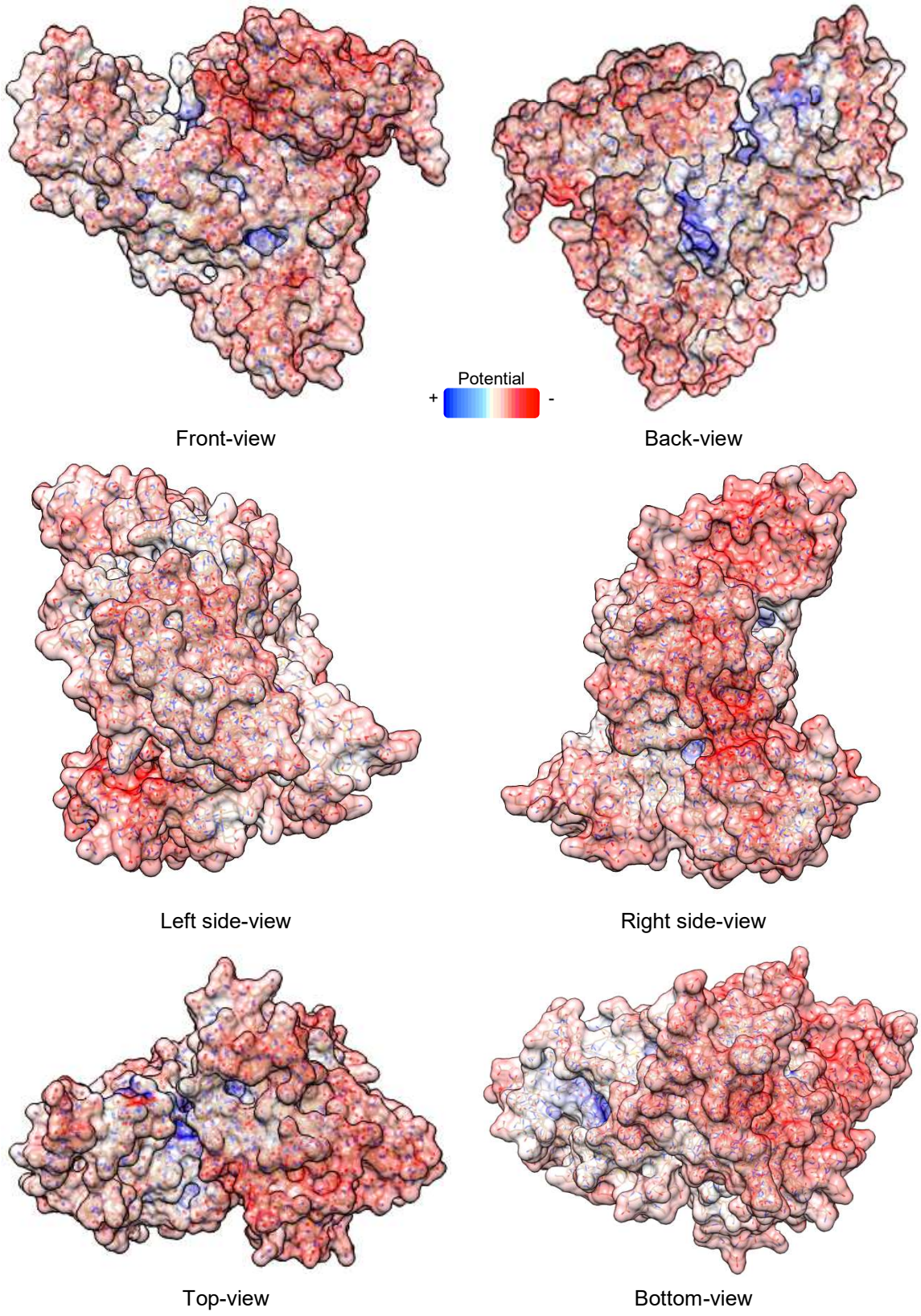

Figure I.6. Molecular visualizations of the electrostatic potential surface (EPS) of bovine serum albumin (PDB 4F5S) at pH 7.4.

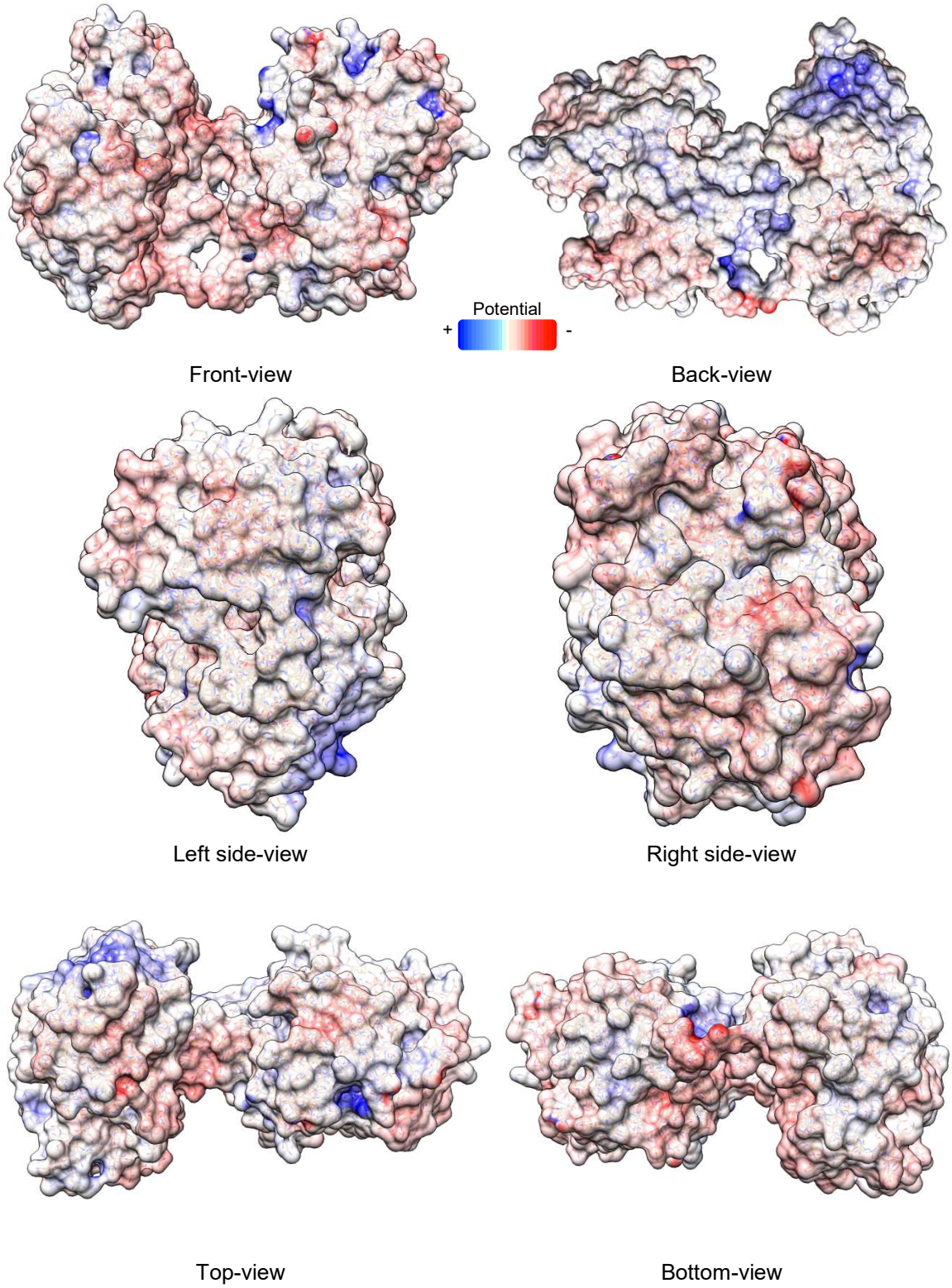

Figure I.7. Molecular visualizations of the electrostatic potential surface (EPS) of human transferrin (PDB 3V83) at pH 7.4.

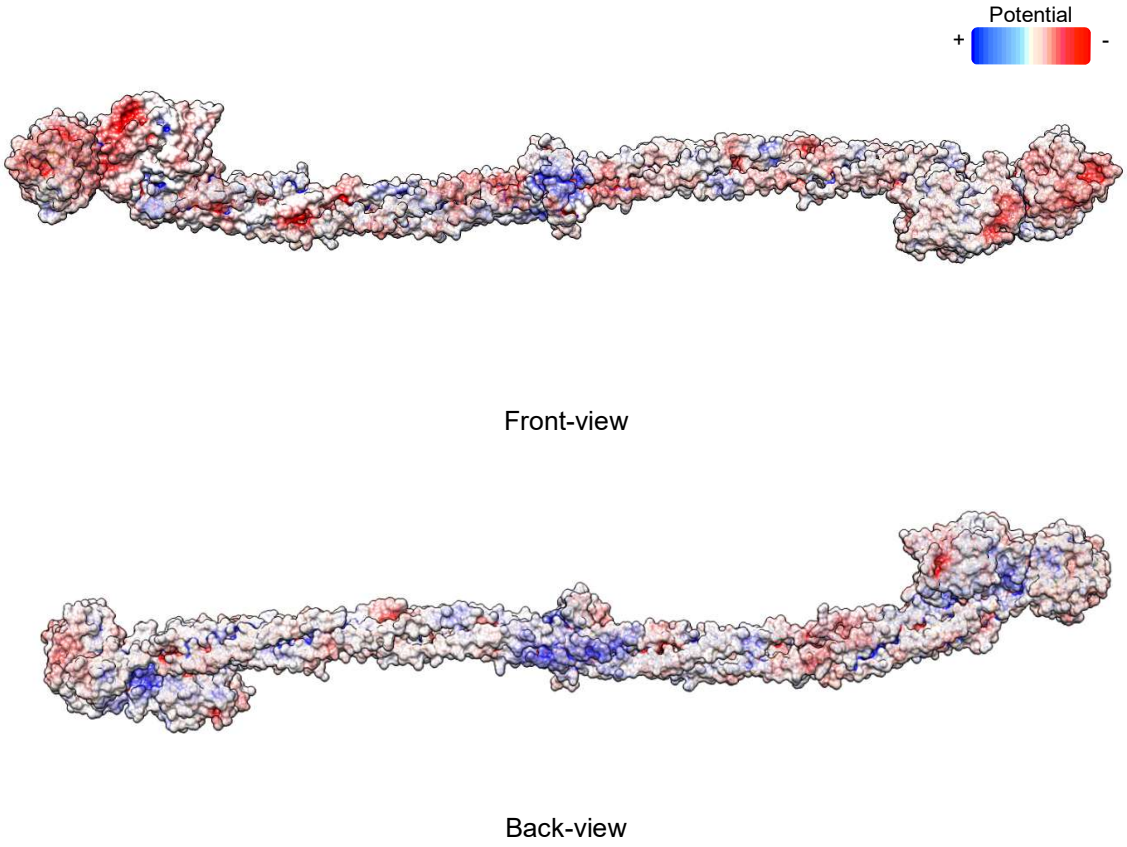

Figure I.8. Molecular visualizations of the electrostatic potential surface (EPS) of human fibrinogen (PDB 3GHG) at pH 7.4.